1-10-2024

DEVELOPMENT OF A XENOGRAFT FOR ANNULAR REPAIR USING PULSED ELECTRIC FIELD EXPOSURES FOR ENHANCED DECELLULARIZATION

Prince Mensah Kwaku Atsu
Rowan University

Recommended Citation

Atsu, Prince Mensah Kwaku, "DEVELOPMENT OF A XENOGRAFT FOR ANNULAR REPAIR USING PULSED ELECTRIC FIELD EXPOSURES FOR ENHANCED DECELLULARIZATION" (2024). *Theses and Dissertations*. 3179.
https://rdw.rowan.edu/etd/3179

1-10-2024

DEVELOPMENT OF A XENOGRAFT FOR ANNULAR REPAIR USING PULSED ELECTRIC FIELD EXPOSURES FOR ENHANCED DECELLULARIZATION

Prince Mensah Kwaku Atsu

ENHANCED DECELLULARIZATION OF FIBROCARTILAGE TISSUE USING PULSED ELECTRIC FIELD EXPOSURES

by

Prince Mensah Kwaku Atsu

A Dissertation

Submitted to the
The Department of Chemical Engineering
College of Engineering
In partial fulfillment of the requirement
For the degree of
Doctor of Philosophy
at
Rowan University
June 16, 2023

Dissertation Chair: Kirti Yenkie, PhD., Professor, Department of Chemical Engineering

Committee Members:
Gary Thompson, PhD., Senior Research Scientist, WuXi AppTec
Erik Brewer, PhD., Professor, Department of Biomedical Engineering
Thomas Chistiani, PhD., Senior Scientist, In Vitro Diagnostics Solutions
Caleb Roth, PhD., Research Scientist, Air Force Research Laboratory

Dedication

To the loving memory of my late brother: Courage Enam Atsu

Acknowledgments

I would like to first and foremost thank my supervisor, Dr. Gary Thompson, who has supported me though my years in Rowan University. He has provided me with countless opportunities and has helped prepare me for my future career.

I would like to thank Dr. Tom Chistiani, a committee member, for sharing his depth of knowledge in bovine tissue dissection and to Dr Erik Brewer, another committee member, for the many great conversation we have had about the clinical implications of our work. Special thanks to the rest of my committee members, Dr. Kirti Yenkie and Dr. Caleb Roth for your time and thoughtful guidance.

I would like to thank my colleague and lab member, Zaha Safaei for always smiling during our countless experiment hours, even when breaking equipment. To all the friends I have made at Rowan, in particular, Emmanuel Aboagye who encouraged me, listened to me complain, ate countless lunches with and continue to share their friendship.

I especially need to acknowledge my family. To my uncle, Dr. Daniel Atsu, my dad, Alex Atsu and my mom Rejoice Wemega, I say thank you. You have been with me from the beginning, and you believed in this journey more than I could imagine. To my wife, Paulina Ewusi-Ansah, thank you for knowing when all I need is a good restaurant and a few movies to get my mind off work. Words can never express how important you have been in making this work come to fruition. You kept me sane during the hectic schedules, kept me fed when I would work late, and brought me back to reality when I couldn’t see the finish line; your unconditional love and support are the reason that I was successful in graduate school.

Abstract

Prince Mensah Kwaku Atsu
DEVELOPMENT OF A XENOGRAFT FOR ANNULAR REPAIR USING PULSED ELECTRIC FIELD EXPOSURES FOR ENHANCED DECELLULARIZATION
2022-2023
Kirti Yenkie, PhD.
Doctor of Philosophy in Chemical Engineering

Severe back injuries and chronic pain necessitate surgical replacement of damaged intervertebral disc (IVD) cartilage in advanced disease stages. Bovine IVD tissue has been exposed to an upper threshold pulsed electric field (PEF) dose, causing cell death without thermal damage to the tissue. Subsequent PEF exposures at lower magnitudes have accelerated the removal of immunogenic biomolecules though electrokinetic extraction using optimized aqueous solutions. This approach yields a natural scaffold, ready for biocompatibility and mechanical strength assessment. The effects of microsecond pulsed electric fields (µsPEF) on primary bovine AF fibroblast-like cells have been characterized in vitro. PEFs of 10 and 100 µs durations, with varying numbers of pulses and electric field strengths, were applied to the cells. Furthermore, a low-intensity and minimally heating PEF-induced electrokinetic flow for molecular extraction has been established, involving the determination of the electrophoretic mobility of charged molecules within the AF cartilage tissue. Ultimately, a biocompatible AF scaffold has been generated using PEF and electrolyte solutions in a custom-designed bioreactor. Compared to chemical methods that take days, PEF application achieves decellularization of cartilage tissue within three hours, while preserving the desired biomolecules and ultrastructure of the tissue matrix.

Table of Contents

Table of Contents (Continued)

Table of Contents (Continued)

Table of Contents (Continued)

Table of Contents (Continued)

Table of Contents (Continued)

List of Figures

Figure Page

List of Figures (Continued)

List of Figures (Continued)

List of Figures (Continued)

Figure Page

List of Figures (Continued)

List of Figures (Continued)

List of Tables

Chapter 1

Introduction

About 31 million Americans suffer lower back pain (LBP) at any given time, and LBP has a global lifetime prevalence of 80 % [1–3]. Back and spine pathologies are the common source of pain and disability and contribute significantly to job-related absenteeism. The rate of clinically significant incidents is at 1.39 per 1000 person years [4]. This disability causes a huge public health burden with an estimate of $100 - $200 billion spent annually, a third being the result of lost wages and reduced productivity [4]. The etiology of LBP is diverse and hard to pinpoint. It has been demonstrated that the pain can originate from the intervertebral disc (IVD), vertebrae, facet joints, neural elements and the surrounding musculature or fascia, or a combination of these structures [4,5]. The IVD has been extensively studied and is the most identifiable source of LBP.

IVD damage often causes severe pain and significant decrease in quality of life. IVD disease commonly referred to as degenerative disc disease (DDD) correlates with increasing age and burdens the global healthcare system. Traditionally, early stages DDD are treated conservatively with rest, medications and physical therapy, but progression to later stages is very likely [6]. Later stages require surgical intervention using prosthetic disc replacement or complete removal of the IVD. Total disc replacement and fusion cages provide relief from the pain; however, they reduce the range of motion. Not only do fusion and prosthetics limit range of motion – they accelerate degeneration of adjacent IVDs [7]. Therefore, therapeutic methods are needed to prevent progression and provide long-term stability of the spine.

Over the past decade, investigators have sought to use allograft and xenograft IVD components for tissue scaffolds [3,5]. Existing chemical methods of removing immunogenic components from IVDs take days to weeks, and result in decreased hydrating proteoglycan (PG) content and compromised mechanical properties [5,8]. Furthermore, there is a lack of research on decellularizing the highly structured, outer AF region of IVDs. Although the method of using PEF exposure(s) for creating tissue scaffolds has been patented recently [9], PEF of avascular tissue such as IVDs is not well-studied, and the patent mentions chemical detergents for removal of biomolecules. We propose a systematic study of a novel method of decellularization of bovine annular fibrosus (AF) tissue and removal of immunogenic components by combining electroporation, fluid perfusion, and electrophoresis – enhancing the extent and efficiency of fibrocartilage xenograft preparation.

1.1 Motivation

The motivation for this dissertation arises from the pressing need to address severe back injuries and chronic pain, which significantly impair the quality of life for millions of individuals worldwide. The current surgical interventions for advanced stages of intervertebral disc (IVD) degeneration, which often involve the replacement of damaged IVD cartilage, are invasive and carry risks associated with implant rejection and limited long-term efficacy.

The innovative approach of using pulsed electric fields (PEF) to induce cell death without thermal damage presents a promising alternative to traditional methods. It offers a way to create a natural scaffold from bovine IVD tissue that potentially circumvents the complications associated with synthetic implants. The ability to accelerate the removal of immunogenic biomolecules through electrokinetic extraction further enhances the suitability of the resulting scaffold for clinical applications, ensuring that the natural architecture of the tissue is preserved while eliminating elements that could provoke an immune response.

Moreover, the in vitro characterization of the effects of microsecond pulsed electric fields (µsPEF) on primary bovine annulus fibrosus (AF) fibroblast-like cells provides critical insights into optimizing the parameters for scaffold preparation. This research could lead to a standardized protocol that ensures the consistency and safety of the scaffolds produced for therapeutic use.

The development of a low-intensity, minimally heating PEF-induced electrokinetic flow for molecular extraction represents a significant advancement in tissue engineering. It allows for the precise manipulation of the tissue's biochemical composition, which is crucial for the maintenance of biocompatibility and mechanical integrity.

The culmination of this work in the generation of a biocompatible AF scaffold using PEF and electrolyte solutions in a custom-designed bioreactor demonstrates a significant reduction in the time required for decellularization. This efficiency, coupled with the preservation of essential biomolecules and ultrastructure, positions this method as a superior alternative to chemical decellularization processes.

In essence, the motivation behind this dissertation is to contribute to the field of regenerative medicine by providing a novel, efficient, and potentially more effective method for preparing IVD scaffolds. This work aims to pave the way for new treatments that can alleviate suffering, reduce the burden on healthcare systems, and ultimately improve patient outcomes in the treatment of back injuries and chronic pain.

1.2 LBP Threshold – Pain Management vs. Tissue Replacement

The pain threshold for lower back pain (LBP) is a subjective measure and varies widely among individuals. It is typically assessed using patient-reported scales such as the Visual Analogue Scale (VAS) or the Numeric Rating Scale (NRS), which help clinicians gauge the severity of pain and its impact on a patient's daily activities.

When comparing pain management to tissue replacement for LBP, each approach has its considerations. Pain management strategies aim to alleviate discomfort and improve function without surgery. These methods include medications, physical therapy, lifestyle changes, and sometimes interventional procedures like steroid injections. The effectiveness of pain management is variable; while some patients may find significant relief, others may continue to experience persistent pain. The risks and side effects associated with pain management are generally related to the specific treatments used, and the costs can accumulate over time due to the ongoing nature of these therapies.

On the other hand, tissue replacement, such as intervertebral disc (IVD) replacement, is a more invasive option that involves surgical intervention to replace damaged tissue with a biological scaffold or artificial substitute. This approach is typically reserved for cases where conservative treatments have failed, and the LBP is debilitating. Tissue replacement aims to provide a long-term solution by addressing the root cause of pain. However, it comes with its own set of risks, including surgical complications and the potential for implant rejection. The recovery period post-surgery is significant, requiring rehabilitation to regain full function. While the upfront costs of tissue replacement are high due to the surgery, successful outcomes may reduce the long-term financial burden of managing chronic LBP.

In essence, the choice between pain management and tissue replacement is complex and must be tailored to the individual patient's condition, weighing the potential benefits against the risks and long-term implications of each treatment option.

1.3 Key Questions Addressed in this Work

The dissertation addresses several key questions that are critical to advancing the field of tissue engineering and regenerative medicine, particularly in the context of treating severe back injuries and chronic pain through intervertebral disc (IVD) repair:

1. **Can pulsed electric fields (PEF) be used to induce cell death in bovine IVD tissue without causing thermal damage?**
    - This question explores the viability of PEF as a non-thermal method to selectively ablate cells within the tissue, which is crucial for preserving the extracellular matrix.
2. **What are the optimal PEF parameters to remove immunogenic biomolecules from IVD tissue while maintaining its structural integrity?**
    - Determining the appropriate duration, intensity, and number of pulses necessary to achieve effective decellularization without compromising the tissue's mechanical properties is essential for scaffold preparation.

3. **How does the application of microsecond pulsed electric fields (µsPEF) affect primary bovine AF fibroblast-like cells in vitro?**
    - Understanding the cellular response to µsPEF treatments helps in tailoring the electric field parameters to either promote cell viability or induce apoptosis, depending on the desired outcome.
4. **Can PEF-induced electrokinetic flow be controlled to extract specific molecules from AF cartilage tissue?**
    - This question addresses the ability to manipulate the tissue's biochemical environment, which is vital for ensuring that the scaffold is free of substances that could elicit an immune response.
5. **What is the electrophoretic mobility of charged molecules within the AF cartilage tissue, and how can it be utilized for tissue engineering?**
    - By understanding how charged molecules move within the tissue under an electric field, researchers can optimize conditions for molecular extraction and scaffold preparation.
6. **Is it possible to create a biocompatible AF scaffold using PEF and electrolyte solutions in a custom-designed bioreactor?**
    - This question investigates the feasibility of a novel bioreactor system to produce scaffolds that are compatible with human biology and suitable for implantation.

7. **How does the PEF-based decellularization process compare to traditional chemical methods in terms of efficiency, preservation of biomolecules, and maintenance of tissue ultrastructure?**
    - Evaluating the effectiveness of the PEF approach against conventional methods is crucial for establishing its potential as a superior alternative for scaffold production.

By answering these questions, the dissertation contributes valuable knowledge to the field, potentially leading to the development of new, less invasive treatments for back injuries and chronic pain, and opening the door to further research and clinical applications.

1.4 Overview of Pulsed Electric Field Applications

Pulsed electric fields (PEF) technology is a versatile tool that has been harnessed in various fields, ranging from food science to cancer treatment, due to its ability to permeabilize cell membranes without significant thermal damage. In the food industry, PEF has emerged as a revolutionary non-thermal pasteurization method. It has been shown to effectively inactivate pathogenic microorganisms in liquid foods while preserving flavor, color, and nutritional value, which is a significant advantage over traditional heat pasteurization [10–16]. This application not only extends the shelf life of products like juices and milk but also maintains their quality, which is highly valued by consumers seeking minimally processed foods.

In medical research, PEF has been investigated for its potential in cancer treatment through a process called electrochemotherapy. By inducing temporary permeability in cell membranes, PEF enhances the uptake of chemotherapeutic drugs into cancer cells, potentially increasing the effectiveness of the treatment. Studies have demonstrated improved outcomes in various cancers, including cutaneous and subcutaneous tumors, with reduced systemic toxicity [17].

The environmental sector has also benefited from PEF technology, particularly in wastewater treatment. Research has indicated that PEF can effectively inactivate bacteria and viruses in wastewater, presenting a viable alternative to chemical disinfectants that can produce harmful by-products [18,19]. This application is particularly promising for the development of more sustainable and eco-friendly water treatment methods.

In the biofuel industry, PEF is utilized for the pretreatment of biomass, where it disrupts the cell walls of plants and microorganisms, thereby enhancing the extraction of valuable compounds and improving the efficiency of subsequent enzymatic hydrolysis, a critical step in biofuel production [20]. This method is not only more efficient but also environmentally friendly, as it reduces the need for harsh chemical treatments.

The winemaking process has also been refined through the use of PEF, which aids in the extraction of phenolic compounds from grape skins, potentially improving the quality of the wine and reducing the time required for maceration [21]. This technique allows winemakers to produce high-quality wines with enhanced flavors and aromas.

In pharmaceuticals, PEF has been explored for drug delivery, particularly in the formation of liposomes and other types of vesicles that can encapsulate therapeutic agents and deliver them to specific tissues or cells [22]. This targeted approach could lead to more effective treatments with fewer side effects.

Lastly, PEF has been applied in the extraction of bioactive compounds from plant tissues, offering an efficient and environmentally friendly alternative to traditional extraction methods. This application is particularly relevant in the production of flavors, fragrances, and pharmaceuticals, where it can lead to higher yields and purer extracts [23].

These studies collectively highlight the broad potential of PEF technology to impact various industries positively. By providing efficient, non-thermal alternatives to traditional methods, PEF technology is paving the way for more sustainable and innovative practices. In the field of tissue engineering, pulsed electric fields (PEF) have been leveraged to facilitate a range of regenerative processes. For instance, Golberg et al. (2015) demonstrated that PEF could significantly enhance skin regeneration and wound healing by promoting the release of growth factors [24]. Sundelacruz et al. (2009) revealed PEF's potential in directing stem cell differentiation, a critical aspect of developing tissue-specific cells [25,26]. In creating scaffolds for tissue reconstruction, Ma et al. (2014) explored PEF for decellularizing tissues, a process vital for preparing scaffolds for organ transplantation [27]. PEF's role in promoting angiogenesis, essential for the survival of implanted tissues, was highlighted in a study by Zhao et al. (2011), which showed improved vascularization in engineered tissues [28]. In orthopedics, Chalidis et al. (2011) found that PEF could stimulate osteoblast activity, crucial for bone healing and regeneration [29]. Additionally, Iwasa et al. (2018) investigated the use of PEF in cartilage tissue engineering, noting its ability to enhance chondrocyte proliferation and matrix synthesis, vital for repairing joint damage [30]. These studies underscore PEF's emerging role as a non-invasive modulator of cellular functions, offering promising avenues for enhancing tissue regeneration across various applications in tissue engineering.

Chapter 2

Background

2.1. Anatomy of the Spine

The human spine also known as the vertebral column consists of five main regions, namely, cervical, thoracic, lumbar, sacrum and coccyx [31–33]. The sacrum and coccyx regions form the tail bone. The cervical region refers to the neck area and is made of seven individual vertebrae (C1 – C7). The thoracic region refers to vertebrae around the chest area and consists of twelve individual vertebrae (T1 – T12). The thoracic region of the spine connects to the ribs. The lumbar region forms the lower back and is made of five vertebrae (L1 – L5). The vertebrae of the spine are similar in shape except for C1 and C2 whose shapes are adapted for articulation and support for the skull. Though similar in shape, the vertebrae vary in sizes. The shape of the vertebrae consist of the main vertebral body, pedicle, foramen, superior and inferior articular processes, transverse process, and spinous process [31] (Figure 1).

The main function of the vertebral column is to transfer loads and bending moments from the head though the trunk to the pelvis [34]. The spine allows for movement and flexibility of the body, provides structure for the body, and protects the spinal cord. Adjacent vertebrae are separated by intervertebral discs (IVDs) which are interfaced at the superior and inferior surfaces of the vertebrae by a cartilaginous plate-like structure called the endplates (Figure 1). The stability and functionality of the vertebral column depends on the structural integrity of the IVDs.

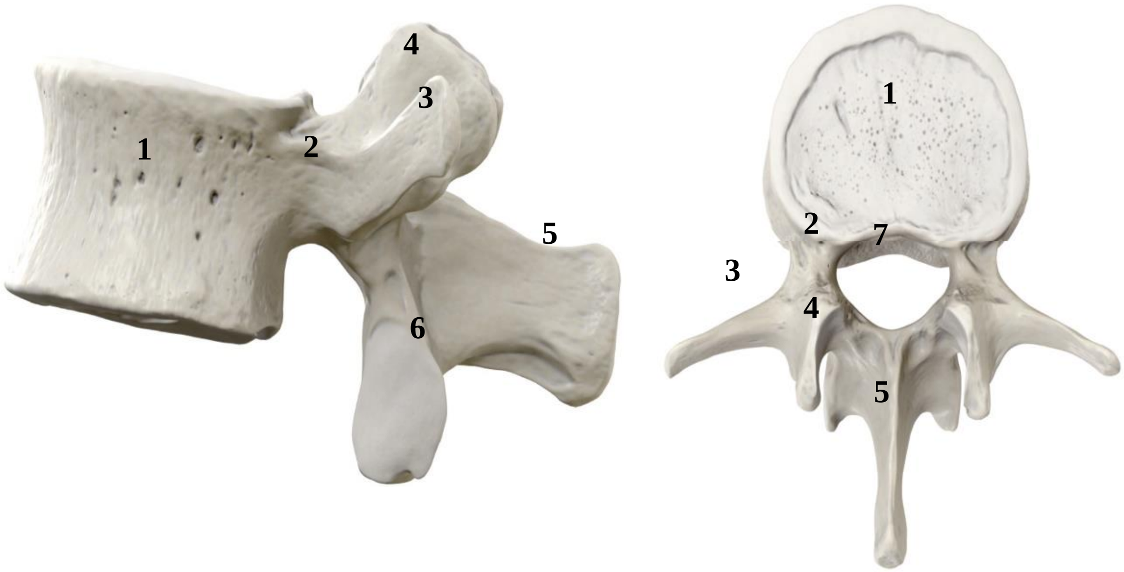

Figure 1. Representative Lumber Vertebrae [35]**.** (1) Vertebral body, (2) Pedicle, (3) Transverse process, (4) Superior articular process, (5) Spinous process, (6) Inferior articular facet, (7) Foramen

2.2. Intervertebral Disc

The IVD is the largest avascular and aneural structure in the human body [36]. The IVDs are highly hydrated fibrocartilaginous structures that separate adjacent vertebrae bodies. The IVDs act as shock absorbers, stabilizing and maintaining the alignment of the spine. The IVD gives the spine flexibility, allowing for bending and twisting and also allows for axial compression [37–41].

The structure of the IVD comprises of several interacting and interdependent tissues divided into the main components; namely: the nucleus pulposus (NP), the annulus fibrosus (AF) and the end plates (EP). The EP is a thin layer of cartilaginous plate covering the top and bottom of the IVD at the interface of the adjacent vertebrae. The AF is made of the concentric collagen sheets at outermost part of the IVD as shown in Figure 2. The AF provides structural support for the disc. It envelops the NP on the inside and attaches to adjacent vertebral bodies on the outside [42–45].

There a total of 24 movable individual vertebrae in the human spine stacked on top of each other and joined though 23 IVDs providing structure to the torso, and protection to the spinal cord and nerve roots [46–48]. Each IVD and two adjacent vertebrae provide motion with six- degrees of freedom in flexion-extension, lateral bending, and axial rotation. The structure of the IVD is such that, the confined NP generates an intervertebral disc pressure (IDP) or intradiscal pressure when the spine undergoes loading. The IDP is then distributed radially to the AF fibers generating hoop stresses within the AF, keeping the AF structure bulged out, hence contributing to the stability and function of the spine [49,50].

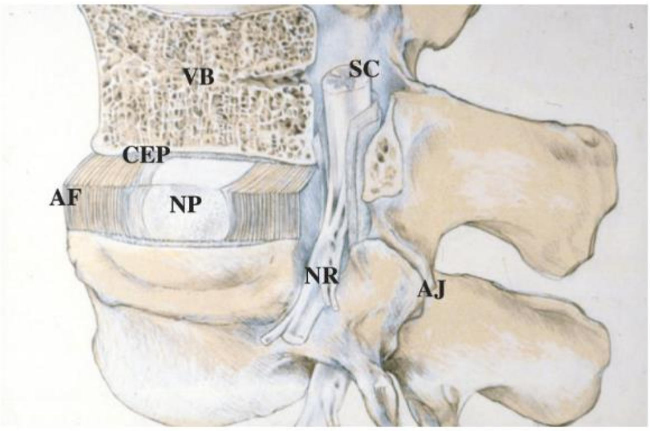

Figure 2. Structure of a Spinal Segment and the Intervertebral Disc showing the component parts. The nucleus pulposus (NP) enveloped in the annulus fibrosus (AF). The cartilaginous end plates (CEP) are shown separating the IVD and the vertebrae body (VB). The relations between the intervertebral disc and the spinal cord (SC), the nerve root (NR), and the apophyseal joints (AJ) are also shown [51]

2.2.1 Nucleus Pulposus

The nucleus pulposus (NP) is a gel-like substance that makes up the innermost part of the IVD, containing a randomly oriented network of collagen type II and elastin fibers. The NP is a highly hydrated aggrecan-containing tissue consisting mainly water (87%, wet weight) and proteoglycans, which gives it its unique properties [52–54]. The proteoglycans consist of a protein core to which about a 100 highly sulphated glycosaminoglycans (GAG) chains, mainly made of chondroitin and keratin sulphate are covalently bonded [55]. The negatively charged GAGs are balanced by smaller positively charged cations in the tissue. The presence of ions allow transport of water into the NP though osmosis. The uptake of water generates an intradiscal swelling pressure within the collagen network. The intradiscal pressure within the collagen network causes bulging of the NP, enabling it to resist compressive loading with minimal deformation [53,56]. The NP is made of chondrocyte-like cells which are responsible for the synthesis of the NP extracellular matrix (ECM). The NP cells synthesize collagen type II and type X and secretes proteases and interleukins [57].

The primary function of the NP is to absorb shock and distribute pressure evenly across the IVD, helping to protect the vertebrae and other structures in the spine. It allows for flexibility and mobility in the spine by providing cushion between the vertebrae. The NP can change shape and size in response to changes in pressure, such as during movement or weight bearing activities. It can compress and expand, which helps to maintain the overall height and shape of the IVD. However, as we age, the NP undergoes changes that make it less able to absorb shock and distribute pressure evenly. The NP can become solid and less gel-like, leading to degenerative changes and development of herniated disc

[43,56,58,59].

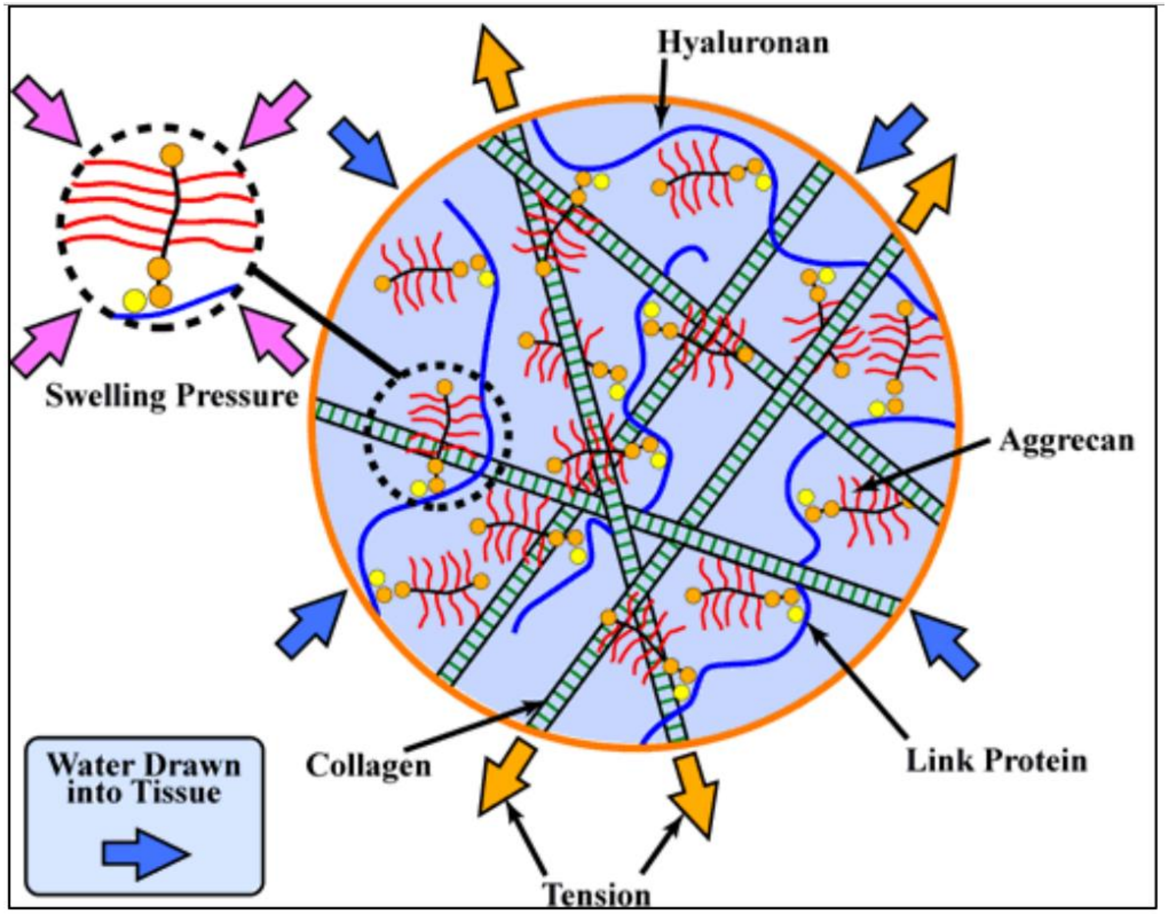

*Figure 3***.** Depiction of the function of collagen fibers and Proteoglycans in the NP [60]

2.2.2 Annulus Fibrosus

The annulus fibrosus (AF) is a specialized fibrocartilage tissue that forms the outermost layer of the IVD. The tissue is composed of concentric rings or lamellae made of collagen fiber arranged in parallel within each lamella. The fibers are oriented at 30° – 45° to the horizontal axis with alternating direction with each adjacent lamella [39,45,61,62]. The alternating lamellae form a crisscross pattern known as a ply-angle-ply architecture which is responsible for the characteristic strength and flexibility of the AF tissue. The AF is primarily composed of collagen type I and II, which account for up to 75% of the tissue dry weight. The remaining 25% is made up of proteoglycans, elastin fibers, and other proteins [44,63,64].

The collagen fibers in the AF are densely packed and arranged in an oblique orientation, creating a strong and durable structure that can withstand compressive and torsional forces. The proteoglycans within the tissue attract and hold water, contributing to the tissue's ability to resist compression and distribute pressure evenly across the disc. The elastin fibers provide the AF with its elasticity and ability to stretch and return to its original shape [48,65].

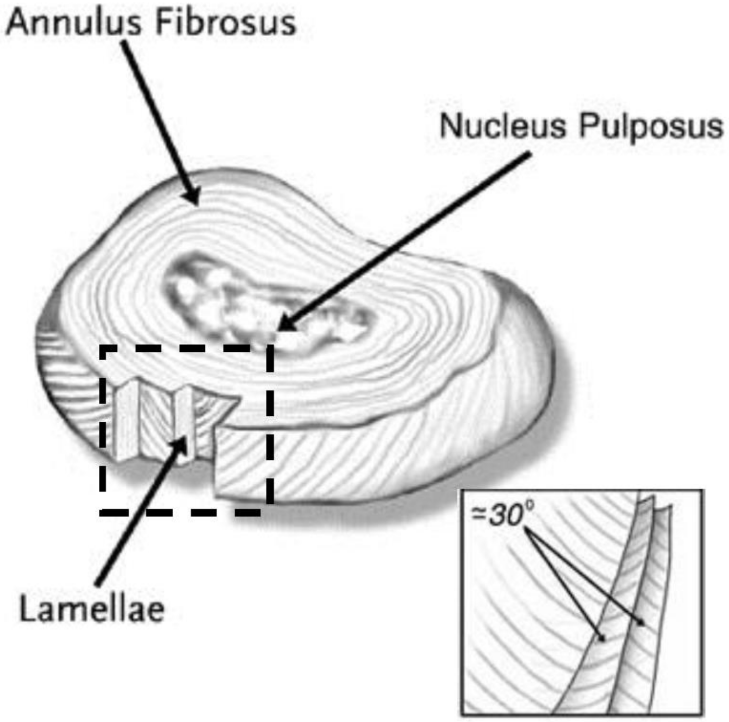

Figure 4. AF structure showing concentric sheets of fiber in the Ply-Angle-Ply architecture [60]

The structure and composition of the AF varies depending on its location within the IVD. The outermost layers of the AF are thicker and more tightly packed, providing greater strength and support, while the inner layers are thinner and more flexible, allowing for greater mobility and flexibility. The outer annulus fibrosus (OAF) is consists entirely of type I collagen fibers with a reported average thickness of 150 µm. The inner annulus fibrosus (IAF) is not as dense as the OAF and has high concentration of type II collagen fibers and proteoglycan. The IAF does not have a highly ordered lamella organization. The lamellae of the IAF have a thickness of approximately 300 µm. The OAF gradually transitions into the IAF as you move radially inwards towards the NP.

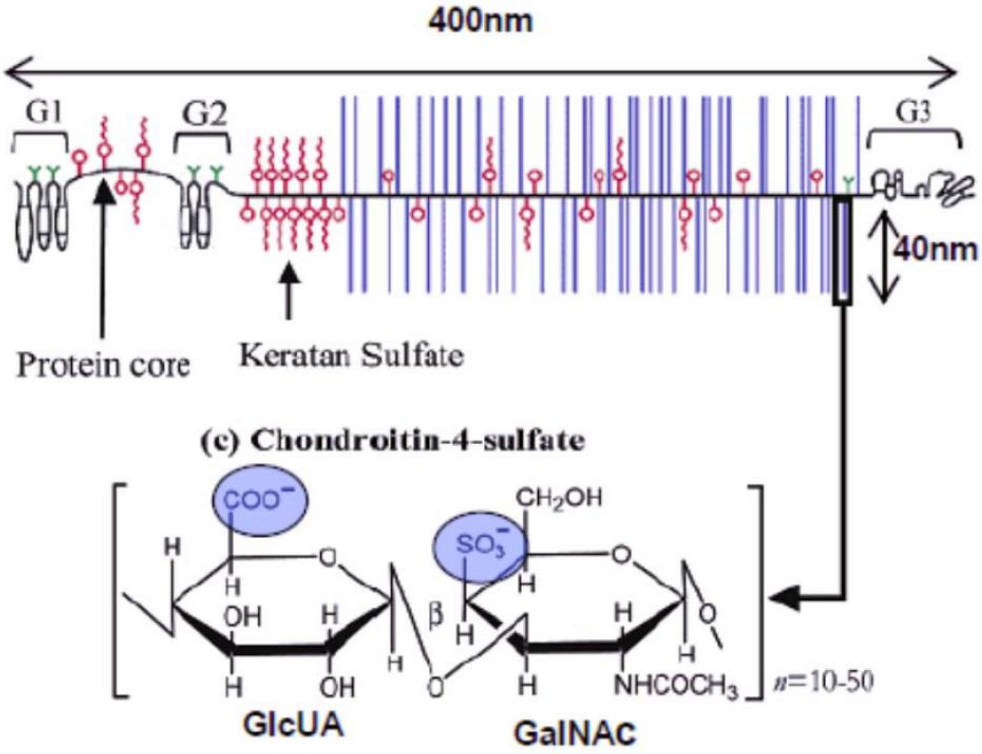

Figure 5. Chemical structure of Chondroitin Sulphate in the Aggrecan, the most abundant Proteoglycan in the IVD [66]

The number of lamellae within the annulus fibrosus is an important parameter that influences its biomechanical properties. The current understanding of the number of lamellae in the annulus fibrosus, including its variability across species, age-related changes, has potential clinical implications [67,68]. Studies have demonstrated significant interspecies variation in the number of lamellae. For example, human lumbar discs typically possess 10 to 20 lamellae, while bovine and porcine discs have been reported to have fewer lamellae [69,70]. These differences suggest that lamellar organization is influenced by anatomical and functional requirements across species. Age-related changes in the number of lamellae have been observed, with a gradual decrease reported in several studies (Table 1 and 2). These changes may result from alterations in collagen synthesis, degradation, and remodeling processes. The reduction in lamellae with age may affect disc biomechanics and contribute to age-related disc degeneration [71–74].

Table 1

Average Thickness (Mean ± Standard Deviation) of Annular Lamellae from Experimental Data of L2-L3 And L4-L5 by Marchand and Ahmed (1990)

tL (mm)6t		A	L	P-L	P	MEAN
tL (mm)6t OUT	Young	0.14 ± 0.02	0.15 ± 0.04	0.16 ± 0.06	0.11 ± 0.03	0.14 ± 0.04
	Old	0.28 ± 0.09	0.37 ± 0.11	0.40 ± 0.08	0.29 ± 0.03	0.33 ± 0.06
tL (mm)6t MID	Young	0.18 ± 0.03	0.15 ± 0.03	0.15 ± 0.05	0.18 ± 0.04	0.16 ± 0.04
	Old	0.45 ± 0.07	0.51 ± 0.09	0.50 ± 0.06	0.37 ± 0.11	0.46 ± 0.07
tL (mm)6t IN	Young	0.23 ± 0.01	0.19 ± 0.04	0.20 ± 0.05	0.2 ± 0.05	0.20 ± 0.05
	Old	0.52 ± 0.08	0.66 ± 0.14	0.49 ± 0.14	0.4 ± 0.11	0.52 ± 0.11
tL (mm)6t ALL	Young	0.18 ± 0.02	0.16 ± 0.03	0.17 ± 0.03	0.16 ± 0.03	0.17 ± 0.03
	Old	0.42 ± 0.06	0.51 ± 0.06	0.47 ± 0.07	0.35 ± 0.09	0.44 ± 0.07

Note: tL = thickness of lamellae, A = anterior, L = lateral, P-L = posterolateral, P = posterior. Young: Mean age, 23 years; range, 18 – 29 years. Old: Mean age, 63 years; range, 53 – 76 years.

The number of lamellae in the annulus fibrosus is intricately linked to its biomechanical properties. Lamellar organization influences load distribution, stress concentration, and disc deformability. Experimental studies and computational models have suggested that alterations in the number of lamellae can significantly impact the disc's mechanical behavior, potentially leading to increased vulnerability to injury or degenerative changes [75,76]. The number of lamellae in the annulus fibrosus has potential clinical implications. Variations in lamellar organization may contribute to the susceptibility of certain individuals to disc herniation, disc bulging, or other disc-related pathologies. Additionally, the number of lamellae could potentially serve as a diagnostic or prognostic marker for disc degeneration, allowing for more targeted therapeutic interventions.

Table 2

Average Number of Lamellae (Mean ± Standard Deviation) from Experimental Data by Marchand and Ahmed (1990)

DL	A	L	P-L	P	Mean
Young L2-L3	20.7 ± 3	25.5 ± 2	24.0 ± 2	20.0 ± 2	22.6 ± 3
Young L4-L5	25.5 ± 2	25.0 ± 2	23.5 ± 5	22.0 ± 2	24.0 ± 2
Old L2- L3	19.0 ± 1	20.0 ± 2	18.0 ± 1	15.0 ± 2	18.0 ± 2
Old L4- L5	19.1 ± 2	21.1 ± 2	18.0 ± 2	18.0 ± 2	19.0 ± 1
Mean	21.1 ± 3	22.9 ± 3	20.9 ± 3	18.8 ± 3	20.9 ± 3

Note. DL = Number of distinct lamellae, A = anterior, L = lateral, P-L = posterolateral, P = posterior. Young: Mean age, 23 years; range, 18 – 29 years. Old: Mean age, 63 years; range, 53 – 76 years.

The lamella work together to create a strong, durable structure that can withstand the compression and torsional forces placed on the spine during movement and activity [63,64]. They can distribute these forces evenly across the IVD, protecting the softer, more vulnerable structures within. However, if the lamellae become damaged or weakened due to injury or degeneration, they can no longer provide the necessary support to the spine leading to pain and dysfunction. The cells of the AF are a type of fibroblast-like cells that are found in the outer ring of the IVD and are essential for maintaining the structural integrity of the IVD [4].

2.2.3 Cells of the Annulus Fibrosus.

Annulus fibrosus (AF) cells are a type of fibroblast-like cells that are found in the outer ring of the intervertebral disc [77–80]. These cells are essential for maintaining the structural integrity of the disc by producing and organizing the extracellular matrix (ECM) components such as collagen and proteoglycans [4]. Several studies have demonstrated that AF cells play a crucial role in the pathogenesis of intervertebral disc degeneration (IVDD). It has been shown that AF cells undergo phenotypic changes in response to various mechanical, biochemical, and genetic factors, which can result in ECM degradation and ultimately lead to disc degeneration [81–83].

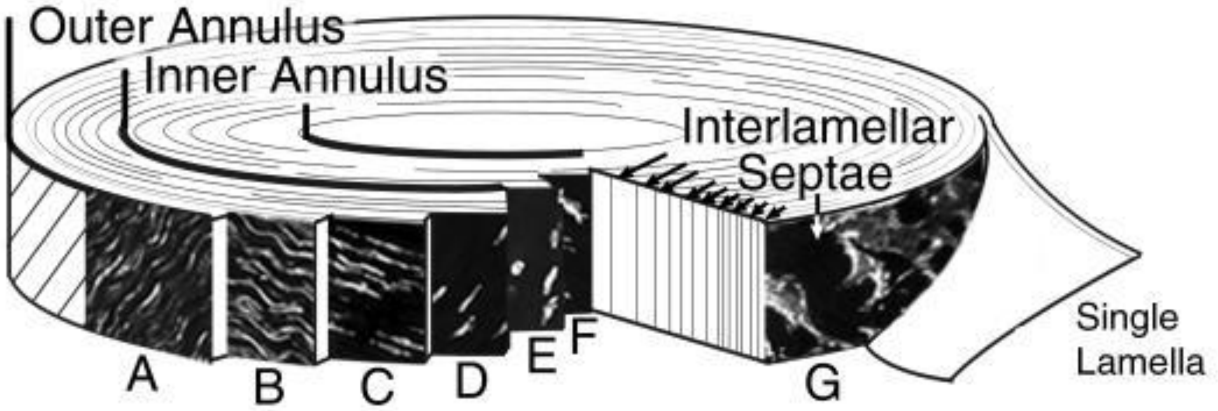

Figure 6. AF Cell Morphology as they Gradually Transition from Fusiform Cell Body to a Spherical Morphology from the Outer to the Inner Annulus [66]

2.3 Intervertebral Disc Degeneration

Intervertebral disc degeneration (IVDD) is a common condition that affects a large proportion of the population worldwide. IVDD is a common age-related condition that can lead to chonic lower back pain, sciatica, and other spinal disorders [84,85]. The condition is characterized the gradual deterioration of the matrix in the IVD and can lead to a range of symptoms, including pain, stiffness, and decreased mobility, and in severe cases can require surgical intervention [55,86–88].

The etiology of IVDD is multifactorial and includes both genetic and environmental factors [4,45,54,63]. Several studies have investigated the genetic basis of IVDD and have identified several genes that may be associated with an increased risk of the condition [89–92]. Genetic factors include mutations in genes that encode for proteins involved in the synthesis of the extracellular matrix of the IVD. Environmental factors that have been implicated in the development of IVDD includes stress, smoking, obesity, and poor posture [93–95]. A degenerated IVD is one with altered extracellular matrix which results in decreased hydration and loss of elasticity. This can lead to the formation of tears and fissures in the AF and can also cause the NP to protrude outwards [96,97].

During IVD degeneration, there is a loss of NP hydration, a reduction in proteoglycan content, and decrease in type II collagen synthesis. This results in the collapse of the disc and the formation of fissures and cleft in the AF. The decrease in proteoglycan content is due to the upregulation of matrix metalloproteinases (MMPs) and a decrease in their inhibitors, tissue inhibitors of metalloproteinases (TIMPs) [98]. MMPs are enzymes that degrade proteoglycans and type II collagen. The increase in MMPs and decrease in TIMPs result in the breakdown of the extracellular matrix in the IVD. In addition to the breakdown of the ECM, there is also an increase in pro-inflammatory cytokines such as interleukin-1β (IL-1β) and tumor necrosis factor-alpha (TNF-α) during IVD degeneration. These cytokines activate catabolic pathways and increase the expression the expression of MMPs, leading to further ECM degradation [99,100].

The decrease in water content and loss of disc height associated with IVDD leads to changes in the mechanical properties of the IVD [98,101]. These changes result in altered biomechanics, increased stress on the AF, and altered load distribution on the vertebral bodies. These increased stresses can lead to bone remodeling osteophyte formation.

2.3.1 Diagnosis and Treatment

2.3.1.1 IVDD Diagnosis. Diagnosis of IVDD uses a combination of clinical evaluation, imaging studies, and histological examination. Clinical evaluation includes a detailed medical history and physical examination. Imaging studies such as X-ray, computed tomography (CT), magnetic resonance imaging (MRI), and discography can provide information about the morphology and integrity of the IVD [102]. Histological examination can provide information about the composition of the disc and the presence of inflammatory cells [103].

Clinical evaluation of IVDD gives information about the onset, duration, and nature of the pain. The physical examination should include neurological examination to assess the presence of radiculopathy or myelopathy [104,105]. X-ray can provide information about the alignment of the spine but is not useful for assessing the disc itself. CT can provide information about the morphology of the disc but is not able to assess the soft tissue components of the disc. MRI is the gold standard for the diagnosis of IVDD as it can provide detailed information about the morphology and integrity of the disc. Discography involves the injection of contrast materials into the disc and can provide information about the presence of annular tears and fissures.

2.3.1.2 IVDD Treatment. There are several treatment options available for IVDD, including conservative, surgical, regenerative, and alternative treatments. [106]. The choice of treatment depends on the severity of the condition, the patient's individual needs and recommendations of the healthcare provider. Conservative treatments for IVDD aim to manage symptoms without surgery. These treatments may include physical therapy, exercise, medication, and lifestyle changes. Physical therapy and exercise can help improve spine mobility, strength, and flexibility, while medications such as nonsteroidal anti-inflammatory drugs (NSAIDs) can help manage pain and inflammation [107,108].

Surgical treatments for IVDD are typically reserved for cases that do not respond to conservative treatments or cases where there is a significant risk of permanent neurological damage. One common surgical treatment for IVDD is discectomy, which involves the removal of portions of the damaged IVD to relieve the pressure on the spinal cord or nerve roots [109,110]. Another surgical option is spinal fusion, which involves fusing two or more vertebrae together to stabilize the spine and prevent further degeneration [111].

Regenerative treatments for IVDD aim to promote the growth and regeneration of damaged IVD tissue. These treatments may include cell therapy, platelet-rich plasma (PRP) therapy, and growth factor injections [112]. Stem cell therapy involves injecting stem cells into the damaged IVD to promote tissue repair and regeneration [113]. PRP therapy involves injecting a concentrated dose of platelets, which contain growth factors, into the damaged disc to stimulate healing. Growth factor injection involves injecting specific growth factors into the damaged disk to promote tissue regeneration.

2.3.2 Surgical Solutions and Shortcomings

Surgical treatments are an important option for managing intervertebral disc disease when conservative treatments fail. Discectomy, spinal fusion, and artificial disc replacement are all effective procedures, but they also have certain shortcomings that should be considered. Discectomy is the surgical removal of part or all damaged IVD. this procedure aims to relieve pressure on the Spinal cord or nerve roots caused by herniated or degenerative disc. While discectomy is generally safe and effective, it has a higher risk of recurrent disc herniation and spinal instability compared to other surgical procedures [114,115]. Additionally, discectomy may not be suitable for certain types of disc herniation such as sequestered or extruded discs.

Spinal fusion is a surgical procedure that involves fusing two or more vertebrae together to stabilize the spine and prevent movement between the affected vertebrae. Spinal fusion can be performed using bone grafts or synthetic materials and it may be augmented with metal implants [116]. While spinal fusion can provide relief for IVDD, it also has several potential complications, such as risk of adjacent segment disease (ASD), which is the development of IVDD in the spinal segment above or below the spinal fusion site. Additionally, spinal fusion can limit the range of motion and flexibility of the spine, leading to stiffness and discomfort.

Artificial disc replacement (ADR) is a procedure that involves replacing the damaged intervertebral disc with a prosthetic disc. This procedure aims to preserve the natural motion of the spine while providing support and reducing pain. ADR has several advantages over spinal fusion, including a lower risk of ASD and greater flexibility in the spine. However, ADR is small complex procedure that requires a highly skilled surgeon and may not be suitable for all patients, such as those with severe osteoporosis or spinal deformities [117].

2.4 Tissue Engineering

2.4.1 Overview

Tissue engineering has emerged as a promising approach for the treatment of IVDD. The approach to tissue engineering for IVD treatment typically involves three components: scaffold materials, cells, and growth factors. Scaffolds are engineered materials that serve as a template for tissue growth [38,45,62]. They provide a physical structure for cells to attach, proliferate, and differentiate. The scaffold material used for intervertebral disc tissue engineering must be biocompatible, biodegradable, and able to withstand mechanical loads. Various materials have been studied, including natural materials such as collagen, hyaluronic acid, and chitosan, and synthetic materials such as poly (lactic-co-glycolic acid) (PLGA), polycaprolactone (PLA), and polyurethane (PU) [37,39,62,118].

Cells are another critical component of tissue engineering for IVDD treatment. The ideal cell source for IVD tissue engineering remains a subject of investigation, but mesenchymal stem cells (MSCs) have been shown to be a promising option [119,120]. These cells can differentiate into multiple cell types, including those found in the IVD, and have anti-inflammatory and immunomodulatory properties. Other cell types such as chondrocytes and nucleus pulposus cells, have also been studied [121]. Growth factor proteins are also essential in IVD tissue engineering [122]. Growth factors can promote cell proliferation, differentiation, and tissue regeneration. Various growth factors, such as transforming growth factor- beta (TGF-β), bone morphogenic protein (BMP), and fibroblast growth factor (FGF), have been investigated for IVD tissue engineering[123].

One approach to IVD tissue engineering involves seeding cells onto a scaffold and then implanting that construct into that IVD space [124,125]. In animal models, this approach has shown promising results in promoting tissue regeneration and reducing disc degeneration. However, challenges remain, such as ensuring appropriate mechanical properties of the scaffold and creating an environment conducive to cell survival and the differentiation[126]. Another approach is to inject cells and growth factors directly into the IVD. While the direct injection of cells and growth factors into the Intervertebral Disc

(IVD) presents as an innovative approach, there are significant challenges that need to be addressed. One major concern is the tendency of cells to migrate out of the disc space due to the high Intradiscal Pressure (IDP). This migration often leads to the formation of undesirable cell types such as osteocytes, which can further complicate the treatment process. Furthermore, there is a lack of clarity on whether Mesenchymal Stem Cells (MSCs) can survive in the harsh environment of a degenerated disc. The optimal concentration of cells required for effective regrowth within the IVD is also unknown.

These factors are crucial for the success of the treatment, as they directly impact the regeneration process. Additionally, the process of puncturing the disc for injection itself poses risks, as it may lead to further degeneration of the disc. This risk needs to be carefully evaluated against the potential benefits of the treatment. Therefore, while the direct injection of cells and growth factors into the IVD holds promise, these significant challenges highlight the need for further research and development in this area. This method has shown promising results in preclinical studies, but clinical trials are needed to determine its safety and efficacy in humans[127,128].

2.4.2 Cell Therapy

Several different types of cells have been explored as potential candidates for cell therapy in IVD degeneration, including MSCs, chondrocytes, and NP cells [129,130]. MSCs have received particular attention due to the appetence cell to differentiate into a range of cell types and their immunomodulation properties [131]. Numerous studies have reported promising results from MSC-based therapies for IVD degeneration in animal models and small-scale clinical trials [132]. For example, studies have shown that MSC transplantation can promote extracellular matrix production, reduce inflammation, and improve IVD structure and function [133].

However, while cell therapy for IVD degeneration shows promise, several challenges and limitations need to be addressed before it can be widely used in clinical practice. ell therapy for intervertebral disc (IVD) degeneration faces several shortcomings that hinder its widespread application. A significant challenge lies in the absence of standardized protocols for cell isolation, expansion, and transplantation. This lack of standardization leads to inconsistent outcomes among different studies, making it difficult to compare and draw reliable conclusions. Another limitation is the issue of cell survival and retention within the harsh microenvironment of the degenerated IVD. The unfavorable conditions impede the transplanted cells' ability to survive and integrate effectively into the tissue [134–137]. Additionally, there is a concern regarding the potential for tumorigenesis, especially with the use of mesenchymal stem cells (MSCs), which have exhibited tumor-promoting properties in certain contexts. Cells have been found to migrate out of the disc space due to high IDP. Once they migrate, they form undesirable cells such as osteocytes. Additionally, we don't know if MSCs would survive in a degenerated disc environment, what concentration of cells is necessary for regrowth, and if more degeneration would occur after puncturing a disc. Furthermore, ethical and regulatory considerations surrounding the acquisition and utilization of human cells pose additional challenges to the advancement of this therapy. To overcome these shortcomings, further research is imperative. Optimization of cell isolation, expansion, and transplantation protocols is necessary to enhance the consistency and effectiveness of cell therapy for IVD degeneration.

2.4.3 Scaffolds

Tissue engineered scaffolds are three-dimensional (3D) structures that provide a framework for cells to attach, proliferate, and differentiate, ultimately leading to the formation of functional tissue [138]. Scaffolds act as temporary extracellular matrices (ECMs) that mimic the natural microenvironment and facilitate cell-matrix interactions. They serve as a mechanical support to maintain tissue shape and integrity, while also providing spatial cues to guide cell behavior and tissue regeneration processes. Scaffolds can be designed to deliver bioactive molecules, such as growth factors or drugs, and can serve as templates for tissue formation or as vehicles for cell transplantation [139–141].

The properties of tissue engineered scaffolds play a critical role in determining the success of tissue regeneration. Various scaffold characteristics influence cell behavior, including attachment, migration, proliferation, and differentiation, which are crucial for the development of functional tissues. Key scaffold properties include porosity, pore size distribution, mechanical properties, surface topography, biocompatibility, and degradation kinetics [142]. The choice of scaffold materials, fabrication techniques, and design parameters must be carefully considered to meet the specific requirements of the target tissue or organ. Additionally, the interaction between cells and scaffolds, including cell adhesion, signaling, and nutrient transport, must be optimized to promote cell survival and tissue integration [143,144].

Understanding the role of tissue engineered scaffolds and their impact on tissue regeneration is essential for advancing the field of regenerative medicine. By continually refining scaffold design and fabrication techniques, researchers can enhance the functionality, biocompatibility, and regenerative potential of scaffolds, ultimately leading to improved clinical outcomes and the development of innovative therapies for a wide range of medical conditions.

The design of tissue engineered scaffolds involves careful consideration of several factors to optimize their performance and efficacy. The scaffold architecture can be tailored to mimic the native tissue structure, such as hierarchical or anisotropic arrangements, to provide mechanical support and guide tissue formation. The porosity and pore size distribution influence cell infiltration, nutrient diffusion, and waste removal within the scaffold, affecting cell viability and tissue regeneration. Interconnectivity between pores ensures the efficient exchange of nutrients and waste products throughout the scaffold. The surface characteristics, including topography and chemistry, can modulate cell adhesion, proliferation, and differentiation, thus influencing tissue regeneration outcomes [145].

Several conventional techniques have been used for fabricating tissue engineered scaffolds. Salt leaching involves mixing a biocompatible polymer with salt particles, which are subsequently dissolved, leaving behind a porous structure. Solvent casting involves creating a solution or suspension of the desired polymer and then casting it into a mold to evaporate the solvent and form a scaffold. Electrospinning utilizes an electric field to draw polymer fibers from a solution or melt, creating a nonwoven, fibrous scaffold [146]. These techniques offer simplicity, versatility, and control over scaffold properties, but they may have limitations in terms of pore size control, reproducibility, and scalability.

Advancements in technology have led to the development of more sophisticated scaffold fabrication techniques with improved control over scaffold properties. Three-dimensional (3D) printing enables precise spatial control and layer-by-layer deposition of biomaterials, allowing the creation of complex structures with customized pore architectures [147]. Bioprinting takes 3D printing a step further by incorporating living cells into the printing process, enabling the creation of cell-laden constructs with high cell density and spatial organization [148]. Electrohydrodynamic jetting utilizes electrical forces to form droplets or fibers from a polymer solution, enabling the fabrication of scaffolds with fine resolution and controlled fiber alignment. These advanced techniques offer enhanced versatility, reproducibility, and customization, enabling the creation of scaffolds that better mimic the native tissue microenvironment.

Hybrid scaffolds combine multiple materials or fabrication techniques to leverage the advantages of each component [149]. For example, a scaffold may consist of a natural biomaterial combined with a synthetic polymer or incorporate different fabrication techniques to create complementary structures. Hybrid scaffolds can offer improved mechanical properties, bioactivity, and cell-matrix interactions. By combining different materials, researchers can tailor scaffold properties, such as stiffness, degradation rate, and bioactive molecule release kinetics, to better match the requirements of the target tissue. Hybrid scaffold designs allow for the incorporation of multiple cell types or growth factors, facilitating complex tissue regeneration processes [150,151].

Natural materials derived from biological sources, such as collagen, fibrin, alginate, and chitosan, have been extensively explored for tissue engineered scaffolds. Collagen, the most abundant protein in the body, offers excellent biocompatibility and biodegradability. It provides structural support and can promote cell adhesion, migration, and tissue remodeling. Fibrin, a natural polymer formed during the blood clotting process, possesses cell-adhesive properties, and supports cell proliferation and angiogenesis [152,153]. Alginate, a polysaccharide derived from seaweed, forms hydrogels that can encapsulate cells and deliver bioactive molecules. Chitosan, derived from the chitin found in crustacean shells, exhibits antimicrobial properties, and can promote cell adhesion and differentiation.

Synthetic polymers have also been widely employed in tissue engineered scaffolds due to their tunable properties and controllable degradation kinetics. Polycaprolactone (PCL) and poly (lactic-co-glycolic acid) (PLGA) are commonly used synthetic polymers. PCL exhibits good mechanical properties and slow degradation rates, making it suitable for long-term tissue regeneration applications. PLGA is a biodegradable and biocompatible polymer that can be tailored to degrade at specific rates depending on the desired tissue regeneration timeline. Other synthetic polymers, such as polyethylene glycol (PEG), polyurethane (PU), and polyethylene oxide (PEO), have also been investigated for their unique properties, including hydrophilicity, elasticity, and controlled degradation.

Composite materials combine natural and synthetic polymers or incorporate other components, such as ceramics or nanoparticles, to create scaffolds with enhanced properties. By blending different materials, researchers can exploit the advantages of each component to achieve a synergistic effect. For example, incorporating ceramic particles, such as hydroxyapatite, into a polymer matrix can improve the mechanical strength and bioactivity of the scaffold for bone tissue engineering applications. Nanoparticles, such as silver or gold nanoparticles, can be incorporated to confer antimicrobial properties or facilitate controlled drug delivery.

Table 3

Biomaterials Used for AF Tissue Engineering [40]

AF tissue engineering scaffold	Biomaterials
Single unit without fiber orientation	Atelocollagen honeycomb
	Collagen-glycosaminoglycan
	Alginate/Chitosan
	Poly (1,8-octanediol malate)
	Poly-D-L-lactide/Bio glass
	Silk
	Genipin crosslinked fibrin
Single unit with fiber orientation	Aligned alginate/chitosan
	Polycarbonate polyurethane linked with dihydroxyl oligomer
	Polycaprolactone
	Poly-L-Lactide
	Silk fibers/chondroitin sulphate
	Collagen fibrils
Biphasic scaffold	Poly (polycaprolactone triol malate)/DBM
Composite scaffold	Poly-L-Lactide as AF and hyaluronic acid hydrogel as NP
	Polyglycolic Acid/poly-l-lactic as AF and alginate hydrogel as NP
	Silk scaffold as AF and silicon as NP or hyaluronic acid as NP
	Polycaprolactone fibers as AF and agarose gel as NP
	Collagen gel as AF and Polyethylene/alginate as NP

Bioactive materials, including hydroxyapatite, bioactive glasses, and decellularized extracellular matrix (ECM) components, have gained significant attention in tissue engineering. Hydroxyapatite (HA), a calcium phosphate mineral found in natural bone, provides an osteoconductive scaffold material that can promote bone tissue regeneration. Bioactive glasses, such as silica-based glasses, stimulate the formation of a biologically active layer on the scaffold surface, facilitating cell attachment and bone regeneration. Decellularized ECM components derived from tissues or organs preserve the native tissue architecture, biochemical cues, and mechanical properties, creating an ideal microenvironment for cell infiltration, proliferation, and differentiation.

The choice of scaffold materials in tissue engineering is crucial as it directly influences scaffold biocompatibility, mechanical properties, degradation rates, and interaction with cells and surrounding tissues. Advances in biomaterials research continue to expand the range of materials available for scaffold fabrication, enabling researchers to develop tailored scaffolds that closely mimic the properties of native tissues. By selecting appropriate scaffold materials and optimizing their characteristics, tissue engineers can create scaffolds that promote cell adhesion, proliferation, and tissue-specific differentiation, leading to successful tissue regeneration.

2.4.3.1 Tissue Decellularization. Tissue decellularization is a process that involves the removal of cellular components from donor tissues while preserving the extracellular matrix (ECM) structure and bioactive molecules. This technique has gained significant attention in the field of regenerative medicine as it offers a potential solution for tissue engineering and the development of allografts and xenografts [154].

Allografts refer to the transplantation of tissues or organs between genetically non-identical individuals of the same species. Decellularized allografts offer several advantages over traditional allografts, which often face limitations such as immune rejection and limited availability of donor tissues. By removing the cellular components, including antigens and immune-stimulatory factors, from allografts, the risk of immune rejection is reduced. Decellularized allografts also retain the ECM structure and bioactive molecules, which can support cell attachment, proliferation, and tissue regeneration in the recipient [155,156]. These decellularized allografts can be used as scaffolds to promote the repopulation of recipient cells or as acellular matrices to facilitate tissue regeneration by endogenous cells. Additionally, decellularized allografts can be modified or functionalized to enhance their regenerative potential, such as though the incorporation of growth factors or immune-modulatory agents [157,158].

Xenografts, on the other hand, involve the transplantation of tissues or organs between different species. The decellularization of xenogeneic tissues presents a unique set of challenges due to the potential for immunological incompatibility and the risk of transmission of zoonotic diseases [159]. However, decellularized xenografts offer the advantage of providing a scaffold with an ECM architecture similar to that of human tissues. With careful decellularization techniques, xenografts can be rendered immunologically inert while maintaining the essential structural and biochemical components necessary for tissue regeneration. Research efforts are focused on overcoming the immunological barriers associated with xenografts and exploring methods to enhance their integration and long-term functionality.

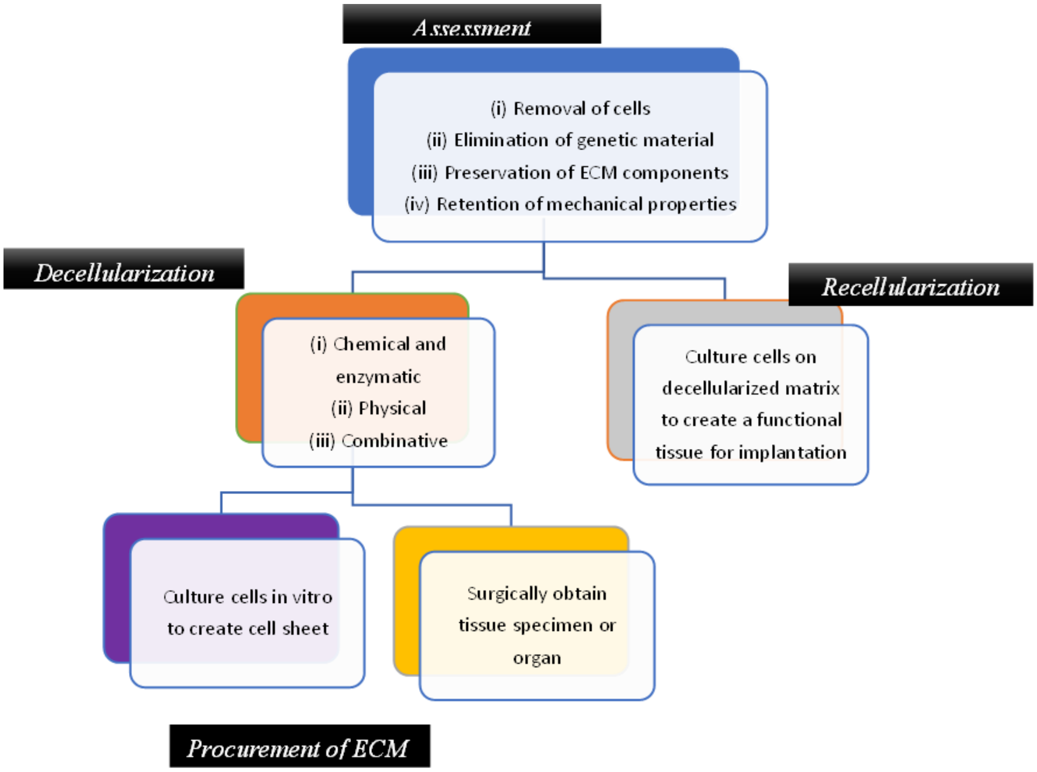

Figure 7. Process of Tissue Engineering using Native Scaffold

Tissue decellularization techniques typically involve a combination of physical, chemical, and enzymatic methods to remove cellular components while preserving the ECM structure. The choice of decellularization method depends on the specific tissue type, desired outcomes, and subsequent applications. Common decellularization agents include detergents, enzymes, and hypertonic or hypotonic solutions. The efficacy of decellularization is assessed by evaluating residual DNA content, histological analysis, and preservation of ECM components [160].

However, it is important to note that decellularized tissues, whether allografts or xenografts, still face challenges. The complete removal of cellular debris, preservation of ECM integrity, and mitigation of immunogenicity are ongoing areas of research. Improving the recellularization potential of decellularized tissues, ensuring proper revascularization, and enhancing long-term functionality are active areas of investigation [161–163].

2.4.3.2 Methods of Decellularization. Decellularization methods play a critical role in tissue engineering and regenerative medicine. Physical, chemical, and enzymatic techniques, either used individually or in combination, provide options for achieving efficient cellular removal and preservation of the ECM structure and bioactive molecules [8,164,165]. Understanding the advantages, limitations, and challenges associated with different decellularization methods is essential for the development of high-quality decellularized tissues with optimal regenerative potential. Further research is needed to optimize decellularization protocols, enhance recellularization strategies. The choice of decellularization method depends on various factors, including tissue type, size, complexity, desired ECM preservation, and subsequent applications. Optimization of decellularization protocols is crucial to achieve complete cellular removal while preserving the structural and biochemical integrity of the ECM. Monitoring techniques, such as histological analysis, DNA quantification, or assessment of residual cellular proteins, are employed to evaluate the efficacy of decellularization protocols.

Physical methods for tissue decellularization involve mechanical force or pressure to disrupt and remove cellular components from the tissue while preserving the ECM structure. Techniques such as freeze-thaw cycles, agitation, or mechanical stirring can aid in cell removal. Freeze-thaw cycles subject the tissue to repeated freezing and thawing, causing cell membranes to rupture and release cellular contents. Agitation methods involve shaking or stirring the tissue in a solution to dislodge cells. Physical methods are relatively simple and do not require the use of harsh chemicals; however, they may not achieve complete cellular removal and can potentially damage the ECM structure if not carefully controlled.

Chemical methods employ various agents to solubilize and remove cellular components from the tissue. Detergents are commonly used as decellularization agents due to their ability to disrupt cell membranes and solubilize cellular contents. Sodium dodecyl sulfate (SDS), Triton X-100, and 3-[(3-cholamidopropyl) dimethylammonio]-1-propanesulfonate (CHAPS) are examples of detergents utilized in decellularization protocols. These detergents effectively remove cellular proteins and lipids but may also compromise the structural integrity of the ECM if used excessively or for prolonged periods. Other chemical agents, such as chelating agents (e.g., ethylenediaminetetraacetic acid, EDTA) or hypertonic or hypotonic solutions, can be employed to aid in cell removal by disrupting cell membranes or inducing osmotic stress [166].

Enzymatic methods involve the use of enzymes to degrade specific cellular components and facilitate cell removal. Enzymes such as nucleases (e.g., DNase and RNase) are commonly utilized to degrade DNA and RNA, facilitating the removal of nuclear material. Proteolytic enzymes, including trypsin, pepsin, or collagenase, can be employed to degrade cellular proteins, facilitating cell detachment from the ECM. Enzymatic methods offer specificity in targeting cellular components, resulting in efficient cellular removal. However, the selection of appropriate enzymes and optimization of enzymatic digestion times and concentrations are crucial to avoid excessive ECM degradation.

Combination methods involve the use of multiple decellularization techniques to enhance cellular removal and preserve ECM integrity. For example, a combination of physical agitation, enzymatic digestion, and detergent treatment can be employed to maximize cell removal while minimizing the adverse effects on the ECM. These methods aim to achieve a balance between efficient decellularization and preservation of the essential ECM components. Combination methods can enhance decellularization efficacy and improve the quality of decellularized tissues, but they require careful optimization and validation.

Table 4

Summary of Decellularization Agents and Techniques [166]

Category	Agents and techniques	Mechanism/description	Significant effects
Chemical and enzymatic	(1) Surfactants	Lyse cells by disarranging the phospholipid membrane	
	Sodium dodecyl sulfate (SDS)	(i) Ionic	(i) Cytotoxic: requires extensive wash process (ii) Alters microstructure (i.e., collagen fibres)
	Triton X-100	(i) Non-ionic (ii) Commonly used with ammonium hydroxide	(i) Less damaging to structure of tissue than ionic surfactants
	Sodium deoxycholate (SD)	(i) Ionic (ii) Commonly used with DNase	(i) Causes agglutination of DNA when used without DNase (ii) Remnant DNA fragments
	CHAPS	(i) Zwitterionic	(i) Maintains structural ECM proteins (ii) Remnant cytoplasmic proteins (iii) Maintains ultrastructure
	(2) Acids and bases	Solubilize cell membrane by utilizing charged properties	(i) Insufficient cell removal (ii) Increases stiffness of ECM
	Peracetic acid	(i) Highly corrosive (ii) Oftentimes used for sterilization	(i) Insufficient cell removal (ii) Increases stiffness of ECM
	Ethylenediaminetetra acetic acid (EDTA)	(i) Commonly used with trypsin	(i) Decreases salt- and acid-soluble ECM proteins
	Reversible alkaline swelling	(i) Induces negative charge on collagen to cause swelling (ii) Used with tridecyl alcohol ethoxylate	(i) Alters mechanical properties
	(3) Enzymes	Typically used to supplement other chemical & mechanical treatments.	
	Trypsin	(i) Breaks cell-matrix adhesions (ii) Commonly used with EDTA	
	Deoxyribonuclease (DNase)	(i) Breaks down DNA fragments (ii) Commonly used with SD	
	Ribonuclease (RNase)	(i) Breaks down RNA fragments	
Mechanical	High hydrostatic pressure (HHP)	(i) Pressures greater than 600 MPa applied to lyse cells	(i) Remnant DNA fragments (ii) Denatures ECM proteins
	Supercritical carbon dioxide	(i) Applies CO2 at pressures above 7.40 MPa and temperatures above 31.1∘ C	(i) Requires entrainer to remove polar phospholipid membrane (ii) Maintains ECM proteins & mechanical properties
	Freeze-thaw	(i) Alternate between freezing temperatures (−80∘ C) and biological temperatures (∼37∘ C)	(i) Maintains ECM proteins & mechanical properties (ii) Remnant DNA

2.5 Pulsed Electric Fields

In 1982, the concept of membrane electroporation was introduced for the first genetic reprogramming of cells with naked DNA by using electric pulses[167]. This electric field phenomenon was termed membrane “electroporation”, to represent “electric pore formation”[167]. Electroporation is the increase in the permeability of the cell membrane to ions and macromolecules which would ordinarily not permeate the cell membrane by exposing the cell to high energy short electric pulses. The increase in membrane permeability is presumed to be related to the formation of nano-scale defects or pores induced by the electric fields[168]. Biological membranes play a critical role in all living organisms. This flexible structure around the cells envelopes the cell and its organelles, it acts as a selective filter towards ion and molecule transport to maintain a concentration gradient in the cell cytoplasm.

When short and intense electric pulses are applied to cells, transient changes occur in the membrane that makes it permeable to various ions and molecules. This phenomenon is due to the interaction between the membrane and the electric fields. The strong electric fields destabilize membranes causing charge redistribution over the membrane bilayer and inducing charges in the structure[169]. A trans-membrane potential is induced by the external electric field due to the difference in the electric properties of the membrane and the external medium. The electric conductivity of the cell membrane at physiological conditions is much lower than the cytoplasm and the extracellular medium. When the externally induced transmembrane potential is high enough, the membrane potential threshold is passed and membrane permeabilization occurs leading to perturbation of the membrane structure and increase in the membrane permeability [169,170]. Depending on the parameters of the applied electric field and membrane conditions, the observed membrane changes can be reversible [169,170] or irreversible [168,171].

Membrane permeabilization has diverse biotechnological applications. In the food industry, pulsed electric fields are employed to increase the extraction of lipids, production of wine, juice, and olive oil. Food products are cold sterilized by irreversible electroporation of bacteria and yeast to preserve the taste. Electro transfer is also used in genetically modified organisms in gene engineering[167]. In medicine, pulsed electric fields are used to enhance penetration and drug uptake and DNA plasmids delivery in electrochemotherapy and electrogenetherapy processes respectively[168]. Irreversible electroporation provides a nonthermal approach to removal of undesirable cells in tissues which is a potential in tissue decellularization for scaffold creation for regenerative tissue engineering. The sections that follow shall discuss the basic electrical concept of tissue electroporation, tissue electrical properties and the electrochemical interface formed between the electrode and tissue.

2.5.1 Basic Electrical Concept of Tissue Electroporation

To understand electroporation, the concept of electromagnetism is required. In tissue electroporation, non-conducting biological tissue materials are exposed to electric fields from alternating voltage or current source[168]. The concepts of the electric fields come from the current-voltage relationship for R, L and C in circuit theory. The applied electricity parameters are defined in table 5 below.

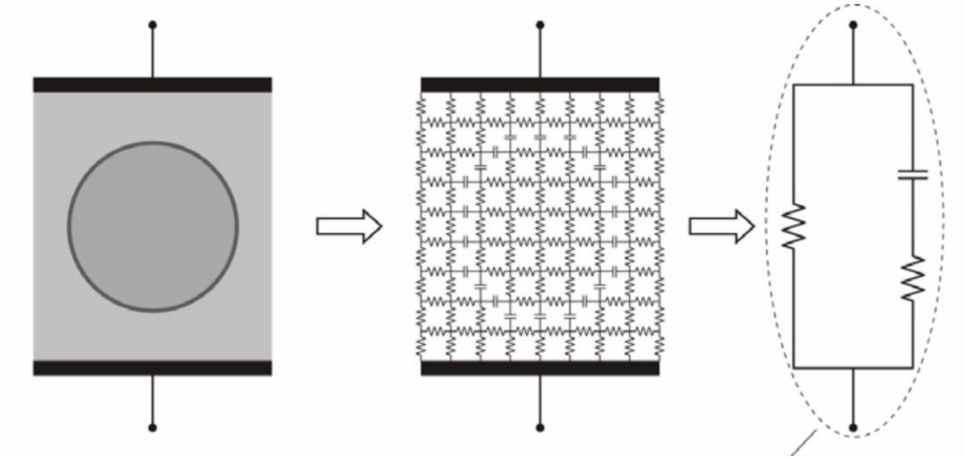

Figure 8. Electrical Representation of a Cell between Electrodes

The Fick's model from the twenties gives a good approximation of the electrical properties of a biological cell[172168]. The model is based on a spherical cell in extracellular. Figure 8 below shows the electrical scheme according to Fick where the extracellular compartment is modeled a resistance in parallel with the intercellular compartment also modeled as a resistance in series with the cell membrane modeled as a capacitance. The intra and extracellular media are ionic solutions with Na+ and Cl- being the most abundant ions in the extracellular medium and K+ in the intracellular medium hence the resistive behavior[168]. The cell membrane is made of lipid by layer with a very low intrinsic conductivity hence the membrane is considered a good dielectric. With circuit theory, the elements are combined to form a single equivalent circuit. Multiple cells are combined so that the same electrical model can be used to characterize the electrical properties of a biological tissue.

Table 5

Basic Applied Electricity Parameters

Parameter	Definition	Formula	Unit
Voltage, V	Energy of a unit charge at a point A compared to the energy of the unit charge at a point B.	$V = IR$ $V = E \times L$	Volt, V
Electric field, E	Region around a charge particle that the electric charge force can be experienced by another charged particle or object.	$E = \frac{Q_1 Q_2}{d}$ $E = \frac{V}{d}$	V/cm
Current, I	Flow of charges across a voltage difference.	$I = \frac{V}{R}$	Ampere, A
Resistance, R	It is the material property that impedes flow of current though it.	$R = \frac{V}{I}$	Ohm, Ω
Conductance, G	Measure of current flow in a material. Inverse of resistance.	$G = 1/R$	Siemens, S
Power, P	Work done	$P = VI = I^2 R = \frac{V^2}{R}$	Watt, W
Current density, J	Current flow per unit area	$J = A/S$	A/m^2
Resistivity, $\boldsymbol{\rho}$	Resistance of each infinitesimal portion of a conductive medium.	$\rho = \frac{E}{J}$	$\Omega . m$
Conductivity, $\boldsymbol{\sigma}$	Inverse of resistivity.	$\sigma = 1/\rho$	S/m
Energy dissipated, U		$U = P * t$	Joule, J
Temperature Rise, $\boldsymbol{\Delta T}$		$\Delta T = \frac{U}{cd}$	Kelvin, K
Capacitance, C	Ability to store charges	$C = \varepsilon \frac{A}{L}$	Farad, F

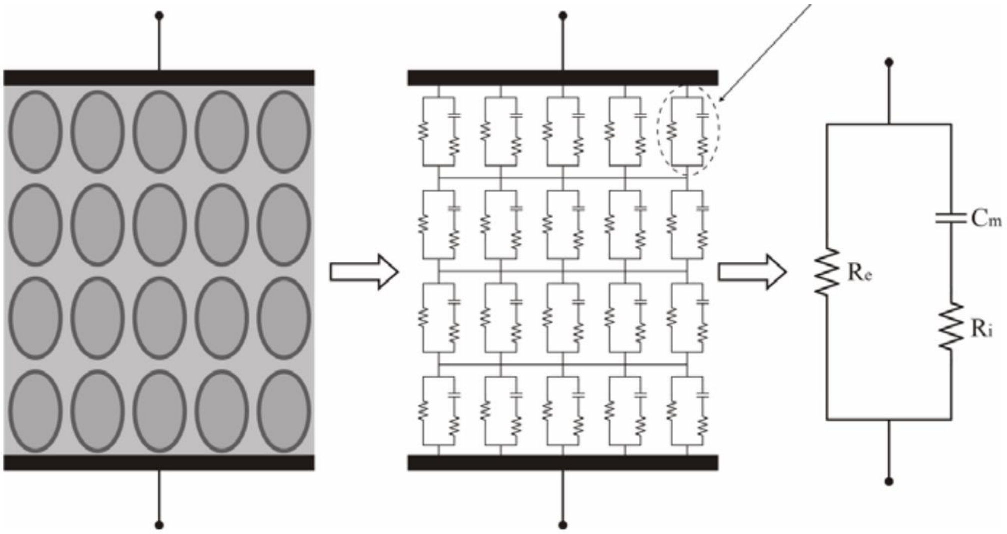

Figure 9. Electrical model of a biological tissue represented by multiple cells combined in an electrical circuit

Based on the Fick's model, the simple RC circuit means the permittivity is independent of frequency. The tissue has been demonstrated to show a frequency-dependent behavior. The Cole electrical circuit model incorporates a constant impedance phase element (CPE) in the tissue electrical circuit diagram to represent the frequency dependence[172]. The model represents the tissue as an equivalent electrical circuit with a low frequency resistance R0 as the extracellular compartment, a high frequency resistance R∞ which represent the intracellular compartment and the cell membrane and a non linear capacitor CPE[172]. The τ the charecteristic time constant of the tissue and the α relates the heterogeneity of cell size and morphorlogy of the tissue[172]. In Figure 10, the biological tissue is not a conducting material as mentioned earlier. It is a dielectric material; it does not conduct charge but support the accumulation of charges. This is discussed in detail in the next section.

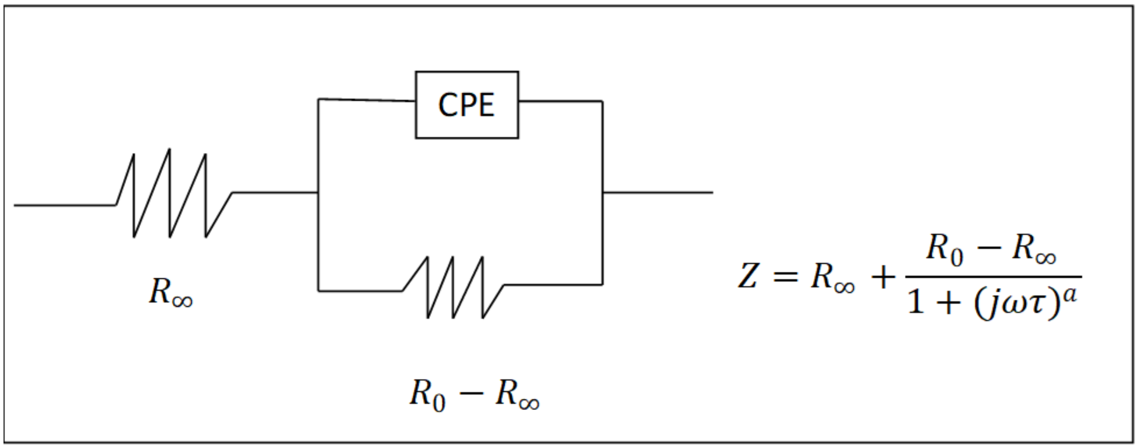

Figure 10. The Cole-Cole Electrical Model of a Biological Tissue

2.5.2 Dielectric Properties of Biological Tissue

The dielectric properties of a material generally describes the electric charge movement inside the material in response to an externally applied electric field[173]. Biological tissue dielectric properties can help in understanding and physiologically differentiating between normal and cancerous (diseased) tissue at the molecular level and the nature of the physical state of water in a biological system[174]. The dielectric properties of biological tissue are highly dependent[173,175] and is determined by the frequency variations in the tissue relative permittivity and electrical conductivity[173,174,176].

At low external field strength, the dielectric properties are independent of the external field strength. For an external field E applied to a material, a current density J will be induced inside the material [173]:

$$J = (\sigma_s + \omega\varepsilon_o\varepsilon'')E + j\omega\varepsilon_o\varepsilon' E \tag{1}$$

$$= \sigma E + j\omega\varepsilon_o\varepsilon' E$$

where σ_s is the conductivity of the material, ω is the angular frequency of the applied field, ε_o is the permittivity of free space, ε'' is the loss factor, ε' is the dielectric constant and conductivity σ. The dielectric constant and conductivity are related by [173]

$$\sigma = \sigma_s + \omega\varepsilon_o\varepsilon'' \tag{2}$$

For biological tissue, ionic conduction is the main contributor to σ_s whereas $\omega\varepsilon_o\varepsilon''$ is from the tissue dielectric relaxation. A basic circuit representation of the tissue dielectric is illustrated in figure 11.

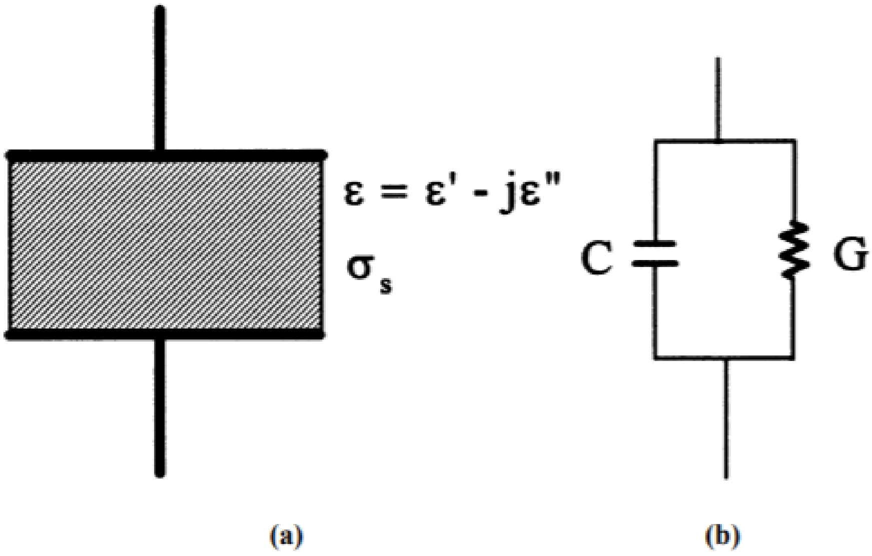

Figure 11. A Basic Circuit Representation of the Tissue Dielectric. (a) A dielectric material between a parallel plate electrode. (b) Circuit diagram of a frequency-dependent model with a capacitance C and conductance G

When a dielectric material is exposed to electrical fields, the distribution of polar molecules in the material is disturbed and reoriented[173,175]. This phenomenon is known as dielectric relaxation and the associated time constant is the relaxation time, τ. Like other dielectric properties, the dielectric relaxation of a biological tissue is frequency dependent and is characterized by the relaxation time. This is given by the Debye equation:

$$\varepsilon = \varepsilon_{\infty} + \frac{\varepsilon_{s} - \varepsilon_{\infty}}{1 + j\omega\tau} \tag{3}$$

where ε_{∞} is the dielectric constant at higher frequencies greater than the characteristic frequency $f_c = 1/2\pi\tau,$ and ε_s is the dielectric constant at low frequencies[173].

2.5.2.1 Tissue Bioimpedance. Bioimpedance is a passive electrical property that describes the ability of a biological tissue to impede current flow. The dielectric properties of a tissue changes with the application of pulsed electric fields[172], this causes variation of the impedance with the local electric field leading to redistribution of the electric field[177]. The bioimpedance of a tissue depends on the tissue type and applied electrical field. Multiple microscopic process occurs to give an overall response when a biological tissue is electrically stimulated. The applied voltage induces the release of metal ions that alters the sample around the electrode changing the conductivity of the tissue. The electrical impedance of a biological tissue is dependent on the tissue composition, anatomy and the frequency of the applied field[178].

Bioimpedance measurement represents a method of monitoring variations in a biological tissue. Bioimpedance measurement is used to differentiate between a normal tissue and a cancerous tissue. It is widely employed to characterize the behavior of complex systems. The extent of permeabilization of a tissue can be measured by the bioimpedance measurement and can also be a method to monitor real time physiological changes to tissue exposed to electric fields. The impedance spectroscopy can be used to characterize the charge distribution at the interface of a sample and the electrodes[172,177]. Impedance measuring techniques vary based on whether the independent variable is frequency or time[172]. When cells are exposed to an electric field, the cell membrane acts as an insulator and does not allow the current to pass though the cell. The insulating ability of the membrane decreases with increasing frequency of the applied field. At a frequency of 1 MHz, the membrane no longer present a barrier to current flow[172].

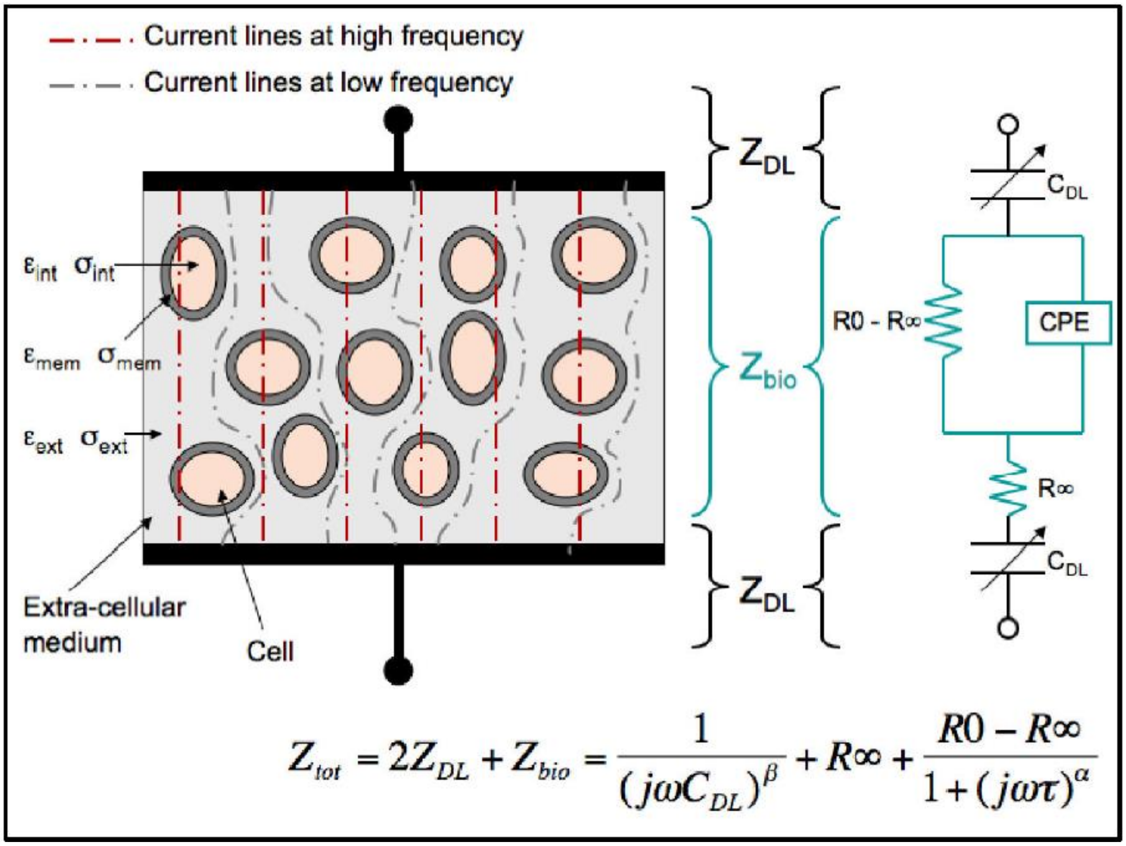

$$Z_{tot} = 2Z_{DL} + Z_{bio} = \frac{1}{(j\omega C_{DL})^{\beta}} + R\infty + \frac{R0 - R\infty}{1 + (j\omega\tau)^{\alpha}}$$

Figure 12. Cell Tissue Electrical Model showing Current Path for Different Frequencies

The standard approach to impedance measuring is to send a voltage or current signal though the electrodes into the sample measuring the amplitude of the impedance phase shift. There are two electrode configurations used for the impedance measurement: 4-probe method and 2-probe method. For the 4-probe method, a pair of electrodes send current signals into the sample and another pair of electrodes measure the current drop across the sample. The impedance measurement relates to the conductivity and permittivity of the tissue[172]. The 2-probe method has two electrodes sending current into the sample and the same electrodes measure the voltage drop across the sample. in this configuration, the voltage drop measured is due to the electrodes and the sample hence a substitution method is employed to deduce the impedance of the sample.

The state of increased permeability of the plasma membrane to molecules and ions as a result of short-duration, high intensity electric field exposures that represent the basis of electroporation has direct consequences on the electrical properties of exposed biological samples [179]. Sudden fluctuation is detected in tissue electrical conductivity as a result of the plasma membrane pore opening when exposed to pulsed electric fields. Studies have reported comprehensive characterization of electropermeabilization with conductivity changes in different biological cells and tissues both in vitro and in vivo [179–182]. For instance, Beitel-White et al. (2022) treated pancreas, liver and brain tissues with IRE and measured the electrical conductivity response to the applied pulses. The study reported an increase in conductivity for all thee tissues, however, the tissue conductivity was dependent on the tissue type [183]. There is ongoing research to develop and improve technology to provide real-time feedback control systems to optimize electroporation based treatment such as non-thermal irreversible electroporation NTIRE [179,181,184].

2.5.3 Non-Thermal Irreversible Electroporation

Non-thermal irreversible electroporation (NTIRE) is an emerging minimally invasive technique used for tissue ablation and targeted cell death. Unlike thermal-based ablation methods such as radiofrequency or microwave ablation, NTIRE utilizes pulsed electric fields to induce irreversible permeabilization of cell membranes, leading to cell death while preserving the surrounding tissue architecture and extracellular matrix. NTIRE involves the application of short, intense electric pulses to the target tissue. The electric pulses create high-intensity electric fields within the tissue, leading to the formation of nanopores in the cell membrane lipid bilayer. These nanopores disrupt the cell membrane's structural integrity and induce a loss of cell homeostasis, resulting in irreversible cell death. The electric pulses are carefully controlled to avoid thermal effects and ensure selective destruction of the target cells.

NTIRE exhibits a unique ability to selectively target certain cell types while preserving surrounding tissues. The susceptibility of cells to NTIRE-induced cell death is primarily determined by their size, membrane composition, and electrical properties. Smaller cells and cells with higher transmembrane potentials are more susceptible to NTIRE. This selectivity allows for precise targeting of specific tissues or structures, minimizing damage to nearby critical structures. One of the major advantages of NTIRE is its ability to preserve the extracellular matrix (ECM) and tissue architecture. Unlike thermal ablation techniques that induce coagulative necrosis, NTIRE causes non-thermal cell death, leaving the ECM intact. This preservation of the ECM is particularly important in tissues with complex structures and functional roles, such as blood vessels, nerves, or delicate organs.

NTIRE has shown promising results in various clinical applications. It has been successfully utilized in the treatment of solid tumors, including liver, pancreas, prostate, and lung cancers. NTIRE can effectively ablate tumor cells while minimizing damage to adjacent critical structures, such as blood vessels or bile ducts. Additionally, NTIRE has shown potential in the treatment of atrial fibrillation, benign prostatic hyperplasia, and other conditions where targeted cell death is desired.

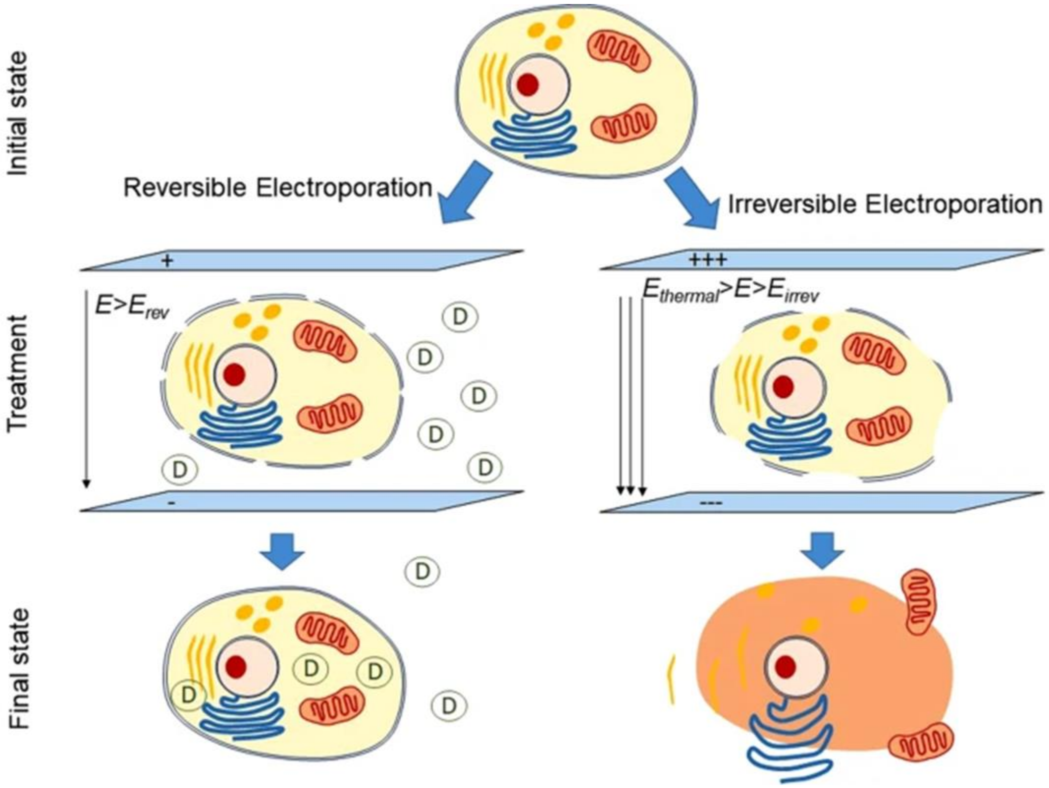

Figure 13. Reversible Electroporation (RE) (Left) and Irreversible Electroporation (IRE) (Right)

The electrical properties of tissues, as reflected by their bioimpedance, can influence the efficiency and safety of the electroporation process. Tissue impedance affects the distribution of the applied electric field during electroporation. Tissue heterogeneity causes varying electrical conductivities and resistivities in the tissue which leads to variations in the electrical distribution [185]. Higher impedance tissues tend to experience higher voltage drop. This non-uniformity can impact the efficacy and consistency of electroporation across the tissue. Tissue with high impedance generally corresponds to higher membrane resistance and can make it more challenging to induce permeabilization during electroporation [186,187]. Hence, higher electric field thresholds are required to induce electroporation in tissues with higher bioimpedance. The consequence of higher electroporation threshold is the undesired Joule heating associated with the current passing though the tissue [188–190]. Joule heating makes the tissue more susceptible to adverse effects such as thermal damage.

Beyond the permeabilization of the plasma membrane, the application of electric fields facilitates the movement of molecules and ions across membranes and tissues, a phenomenon known as electrokinetic transport. Electrokinetic transport can be influenced by the electrical properties of tissue [191]. For example, the movement of ions or charged molecules during electrophoresis across tissues can be influenced by the tissue's electrical conductivity or impedance [192]. Similarly, the flow of fluid during electroosmosis can be affected by the tissue's electrical properties [193].

2.5.4 Electrokinetic Transport in Tissue

At phase boundaries of biological interphases, charge separation naturally occurs forming an electrical double layer (EDL) of charges with opposite charges in each adjacent phase. The electrical double layer plays an important role for coupling electrical, mechanical, and chemical events in biological tissues. The electrical properties of such a layer are very important since they significantly affect the electrochemical properties and measurements. The existence of EDL at the surface of the electrode in contact with the electrolyte appeared in 1879 (Helmholtz). The Helmholtz model assumed a compact layer of ions in contact with the metal electrode. The Gouy and Chapman model was followed by proposing a diffuse double layer in which the ions accumulate due to the Boltzmann distribution, and extends some distance from the solid surface [194]. Later developments suggested that the EDL was an electrified solid-liquid interface which includes the rigid and diffuse layer models by Stern (1924).

Several models of the EDL have been proposed over the years. A classic, simplified model of the EDL formed at the electrode-electrolyte interface is presented in Figure 14. The EDL forms a capacitor which must be charged, which means that capacitive current, not related to the reduction or oxidation of the electrode flows in the electrical circuit []. The composition of the EDL influences the electron transfer rate. As seen in Figure 14, there is a layer of adsorbed water molecules on the electrode surface. As a result of the excess negative charge at the electrode surface, the hydrogen atoms in the adsorbed water molecules are oriented toward the electrode surface.

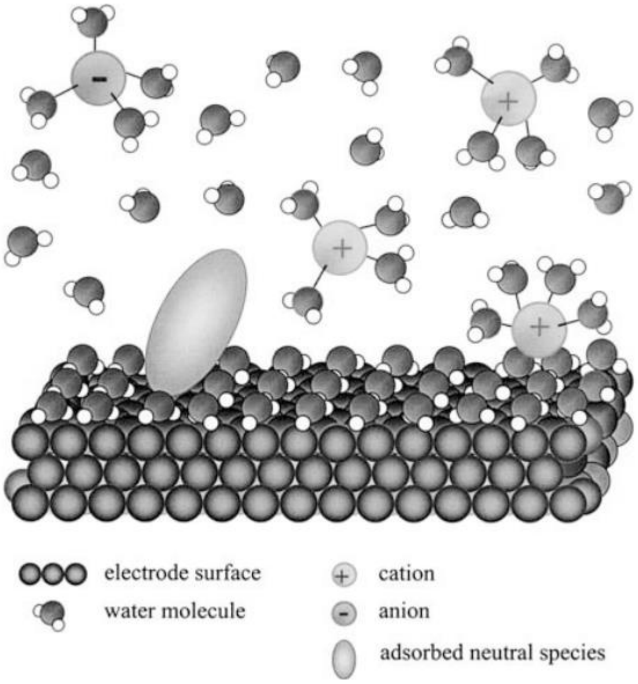

Figure 14. Representation of the Electrical Double Layer Formed at the Electrode-Electrolyte Interface

Two planes are associated with the double layer, the inner Helmholtz plane (IHP) passing though the center of the adsorbed ions, and the outer Helmholtz plane (OHP) passing though the center of the hydrated ions that are in contact with the electrode surface. The electric potentials of the IHP and OHP are usually written as $\psi_1$and ψ_2, respectively. The concentration of cations in the EDL decreases exponentially with the distance from the electrode surface. Assuming a negatively charged electrode surface, electric potentialϕ_M, remains constant in the metallic phase. The potential drops across the IHP and OHP of the EDL, and remains almost constant in the solution, ϕ_s, as shown in Figure 15.

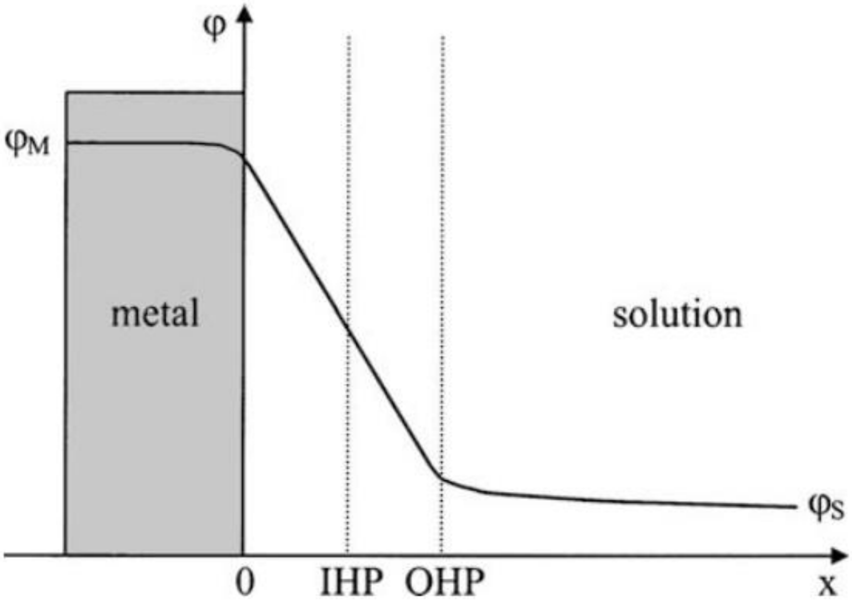

Figure 15. Electric Potential Profile in the EDL at the Electrode-Electrolyte Interface of a Negatively Charged Electrode

An imposition of an external potential to the electrode results in the generation of a charge, σ_M, on the metal and a charge, σ_S, in the solution. The charge at the electrode is directly related to the EDL or interfacial capacitance and can be described in two ways: The differential capacitance, C_d, at the minimum for the potential of zero charge which is represented by Eq. (4):

$$C_d = \frac{\partial \sigma_M}{\partial E} \tag{4}$$

The integral capacitance, C_i, described by Eq. (5):

$$C_i = \frac{\sigma_M}{E - E_{\sigma=0}} \tag{5}$$

The thickness of the double layer is usually approximated to be $1.5\kappa^{-1}$, where κ^{-1} is the Debye-Huckel length:

$$\kappa^{-1} = (\varepsilon_r \varepsilon_0 k_B T / 2 c_0 z_i^2 e^2)^{1/2} \tag{6}$$

Where c_0 is the concentration of the $z{:}z$ electrolyte, ε_r is the relative dielectric permittivity of the solvent, ε_0 is the permittivity of vacuum, k_B is the Boltzmann constant, T is the temperature, z is the ion charge, and e is the elementary charge. The thickness of the EDL also depends on the applied potential, meaning the higher the potential difference, the smaller the Debye Huckel length.

The electrokinetic phenomena are associated with the double layer and are common to insulating solid/electrolyte interphase resulting in a relative motion between the insulating solid and electrolyte phases. For a deformable system like a tissue, the electrokinetic effect manifests as electroosmosis, streaming potential, electrophoresis and sedimentation potential [195]. The transport and extraction of biomolecules from a tissue by electroosmosis and electrophoresis is described in the sections that follow.

2.5.4.1 Electroosmotic Flow. Electroosmosis has numerous advantages and has been utilized in many microfluidic devices to transport solutes in biomedical devices [196]. Electroosmosis is the bulk fluid flow that is generated when an electric field is applied to a solid/electrolyte interphase [197]. When an electric field is applied to the interphase, a force density, $\boldsymbol{\rho_e E}$ is generated in the double layer, where E is the applied electric field strength. From the Stokes equation, the balance of electrical and viscous forces in the diffuse double layer reduces to:

$$\rho_e E + \mu \nabla^2 v = \nabla p \tag{7}$$

The resulting velocity of the bulk solution can be expressed in terms of the applied electric field, E_0 and the interfacial potential drop, ζ across the mobile portion of the double layer. The bulk electroosmotic fluid velocity can be written as:

$$U_{eo} = \frac{\epsilon\zeta}{\mu} E_0 \tag{8}$$

For a given double layer thickness, d and surface charge density, σ_d, the bulk velocity can be written as:

$$v = -\left(\frac{\sigma_d d}{\mu}\right) E_0 \tag{9}$$

2.5.4.2 Electrophoresis. Another of the double layer mediated electrokinetic transduction is electrophoresis. Electrophoresis refers to the movement of charged particles in electrolyte solutions induced by the application of electric fields. Electrophoresis as a method of DNA separation was introduced in 1962 by Matsubara and Tigarki, using starch as the medium [198]. Presently, gel electrophoresis is one of the prominent laboratory techniques for nucleic acid separation, quantification, and identification. Agarose gel provides the rigid matrix with good pore sizes required for the movement of the molecules and does not require a cross-linking agent [199]. The electrophoretic mobility, a measure of the relative difference in velocities of the charged molecules, depends on the properties of the gel, the electrolyte, the charge molecules and applied electric fields.

The intensity of the electrophoretic mobility is influenced by the geometry of the gel matrix. The pores within the gel matrix provide a pathway for the charged molecules to travel; hence, the velocity is affected by the pore size [200,201]. Equally, the molecular weight of the charged solute also affects the speed of migration. It is reported that molecules with smaller weight have higher mobility compared to heavier molecular weight molecules [202]. Both the direction and intensity of the electrophoretic velocity depends on the properties of the conducting media in contact with the electrodes. These properties include the ionic concentration, ionic strength, ionic species, and the pH of the electrolyte. The viscosity, density and the dielectric permittivity of the electrolyte also affect the velocity of the charged molecules [203]. The type of applied electric field, its magnitude and frequency also affect the direction and intensity of the electrophoretic mobility.

2.5.5 Joule Heating

Joule heating, also known as Ohmic or resistive heating, is a phenomenon in which energy is generated by an electric current passing though a conductor. Joule first demonstrated this principle in 1841, which subsequently became known as Joule's First Law:

$$P = I^2 \times R \tag{10}$$

Where: P is the power in watts, I is the current in amperes, and R is the resistance in ohms.

In biological tissues, it's crucial to consider the implications of Joule heating due to their sensitivity to temperature changes, particularly in the context of electrokinetic transport [204–206].

The application of an electric field to biological tissues leads to several electrokinetic effects, including electrophoresis, electroosmosis, and dielectrophoresis [207–209]. Joule heating occurs due to these electrokinetic processes, leading to a rise in the local tissue temperature.

Controlling Joule heating is critical, particularly for biomedical applications like drug delivery, tissue ablation, electroporation, and electrochemotherapy, where excessive Joule heating could cause unintended thermal damage [210].

There are various mathematical models to predict Joule heating in biological tissues. Ivorra and Rubinsky proposed a model for Joule heating during in vivo electroporation, where heat generated (Q) can be expressed as:

$$Q = \sigma . E^2 \tag{11}$$

Where: σ is the electrical conductivity in Siemens per meter and E is the electric field in volts per meter.

This model includes the impact of electric field-induced muscle contractions and electrode-tissue interface impedance on Joule heating. The authors demonstrated that these factors significantly contribute to the local temperature rise during in vivo electroporation.

In a further model by Sano et al., they incorporated the Pennes' bioheat transfer equation, describing heat transfer in living tissues, accounting for the metabolic heat generation, blood perfusion, and heat conduction [182,211]:

$$\rho c \left(\frac{\partial T}{\partial t}\right) = \nabla . (k \nabla T) + \omega_b \rho_b c_b (T_b - T) + Q \tag{12}$$

Where ρ is the tissue density (kg/m^3), c is the specific heat (J/kg·K), T is the tissue temperature (°C), t is the time (s), k is the thermal conductivity (W/m·K), ω_b is the blood perfusion rate (1/s), ρ_b is the blood density (kg/m^3), c_b is the specific heat of blood (J/kg·K), T_b is the blood temperature (°C), and Q is the heat source (W/m^3) including Joule heating.

One of the strategies to manage Joule heating in electrokinetic transport is the use of pulsed electric fields. PEFs apply brief, high-voltage pulses which can permeabilize cell membranes, a technique useful in electroporation, gene transfer, and other biomedical applications [212].

The key advantage of PEFs is that the short duration of the pulses allows for substantial modification of cellular structures with minimal heat generation, thus avoiding the harmful effects of Joule heating. This is particularly relevant in electroporation, where PEFs have demonstrated greater cell permeability with less thermal damage compared to continuous electric fields [213]. Moreover, PEFs provide better control over the spatial distribution of the electric field, allowing for targeted treatment and reducing potential harm to surrounding tissues.

Joule heating plays a significant role in electrokinetic transport across biological tissues. Its understanding and proper management are critical in various biomedical applications. Pulsed electric fields provide an effective means to manage Joule heating and have shown significant advantages over continuous fields. Further research is needed to optimize their use and to gain a better understanding of their effects.

2.6 Summary

The chapter discussed the anatomical structures of the spine, the function, and components of the IVD. The IVD is made up of three main components; the soft highly hydrated nucleus pulposus (NP), the fibrous concentric sheets forming the annulus fibrosus (AF), and the cartilaginous end plates (EP) which bounds the top and bottom of the disc. The IVD functions as a shock absorber by redistributing loads in the spine as a result of movement. As a load bearing tissue, the IVD is susceptible to loss of hydration and eventual tear. As an avascular tissue, the IVD is unable to heal itself hence the tissue degenerates and often requires an external intervention to repair. Pain medications are used at the onset of LBP, but surgical intervention is required to treat the condition at latter stages. Often, surgical interventions affect the integrity of adjacent IVDs and leads to re-herniation of the IVD. Some tissue engineering approaches have been explored to produce biomaterials for regenerating the disc. There have been successful hydrogel implants for NP replacements, however, the repair of the AF has proved elusive. Decellularization of the native tissue can be used to produce a scaffold that retains most of the biochemical and biomechanical components required to regenerate the AF tissue.

Current decellularization protocols involve using chemical detergents, enzymes or physical methods or a combination to remove immunogenic materials from the tissue matrix. However, these methods disrupt the matrix ultra structure and remove proteoglycans which are important for the matrix rehydration and eventual regeneration. Therefore, there is the need to develop a method to efficiently decellularize AF tissue without disrupting the ultra-structure and conserving the biomechanical and biomolecular components. In this context, the potential of PEF was discussed as a tool for enhanced tissue decellularization.

Pulsed electric fields have been extensively explored in recent years for several biomedical applications. PEFs have been used for cancer therapies in electrochemotherapy, DNA transfections and tumor ablations. When PEF is applied to a biological cell, nanopores are formed in the plasma membrane making it more permeable to molecules and ions. The dielectric nature of the biological tissue presents a complex challenge when apply pulsed electric fields. The complex impedance of the tissue directly influences the effectiveness of applying electric fields. Also, there is Joule heating associated with the application of electric current. Joule heating can escalate the temperature of the system and cause thermal damage hence there is the need to control it. The charge separation that occurs at the electrode-electrolyte interface when an external electric field is applied can also be explored for electrokinetic extraction of biomolecules across the tissue.

In the chapters that follow, the specific objective of the research is outlined as well as detailed description of experiments conducted to achieve the goals of this research.

Chapter 3

Objectives and Specific Aims

3.1 Global Hypothesis

The application of pulsed electric fields (PEFs) can be optimized to serve as a novel, rapid, and efficient method for the ex vivo decellularization of annulus fibrosus (AF) tissue, providing a structurally and biochemically intact scaffold for intervertebral disc (IVD) tissue engineering. This approach aims to address the critical challenges in spine surgery related to AF tissue repair, specifically the prevention of re-herniation and the facilitation of nucleus pulposus repair techniques. By characterizing the optimal parameters for non-thermal irreversible electroporation, we hypothesize that PEFs can selectively ablate AF cells while preserving the extracellular matrix, thus maintaining the scaffold's mechanical integrity and bioactivity crucial for subsequent recellularization. Furthermore, we posit that PEF-induced electrotransport can effectively remove nucleic materials without compromising essential proteoglycan content, enhancing the biocompatibility of the AF scaffold. Lastly, the development of a custom bioreactor for the application of PEFs is hypothesized to streamline the decellularization process, yielding a scaffold that is superior in terms of tissue compatibility and structural preservation compared to existing decellularization techniques. This comprehensive approach is expected to significantly advance the field of IVD tissue engineering, offering a viable solution for effective AF tissue repair and regeneration.

3.2 Aims and Objectives

Annulus fibrosus (AF) tissue repair techniques for the intervertebral disc (IVD) are of key relevance in spine surgery because; (1) they address the unresolved problem of re-herniation though the untreated annulus defect and (2) facilitate the development and repair techniques of the nucleus pulposus for IVD disease by providing adequate containment. Biological scaffold technology provides primary stability and 3-dimensional space for tissue formation by introducing a range of absorbable and non-absorbable biomaterials. Biological AF scaffold provides bioactive factors enforcing cell proliferation and matrix production as well as cell chemotaxis to enhance the AF repair process. The objective of this work is to develop a method for decellularizing the AF tissue which provides a 3D scaffold with structural integrity and retains biomolecular cues necessary for recellularization. The study explores using pulsed electric fields as a tool for ex vivo decellularization of native AF tissue.

PEFs have been shown in several studies to influence cellular activities such as proliferation, differentiation and migration [212,214–217]. Also, PEFs have been used to achieve tissue decellularization in vivo by using pulses to ablate cells in vivo and allowing the body's immune response to remove the debris of the dead cells [9,134,188]. A pulse duration of 10 ms and 20 ms period was applied. Millisecond pulse durations have been shown to migrate DNA across nanopores during electro transfection [218–220]. Current advancement in tissue electro clearing has led to the emergence of techniques such CLARITY and Stochastic electrotransport (SE) [221–225]. In the CLARITY protocol, conventional electrophoresis is employed by apply up to 10 kV/cm electric field across the tissue in the clearing solution for several days [221]. The aim of this study is to design a process that optimally utilize NTIRE as a tool to rapidly and efficiently produce decellularized AF tissue scaffold for the tissue engineering of the IVD.

3.2.1 Specific Aim 1 (Chapters 4 and 5)

The goal of this aim is to characterize the AF cells and AF tissue responses to pulsed electric field stimulations to determine the optimal parameters for non-thermal irreversible electroporation for tissue decellularization and reversible electroporation for other cellular processes. This is accomplished by isolating AF cells and exposing the cell cultures to different parameters of µsPEF in vitro and various assays and microscopy performed to determine cell responses to the applied PEF. For AF tissue studies, the tissue samples are exposed to µsPEF ex vivo and the impedance of the tissue is measured and compared to microscopy images to determine the extent of electro permeation.

3.2.2 Specific Aim 2 (Chapter 6)

The goal of this aim is to demonstrate that, electrotransport by way of applying pulsed electric fields can remove nucleic materials whiles conserving the proteoglycan content of the native tissue. To accomplish this, the electrophoretic mobilities of pyronin y and safranin o, two cationic dyes with properties similar to nucleic acids and glycosaminoglycans were measured across the tissue sample.

3.2.3 Specific Aim 3 (Chapter 7)

In this aim, a custom bioreactor is designed to provide a single unit for pulse treatment and enhanced removal of immunogenic materials from the tissue scaffold. The chamber is designed to achieve efficient and faster decellularization and incorporate electrodes to deliver pulses from high voltage power supply. Histological analysis is performed to characterize the scaffold decellularized with this protocol and compared to other decellularization protocols to determine the efficiency of the tissue decellularization method explored in this study.

Chapter 4

In Vitro and Ex Vivo Characterization of AF Cells and Tissue

4.1 Introduction

Cartilage tissue has limited repair capabilities during injuries. Cartilage heals poorly or do not heal at all leading to tissue degradation[226]. The cells in the cartilage become senescent, releasing chemicals that cause inflammation [226,227]. Cell therapy holds great potential in addressing cartilage degradation, however, several challenges remain for clinical translation. Appropriate maintenance of cell state, expanding cells reproducibly in large quantity for transplantation, assuring efficient differentiation into desired cell types and maintaining cell viability and migration during and after delivery are some of the challenges with cell therapies [228–232]. Cellular responses such as proliferation and differentiation can be induced and controlled by physical methods such as mechanical and electrical stimulations, and chemical methods such as substrate and material design [233]. Electric fields have been used to induce cellular phenomena by modifying the membrane potential, which impacts the voltage-gated channels which impact the influx of ions [234]. The treatment time of electric field stimulation can be shortened to ultra-short pulse electric fields (PEF) at higher voltages without damaging the cell [235,236].

The several different cellular responses to PEF have the potential to be utilized in tissue engineering and regenerative medicine. The parameters of PEFs can be chosen such that temporary or permanent pores are created in the cell membrane [237]. It has been observed that different cell lines respond differently to PEF. Therefore, optimization of pulse parameters for electropermeabilization must be cell or cell line specific [237,238]. The effect of PEF is multifactorial and is also influenced by the dielectric nature of the plasma membrane. The effects of PEF-exposures depends on the applied field intensity, pulse duration or width, the number of pulses and the repetition rate [233,239]. The optimal pulse parameters also depend on the electrosensitivity of the cells within a threshold PEF exposure proximity, which includes properties such as the cell radius and the type of tissue [216,237,238]. Cytotoxic effects of PEF have been extensively studied with several cell lines. However, there is no consensus if any single exposure metric could reliably and universally predict cell death due to PEF exposure [235,240,241]. For instance, Ibey *et al*. measured the absorbed dose-dependent survival of Jurkat and U937 cell lines with trains of electric pulses, and Pakhomov *et al*. measured the survival of U937 with absorbed dose and number of pulses. Also, Cemazar *et al.* studied the electrosensitivity and electropermeability of twelve different cell lines with electric field intensity of applied PEF. However, the response of annulus fibrosus (AF) cells to PEF exposure has not been studied. Although the AF tissue environment is different from the AF cells in media, *in vitro* studies of cellular responses induced by PEF-exposures of AF cell can serve as a guide for in vivo applications such as tissue regeneration and decellularization.

PEF parameters can be chosen such that not only cell death can be achieved, but other cellular activities can be enhanced. There have been studies conducted on the effects of electric fields on proliferation of different cells and cell lines [212,234,242,243]. Electric fields have also been observed to affect the migration of cells [28,244–246], differentiation [247,248] and increase of growth factor and DNA syntheses [249]. Cell proliferation and migration play significant roles in tissue regeneration. Slow proliferation significantly impedes the regeneration of tissue [234]. For this reason, PEF-induced AFC proliferation has the potential of enhancing the regeneration of the AF tissue. Similarly, cell migration is vital to mammalian cell embryonic growth [250]; hence, systematic PEF-induced AFC migration can be important to AF tissue regeneration. In this study, we characterize the effects of microsecond-duration PEF (µsPEF) on AF cells *in vitro*, to determine the lethal dose parameters and relevant combination of electric field parameters to enhance cell proliferation and migration. Our findings demonstrate that PEF can be applied to decellularize the AF tissue to create a native tissue scaffold and also has the potential application of enhancing proliferation and migration of transplanted AF cells in the AF tissue matrix.

4.2 Materials and Methods

4.2.1 Fibroblast Cell Isolation and Culture Conditions

Whole bovine tails were acquired from a local abattoir (Bringhurst Meats, Berlin, NJ, USA) without the skin to reduce contamination. Intact IVDs are dissected using #10 and #22 scalpels within 4 h of sacrifice while being kept hydrated in saline. Under aseptic conditions, the Annulus Fibrosus (AF) tissue were isolated with biopsy punch (6 mm diameter) and transferred into a specimen container. The isolated fibrocartilage tissue is minced and incubated overnight in collagenase P solution, made by dissolving 50 µg of collagenase enzyme (Rockland Immunochemicals, Philadelphia, PA, USA) in 10 mL growth media. The growth media consist of Dulbecco’s modified Eagle Medium (DMEM) supplemented with 10 % fetal bovine serum and 1 % antibiotic antimycotic (Thermo Fisher Scientific, Bridgewater, NJ, USA). After digestion, the suspension is sieved though a 100 µm cell strainer, centrifuged at 1200 rpm for 5 min, and the pellet re-suspended in fresh growth media. The cells were counted and seeded in monolayer cell culture flasks at a concentration of 2×10^5 cells/mL then incubated at 95 % humidity, 5 % CO_2 and 37 ^{0}C. At 90 % confluency, the cells are trypsinized and re-suspended in media for PEF exposures.

4.2.2 µspef Exposures

The PEF exposure system used to execute the pulses was a commercially available pulsing system consisting of a pulse generator (BTX Gemini X2), a cuvette holder, standard 1 mm and 2 mm gap electroporation cuvettes, and the gold-plated Petri Dish Pulser electrode array (BTX, Holliston, MA, USA). The cuvettes were used to expose cell suspensions for PI uptake and viability studies, whereas the petri dish electrode was used to expose adhered cells for migration studies. The responses of primary AF cells to µsPEF were explored by exposing the cells to 10- and 100-µs pulse durations at different electric field strengths and pulse numbers. Rectangular pulse waveforms with 1, 5, 10 and 20 pulses at 1, 1.5 and 2 kV/cm were applied to the cells. Our COMSOL Multiphysics simulation of the applied fields was published[251]. The sham controls for all the exposures were handled similarly except pulses were not applied to the cells.

4.2.3 PI Uptake and Viability

Propidium iodide (PI) fluorescent dye was used to detect the integrity and electropermeabilization of the plasma membrane of living AF cells. Cells suspended in growth media was mixed with PI solution (2 µg/ml). The cell suspension was then put in 1-mm gap cuvettes, followed by pulse exposures. The exposed cells were seeded on glass-bottom dish immediately after exposure and incubated for 15 min after which they were imaged. Parallel controls were run with unexposed cells (sham) and cells treated with digitonin. Permeabilizing medium was prepared by diluting the digitonin to give a final concentration of 30 μM within Ca^{2+}-free media. The cells were incubated in 0.25 mL of 30 μM digitonin-permeabilizing medium for 10 min. Imaging was performed using a Thorlabs Confocal Microscopy Upgrade (Newton, NJ, USA) attached to an Olympus IX-73 microscope (Tokyo, Japan).

For cell viability measurements using the MTT assay, cells were exposed at 1.2×10^6 cells/mL in 2-mm gap electroporation cuvettes. Exposed cells were aliquoted into 96-well plates in triplicates at 2×10^4 cells/well. The volume of the cell suspension was topped to 100 μL/well growth media and incubated at 37 ^oC and 5 % CO_2 for 24 h or 72 h. After appropriate time of incubation, 10 μL of MTT reagent, 3-(4,5-Dimethylthiazol-2-yl)-2,5-diphenyltetrazolium bromide, was added to each well and further incubated for 4 h. The crystal dissolution solution was then used to dissolve the blue formazan crystals formed during incubation by adding 100 μL of the solvent to each well and shaking overnight on an orbital shaker. The absorbance was read at 570 nm using a Tecan Infinite F200pro microplate reader (Morrisville, NC, USA). The optical absorbance of the exposed cells was converted to cell density and normalized against the matched controls (unexposed cells).

4.2.4 Migration Studies

At 90 % confluency, the AF cells were trypsinized and seeded with growth media in a 60 mm^2 petri dish. The cells were then incubated in a humidified incubator at 37 ^0C and 5 % CO_2 until reaching 85 to 90 % confluency. The media was aspirated, and the cells were washed with 2 mL phosphate buffered saline (PBS). A wound model was formed in the center of the plate by scratching a cell-free area (~150 µm gap) into the confluent monolayer. The cells were rinsed twice with 1 mL PBS to remove all debris. Complete growth media was added to the cells, and images were taken using an Olympus CKX53 inverted phase microscope using a 10X, 0.25 NA objective (Tokyo, Japan). The cells were then exposed to µsPEF using a Petri Dish Pulser electrode array. The electrodes were placed 1 mm above the cell monolayer during pulse exposures. Images were taken at 3 h intervals for a total of 24 h duration for migration distance analysis.

4.3 Results

The experimental design investigates the electroporation effect of µsPEF exposure of primary AF cells isolated from bovine AF tissue. The extent of electroporation of various combinations of the applied field strength and number of pulses of 10 and 100 µs PEF was measured by the uptake of PI after pulse exposures. The viability of the cells at 24 and 72 h after exposure to these µsPEF parameters have been determined using the MTT cell viability assay. The effect of µsPEF exposure on cell migration has been measured for adherent AF cells in culture using a scratch wound healing method.

4.3.1 Membrane Permeabilization by Microseconds Pulsed Electric Fields

AF cells exposed to µsPEF uptake propidium ions, indicating the loss of functional integrity of the plasma membranes (Fig. 1). For both 10 and 100 µs pulse widths, more cells are permeabilized with increasing number of pulses. The 20-pulse exposures show the most cells with damaged plasma membrane for 1, 1.5 and 2 kV/cm field strengths, as compared to 1, 5 and 10 pulse exposures. There is no significant difference between 10 and 100 µs pulse width for PI uptake.

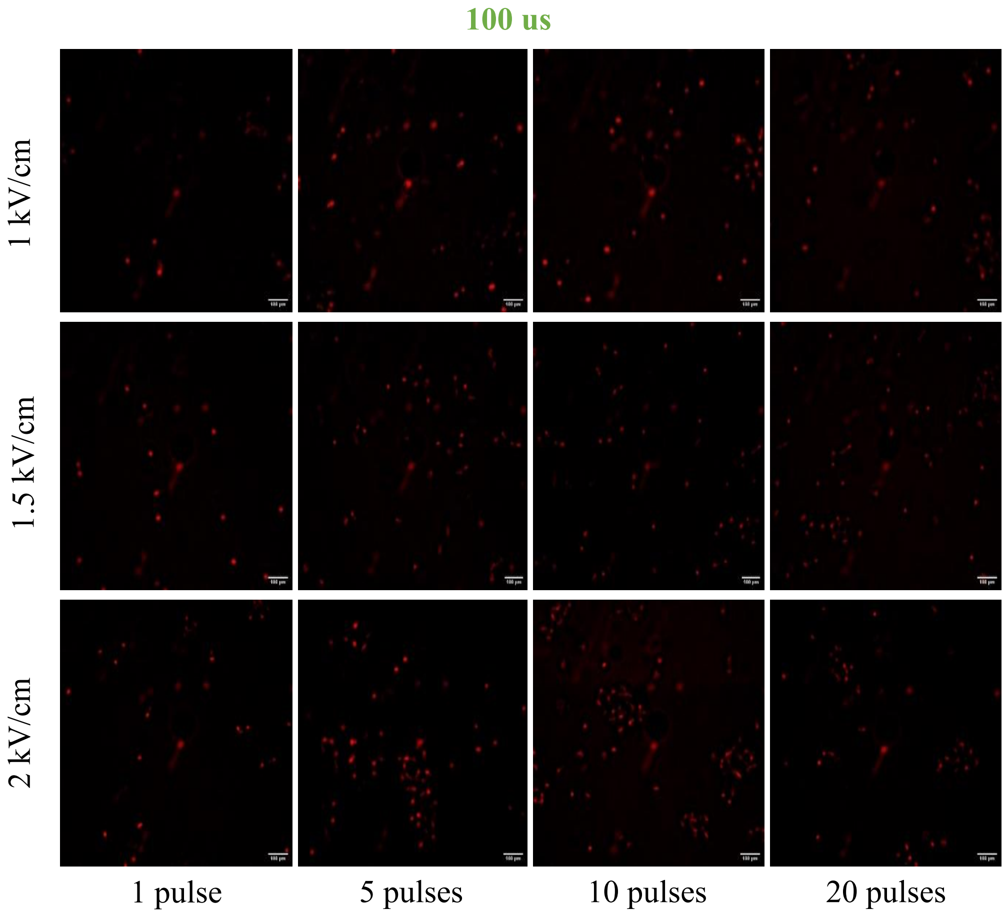

Figure 16. Florescent Confocal Images of PI Uptake after Exposures to 100 µsPEF

.

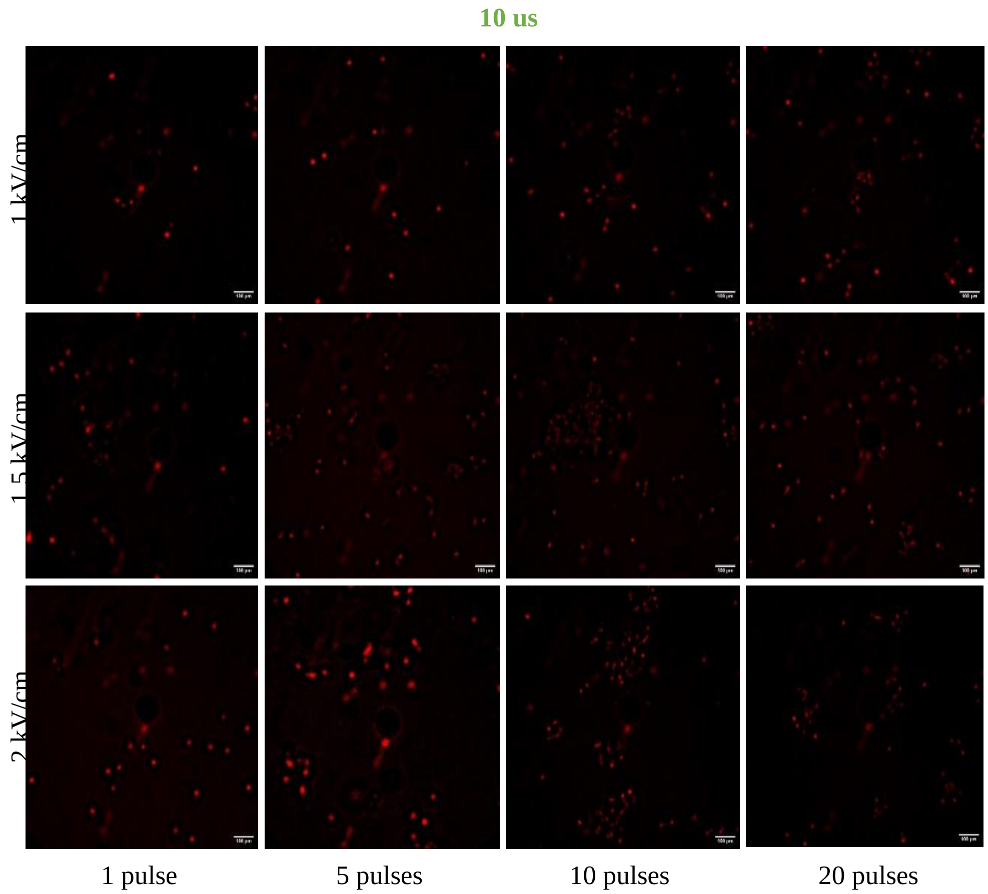

Figure 17. Florescent Confocal Images of PI Uptake after Exposures to 10 µspef. Images were taken within 5 min after exposures to 1, 5, 10 and 20 pulses of 100 µs pulse width at 1 kV/cm (Top), 1.5 kV/cm (Middle) and 2 kV/cm (Bottom)

4.3.2 Viability 24 and 72 h Post-Exposure

The correlation of increased PI uptake to decreased viability is shown in Figures 2 and 3. The viability is reported as a percentage of the sham controls. After 24 h, the viability of PEF-exposed cells decreases (Fig. 2A) for cells exposed to the 100 µs pulse width and all pulse parameters. Increasing the number of pulses generally decreases cell viability after 24 h for 100 µs pulse width. However, no linear relationship is observed with the applied electric field strength. At lower number of pulses (1 and 5), there is no statistical difference between the electric field strength effects, whereas the impact of field strength becomes more significant with higher number of pulses (10 and 20). The 24-h viability measurements (Fig. 2A) reveal necrotic cell death, while the 72-h viability measurements (Fig. 2B) can show apoptotic cell death. For 100 µs PEF, AF cells experience necrosis earlier after exposure and apoptosis later given a lower number of pulses, as viability decreased further between 24 and 72 h after exposure to 1 or 5 pulses (Fig 2B).

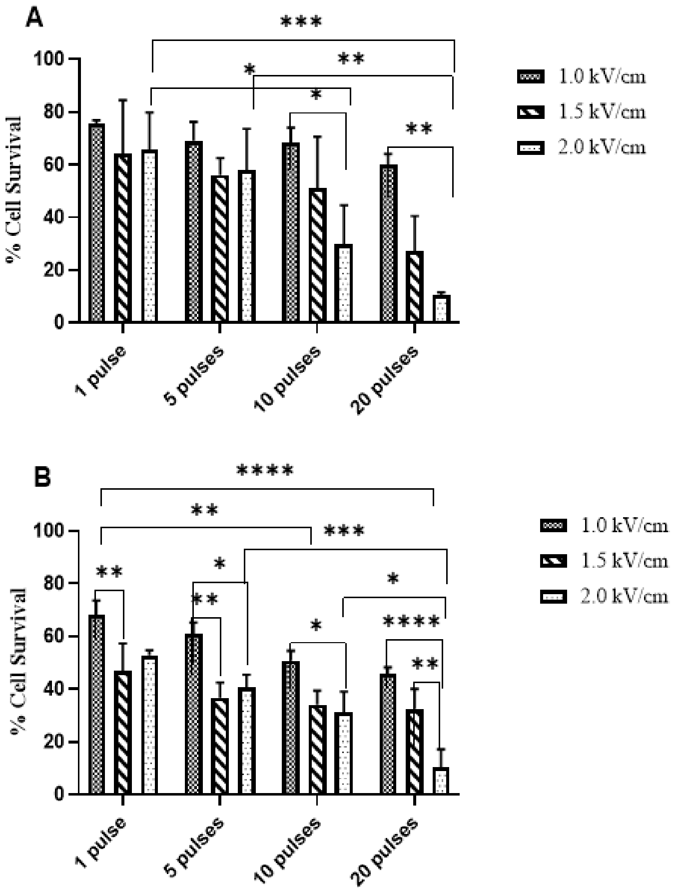

Figure 18. Cell Viability after Exposure to 100 µsPEF with Varying Number of Pulses and Electric Field Intensity. (A) AF cell viability after 24-h post 100 µsPEF exposures. (B)AF cell viability 72-h post 100 µsPEF-exposures. (n=5 independent experiments) Data are mean and SD. Statistical significance represented: p<0.0001, for comparison, number of * represented the decimal places of the p value

Figure 19 shows the viability of primary fibroblast cells 24 and 72 h. after PEF-exposure to 10 µs pulse width. Cell viability decreases 24 h. post-exposure (Fig. 17A) showing the fraction of cell death due to the necrotic effects of the applied pulses. The lethal effect of the applied pulses is dependent on the number of pulses. However, Fig. 4B shows increased cell viability 72-h post 10 µs pulse width PEF-exposure. Relative to the sham, the fibroblast cells show enhanced proliferation after being treated with 10 µs pulse width. The cell proliferation increases with 1 and 5 pulses at 1.0, 1.5, and 2.0 kV/cm electric fields.

However, at 10 and 20 pulses, the cell proliferation is not as significant at all applied electric fields even though when compared to cells treated with 100 µs pulse width (Fig. 16B), the 10 µs pulse width treated cells at higher number of pulses show a significant rate of survival after 72-h post exposure (Fig. 17B).

The statistical analysis shows that, the observed effect of both the 10 and 100 µs pulse widths are influenced by the number of pulses. The ratio of the significant difference of the number of pulses for the PEF exposure with 10 µs pulse width to 100 µs pulse width is greater than 200. This shows the extreme dependance of the observed effect of the 100 µs pulse width on the number of pulses compared to that of the 10 µs pulse width. On the other hand, the applied electric field only influences the cell responses observed in the 100 µs pulse width PEF-exposures with p-value < 0.0001. Though the effect of the applied electric field was not significant for the 24-h post PEF-exposure analysis of the 10 µs pulse width treated cells, the 72-h post PEF-exposure shows a significant dependence on the applied electric field with a p-value = 0.025. Therefore, the necrotic effects observed in the cells after µsPEF-exposures can be mainly attributed to the number of pulses, whiles the proliferation and apoptotic responses can be attributed to a combination of the number of pulses and applied electric field.

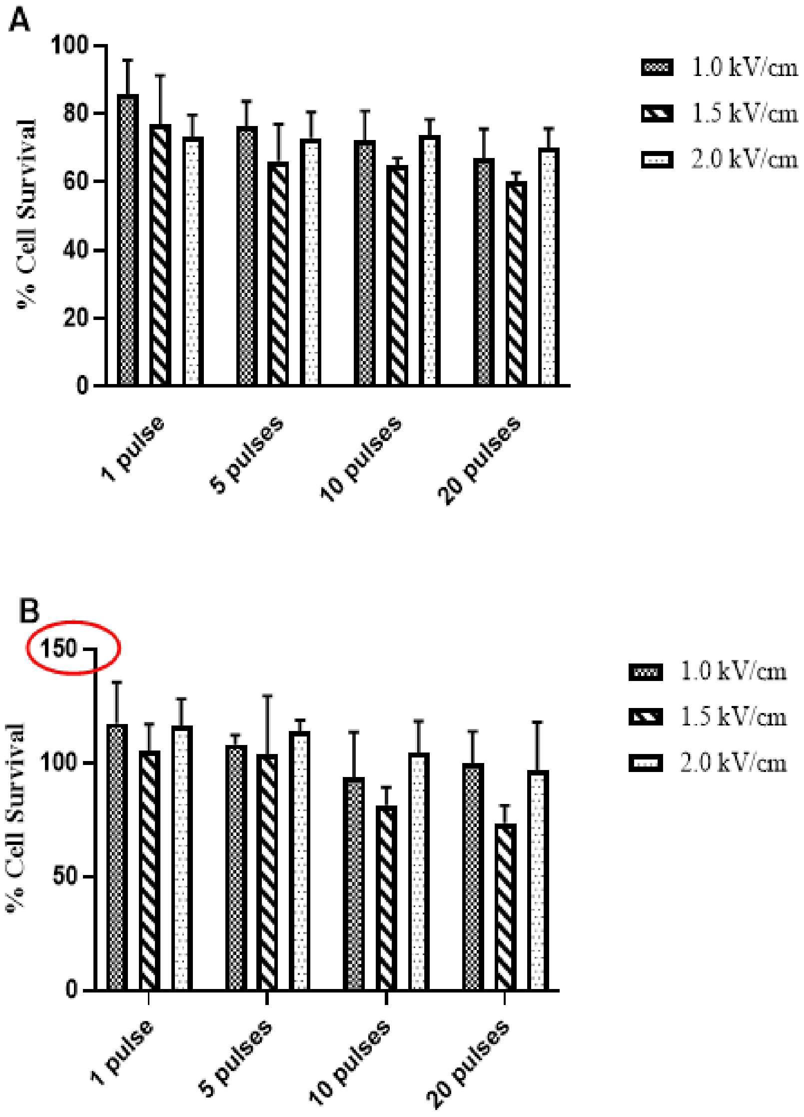

Figure 19. Mean and SD of AF Cell Viability after Exposures to 10 µspef. (A) AF cells viability after 24-h post 10 µsPEF-exposures. (B) AF cell viability 72-h post 100 µsPEF-exposures (cell viability exceeds 100% of the control hence the y-axis goes up to 150%). (n=5 independent experiments) Data are mean and SD. Statistical significance represented: $p<0.001$

4.3.3 Effect of PEF-Exposures on Migration

To study the effects of µsPEF-exposure on cell migration, a manual wound of ~400 µm was formed on the AF cell monolayer and subjected to trains of electric pulses. The cells were placed under an inverted microscope for imaging every 3 h. Figures 20 and 21 show compares the wound model before µsPEF-exposure and after 24-h post µsPEF-exposures to 10 and 100 µsPEF. The average wound width was measured and used to determine the average rate of migration of the cells after µsPEF-exposure.

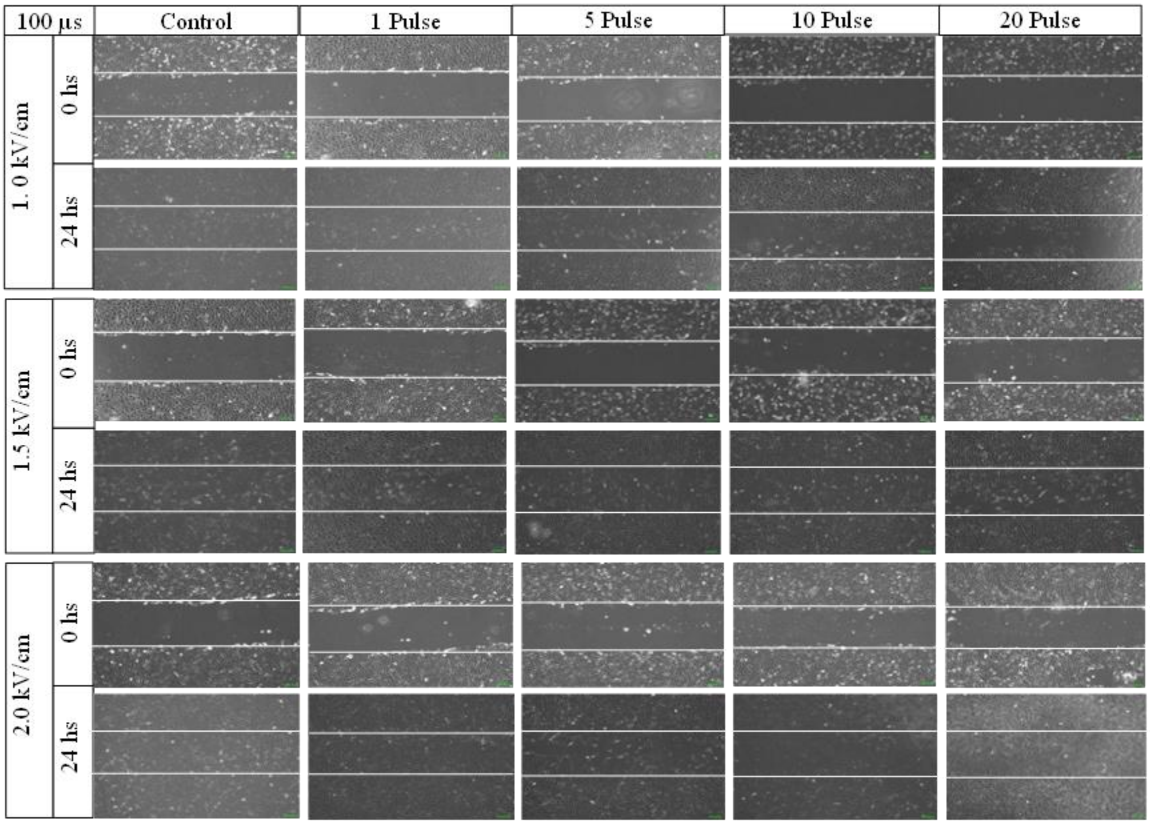

Figure 20. Representative Images of AF Cell Migration at 0-H And 24-H Post 100 µspef-Exposure

The average rate of migration with respect to time is plotted for cells exposed to 1, 5, 10 and 20 pulses at 1.0, 1.5, and 2.0 kV/cm for both 10 µsPEF and 100 µsPEF in Fig. 7. We found out that the average rate of migration of the unexposed fibroblast cells exceeds the rate of migration of the exposed cells. However, the rate of migration was enhanced in cells exposed to 1 pulse at 1.0 kV/cm of 10 µsPEF. The rate of migration is generally affected by the number of pulses as well as the applied electric field for both pulse widths. For 10 and 100 µsPEF-exposures, the average rate of migration decreases with increasing number of pulses. The relation between rate of migration and number of pulses is emphasized by an average p-value <0.001 for both 10 and 100 µsPEF-exposure (Fig. 21). The 10 µs pulse width exposures showed higher rate of cell migration post PEF-exposures compared to the cells treated with 100 µs pulse width. This observation is corroborated in the reduced cell viability reported in the viability studies. The significant cleaving of the adhered cells after exposures to 10 and 20 pulses of the 100 µs pulse width is also noteworthy, as it suggests that µsPEF-exposure could have significant effects on cell adhesion and morphology.

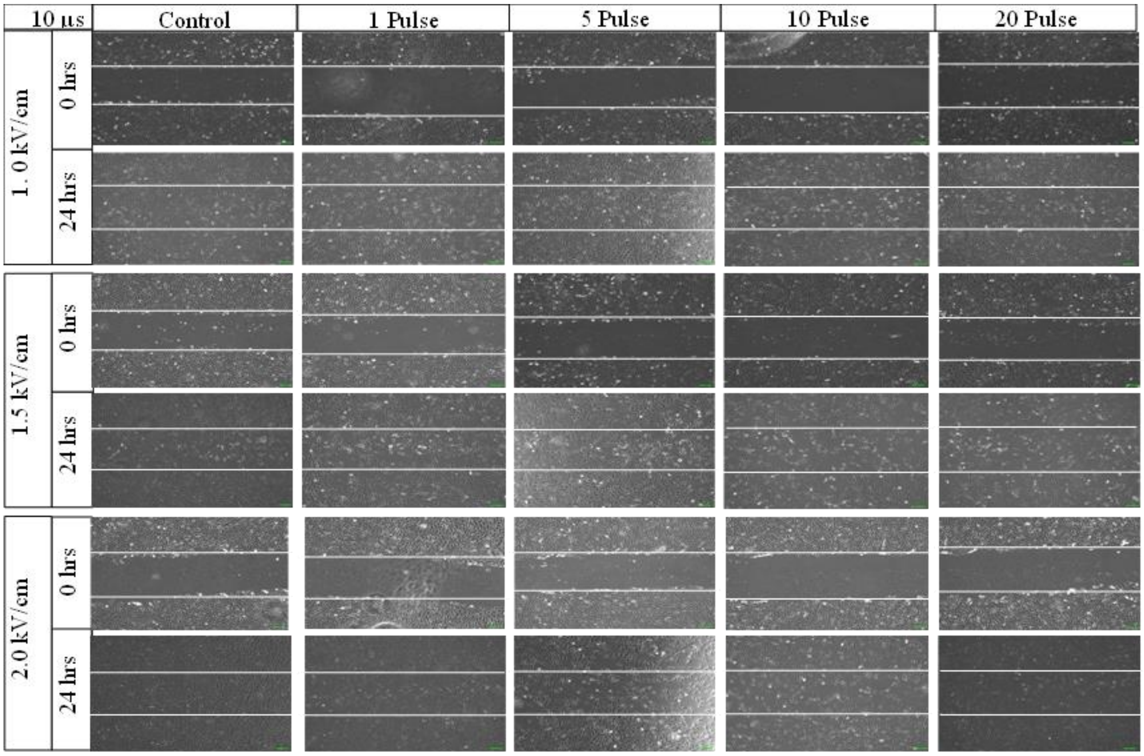

Figure 21. Representative Images of AF Cell Migration at 0-H And 24-H Post 10 µspef-Exposure

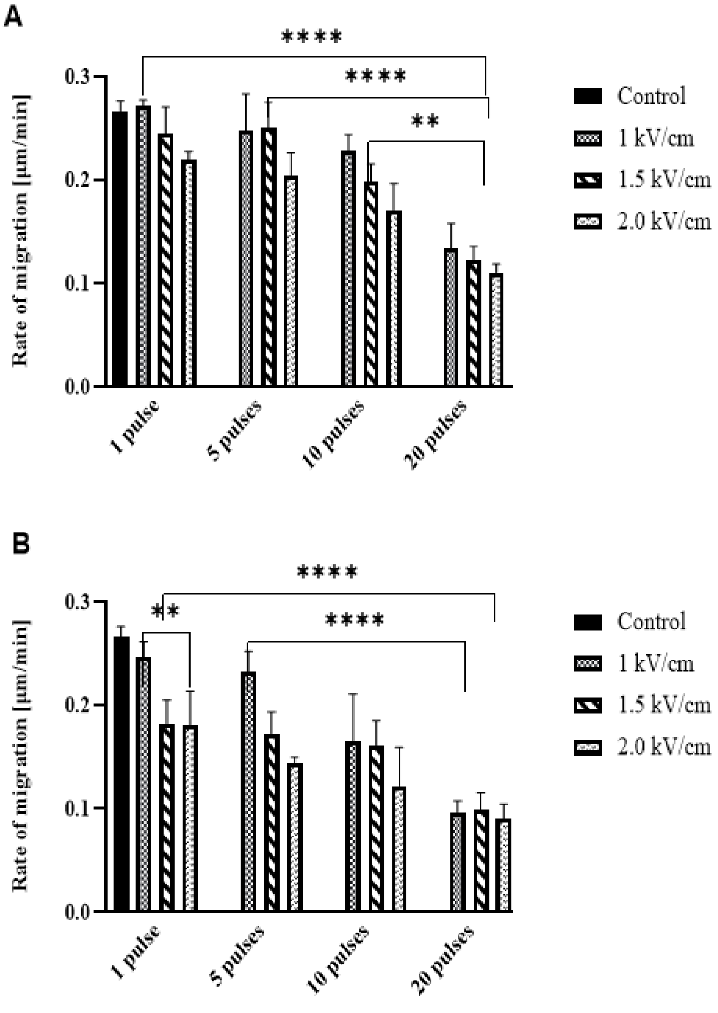

Figure 22. Rate of AF Cell Migration Post µsPEF-Exposure with Different PEF Parameters. (A) Rate of migration of AF cells exposed to 10 µsPEF in 24-h. (B) Rate of migration of AF cells exposed to 10 µsPEF in 24-h. Results are presented as mean ±SD; **p<0.01, ***p<0.001, ****p<0.0001

4.4 Discussions

Short intense electric pulses induce important changes in cell physiology by permeabilizing the cell membrane [252]. µsPEF are effectively used in several research arrears such as medicine and biotechnology, for antitumor electrochemotherapy, tumor ablation, cell transfection, etc. the duration of µsPEF is long enough to cause transmembrane potential changes. µsPEF solely interact with the plasma membrane and change its permeability properties if the field amplitude reaches a certain threshold. The electrical parameters selected for the µsPEF stimulation caused fibroblast electropermeabilization, which was verified by the uptake of PI dyes.

The experimental results as presented in the section above demonstrates that the parameters of PEF such as number of pulses, applied field intensity, and pulse width can individually influence the lethal and stimulating effects of the PEF on primary bovine AF fibroblast cells. The results suggest that the effects of PEF-exposure on fibroblast cells are complex and depend on several factors, such as pulse width, number of pulses, and applied electric field. The 10 µs pulse width treatment caused necrotic effects in cells, but there was increased cell viability and proliferation at 72 h. post-exposure. The effect of the number of pulses was more significant in the 100 µs pulse width treatment, and the applied electric field had a significant impact on cell responses observed in the 100 µs pulse width PEF-exposures. Therefore, 10 µs pulse width induces reversible electroporation whiles the 100 µs pulse width induces irreversible electroporation in the primary bovine AF fibroblast cells. Sankara Narayanan et al. reported irreversible electroporation in Chick Embryo Fibroblast with 1 and 8 pulses at 1.2 kV/cm with 100 µsPEF [28]. Hanna et al. also reported reduced cell viability in DC-3F cell line after exposure to 1 pulse of 100 µsPEF at 1.4 kV/cm to 2.0 kV/cm even though hMSCs mortality was not reduced after exposure to up to single 100 µsPEF at 2.0 kV/cm [29]. The application of PEF has been reported to enhance proliferation in other cell types [8], [9], [17]– [19].

Based on the analysis of the rate at which the wound gap closed, the AF fibroblast cells exposed to a single pulse 10 µsPEF at 1.0 kV/cm showed an increase in migration speed compared to the to the unexposed control group. Fibroblast cells exposed to up to 20 pulses at up to 2.0 kV/cm of 10 µsPEF stimulation expressed statistically remarkable decrease in migration speed compared to the control. On the other hand, fibroblast cells exposed to 100 µsPEF stimulations significantly reduced the rate of cell migration compared to the control and the group exposed to 10 µsPEF stimulation. Therefore, µsPEF can change the morphology of the cell hence influencing the cell migration behavior by increasing or decreasing cell migration depending on the selected PEF parameters. Xiang et al. reported increased fibroblast cell migration speed with a single 100 µsPEF at 0.75 kV/cm stimulation whiles cells exposed to 1.5 kV/cm stimulation expressed a remarkable decrease in migration speed [30]. When the parameters of the pulse are select such that, a higher cell viability is maintained, µsPEF stimulation could promote an increasement in the migration speed of primary fibroblast cells over a long period which has the potential to significantly reduce clinical treatment time.

These findings suggest that the effects of PEF-exposure on cells are multifactorial, and the duration, intensity, and number of pulses should be considered in future studies. Overall, this study provides valuable insights into the complex cellular responses to µsPEF -exposure and paves the way for further research in this field.

4.5 Conclusion

In conclusion, the use of µsPEF in various research areas such as medicine and biotechnology has been demonstrated to induce significant changes in cell physiology by permeabilizing the cell membrane. The effects of PEF-exposure on fibroblast cells are complex and depend on several factors, such as pulse width, number of pulses, and applied electric field. The study presented here highlights that the duration, intensity, and number of pulses should be considered in future studies, as these factors can have significant impacts on the effects of µsPEF on cells. Overall, these findings provide valuable insights into the multifactorial cellular responses to µsPEF-exposure, paving the way for further research in this field.

Chapter 5

Ex Vivo Characterization of the Native AF Tissue

5.1 Introduction

The diversity of cellular responses to pulsed electric field (PEF) exposure motivates its use in tissue engineering and regenerative medicine [188,190,234]. PEF-based technologies have been applied extensively in cancer therapies and for non-viral transfection of cells [236,253–255]. Application of PEF creates nanoscale defects in the cell membrane that allow for movement of ions and molecules into and out of the cell. This phenomenon is known as electroporation or electropermeabilization of the plasma membrane. PEF parameters can be tuned to create temporary or long-lived permeabilization of cell membranes [235]. Due to the dielectric nature of the plasma membrane, the effect of applied external PEF depends largely on the pulse duration, number of pulses, rate of repetition, and exposure field strength [9,236].

Biological tissue consists of cells embedded in an extracellular matrix (ECM). The intracellular and extracellular fluids exhibit low resistive electrical properties under the application of an alternating current (AC) electric field, whereas the phospholipid bilayer membrane produces a capacitive impedance to AC fields [256,257]. Thus, biological tissue produces a complex electrical impedance known as bioimpedance. The complex bioimpedance develops from charge accumulation at membrane/electrolyte interfaces, causing field distortions, conductivity changes and diffusive flux around the cells [258]. The complexity of a tissue's bioimpedance depends on its physiology and physiochemical status and on the frequency of the applied signal. Generally, biological tissues have high impedance at lower frequencies. Probing tissues over a range of frequencies provides important information on tissue physiology.

Bioimpedance of tissues can be measured by a method known as electrochemical impedance spectroscopy (EIS) also known as electrical impedance spectroscopy [259,260]. The EIS technique involves analyzing the frequency response of the impedance distribution of the tissue by injecting a certain frequency range of exciting current (voltage) into the tissue, measuring the voltage (current), and analyzing and processing the collected signals. Tissue electrical properties such as the relative conductivity and equivalent permittivity can be derived from the measured impedance using a probe constant. Bioimpedance and electrical conductivity are intrinsic properties related to fluid volume, ion concentration, and membrane permeability. Tissue bioimpedance changes upon PEF-induced electropermeabilization of cell membranes [261–263]. Therefore, EIS can be used to quantify electropermeabilization within tissues.

Electropermeabilization often is measured by microscopic imaging of a membrane-impermeable fluorophore that penetrates the cells following PEF exposures [264]. Yet, dye influx can take up to 30 min and often does not allow measurements in real time. Furthermore, optical microscopy only detects clear signals near the surface of most tissues and cannot reveal the total extent of electropermeabilization in the entire tissue volume. EIS measurement on the other hand can be used to detect electropermeabilization in real time and throughout the entire tissue. There has been extensive development of diagnostic tools based on EIS measurements, especially of pathologic tissue types [184,213,265,266], and EIS boasts some successful clinical applications [267–270]. However, EIS has not been extensively explored as a tool to measure the degree of PEF-induced electropermeabilization of mammalian tissues, especially cartilage.

Herein, biophysical properties of bovine annulus fibrosus cartilage tissue exposed to µsPEF with varied pulse parameters are characterized. The goal is to use EIS as a tool to measure cell permeability and death in avascular cartilage tissue following PEF exposure. PEF of 100 µs duration have been used to induce irreversible electroporation within other types of tissues, such as arteries [190]. Relative tissue electrical conductivities and permittivity of the tissue are calculated using a probe calibrated with NaCl solutions of known concentrations ranging from 0.0015 M to 0.15 M [213]. Impedance spectra, effective electrical conductivities and permittivity of the cartilage tissue change with PEF exposure. These changes in dielectric properties correlate with trends seen from Live/Dead confocal fluorescence microscopy assay of cells near the surface of the cartilage samples.

5.2 Materials and Methods

5.2.1 Impedance Spectroscopy

EIS measurements were conducted using a Gamry Instruments Interface 1010E™ potentiostat (Warminster, PA, USA). By running a galvanostatic EIS experiment, the device measured the impedance of a conductor injecting AC current at 3 µA over a frequency range of 100 H_z to 1 MH_z Stainless steel caliper electrodes (BTX®, Holliston, MA, USA) formed a parallel plate, two-electrode system for both EIS measurements and PEF exposures. In EIS, the two-electrode setup measures the complete voltage drop for the current across the whole sample. The working and working-sense electrodes are attached to the anode, while the reference and counter electrodes are connected to the cathode. Filter paper pads soaked in 50X Tris-acetate-EDTA (TAE), a conducting solution were affixed to the caliper electrodes to protect the stainless-steel surfaces (Fig. 1).

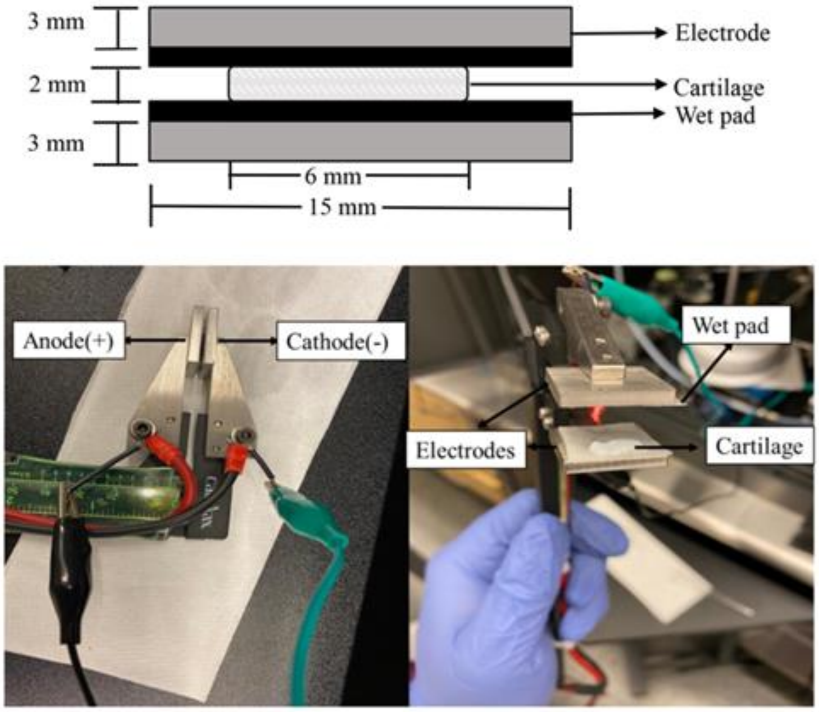

Figure 23. Diagram and Experimental Set-Up for Electrochemical Impedance Analysis. The pulse generator is connected to the electrodes via ring terminals, and the potentiostat is connected via alligator clips. (The potentiostat is disconnected during pulse application.) Each square electrode surface is 225 mm^2. The cartilage sample is compressed by hand between solution-soaked filter paper pads. The caliper electrodes allow for determination of the electrode gap distance

The probe calibration method was described in detail elsewhere [271–274]. Calibration enabled acquisition of values of equivalent conductivity ($\varepsilon_{e,eq}$). and equivalent relative permittivity (σ_{eq}) The probe was calibrated by comparison to known conductivity values using 0.001 M to 0.15M NaCl (Fig 24.). The probe calibration liquid was retained between the electrodes by surface tension within the filter papers. The gap between the electrodes was maintained at 2 mm thoughout the calibration since the thickness of the tissue samples were sectioned at 2 mm. However, the lateral spread of the liquid could not be controlled. The probe constant (K) was determined using the real part of the impedance spectra. Tissue conductance (G) and capacitance (C) were found by the expression for the inverse of impedance (Z), which is admittance (Y):

$$Z^{-1} = Y = G + jwC \tag{13}$$

with j being the imaginary number, √(-1), and w being the angular frequency. Equivalent tissue properties are determined using K in the expressions:

$$G = K\sigma_{eq} \tag{14}$$

$$C = K\varepsilon_0\varepsilon_{e,eq} \tag{15}$$

with $\varepsilon_0$being the permittivity of free space. The impedance and electrical conductivity of excised tissue samples both before (control) and after PEF exposed were measured to determine the extent cell permeabilization with respect to varying parameters of the applied electric pulses.

Table 6

Evaluation of K Using Average Conductance, G (S), of Different NaCl Concentrations (M) from 100 H_z to 1 MHz

NaCl (M)	G_{avg} (S)	± S.D.	% S.D.
0.0015	2.99E-03	8.78E-05	2.93
0.005	9.88E-03	1.60E-04	1.62
0.01	1.63E-02	2.85E-04	1.75
0.03	5.61E-02	2.26E-03	4.04
0.05	9.75E-02	4.82E-03	4.94
0.1	1.78E-01	1.14E-02	6.41
0.15	2.26E-01	1.66E-02	7.35

5.2.2 Tissue Harvesting and Preparation

Whole bovine tails were acquired freshly harvested from a local abattoir (Bringhurst Meats, Berlin, NJ, USA) without the skin to reduce contamination. Intact intervertebral discs (IVDs) were dissected using #10 and #22 scalpels and a band saw within 4 h of sacrifice under sterile conditions and kept hydrated in saline solution. The fresh AF tissue was isolated and sectioned with 6 mm biopsy punches along the circumference of the disc, perpendicular to annular fiber orientation. AF tissue was exposed and measured immediately after preparation.

5.2.3 PEF Exposures

A BTX® Gemini X2 electroporation system (Holliston, MA, USA) with stainless steel caliper electrodes was used to expose AF tissue at room temperature. Tissue samples of 6 mm diameter and 2 mm thickness were sandwiched between filter paper soaked in 50X TAE buffer solution. Calipers were closed gently until the sandwiched sample completely contacted the pad and electrode surfaces. The final distance between the steel electrodes was 2.5 mm for pulse exposures and EIS measurements. PEF of 100 µs duration (tp) were applied at 1 Hz repetition rate. The effect of electric field strength (E) was tested from 0.1 kV/cm to 5 kV/cm. Secondly, the number of pulses (n) at 2 kV/cm and 4 kV/cm was varied at 10, 20, 50, 80, or 100 pulses. Thee independent experiments were run for each set of pulse parameters. In each of the experiments, pulse parameters were alternated in a random sequence. For a given mass of tissue (m), the total specific energy delivered (SED) was calculated as:

$$SED = \frac{\sigma_{eq} E^2 t_p n}{m} \tag{16}$$

Are there definitions for this equation?

5.2.4 Fluorescence Microscopy

Cell permeabilization and viability in the AF tissue was measured using a Live/Dead Assay (Biotium Kit # 30002, Fremont, CA, USA), which included ethidium homodimer III (EthD-III) as the “dead” dye and Calcein AM as the “live” dye. The manufacturer’s protocol was followed for the Live/Dead assay. Briefly, 5 µL of 4 mM Calcein AM and 20 mL of 2 mM EthD-III was added to 10 mL PBS. Tissue samples exposed to pulses as described above were incubated in aliquots of the dye solution at 37

^{o}C for 15 min followed by imaging. Imaging was performed using a Thorlabs Confocal Microscopy Upgrade (Newton, NJ, USA) attached to an Olympus IX-73 microscope (Tokyo, Japan). Image processing and analysis was performed using Fiji/ImageJ [275] What type of processing did you perform?.

5.2.5 Statistical Analysis

Statistical analyses were performed with Prism 9 (GraphPad Software, San Diego, CA, USA). Non-linear and multiple regression analyses were applied to the data curves to derive the best-fitting regression equations to predict the statistical significance of the data. The data from the PEF exposed groups were compared to each other and to the control group by performing multiple regression analyses to determine the statistical significance of the reported results. For Live/Dead assay results, two-way ANOVA with Tukey post-hoc tests were used. A confidence interval of 95% was applied for all data analyses. The error values were reported as one standard deviation (SD) of the mean of 3 groups.

5.3 Results

5.3.1 Probe Calibration

In theory, an ionic solution with completely dissociable monovalent ions such as NaCl shows no dielectric dispersion < 1 MHz the conductivities of different concentrations of NaCl are known. Therefore, measured conductance can be used to estimate K, which accounts for total equipment noise and various experimental artifacts such as electrode polarization. Conductance of NaCl solutions ranging from 0.0015 M to 0.15 M is shown in Figure 24. For a system without errors, there should be no variation in the measured conductance as a function of frequency. The systemic error (expressed as one standard deviation) is < 8.0 % for all measurements (Table 6). In practice, electrode polarization and experimental artifacts introduce frequency-dependent variations. The data are nearly frequency-independent such that the conductance value at any frequency varies with the ionic conductivity and hence with the concentration of each solution (Fig. 22). A linear relationship exists between the measured conductance at all frequencies and concentrations. The corresponding conductivities have a correlation coefficient of 0.98, and the factor relating conductance and conductivity, K = 0.171 m.

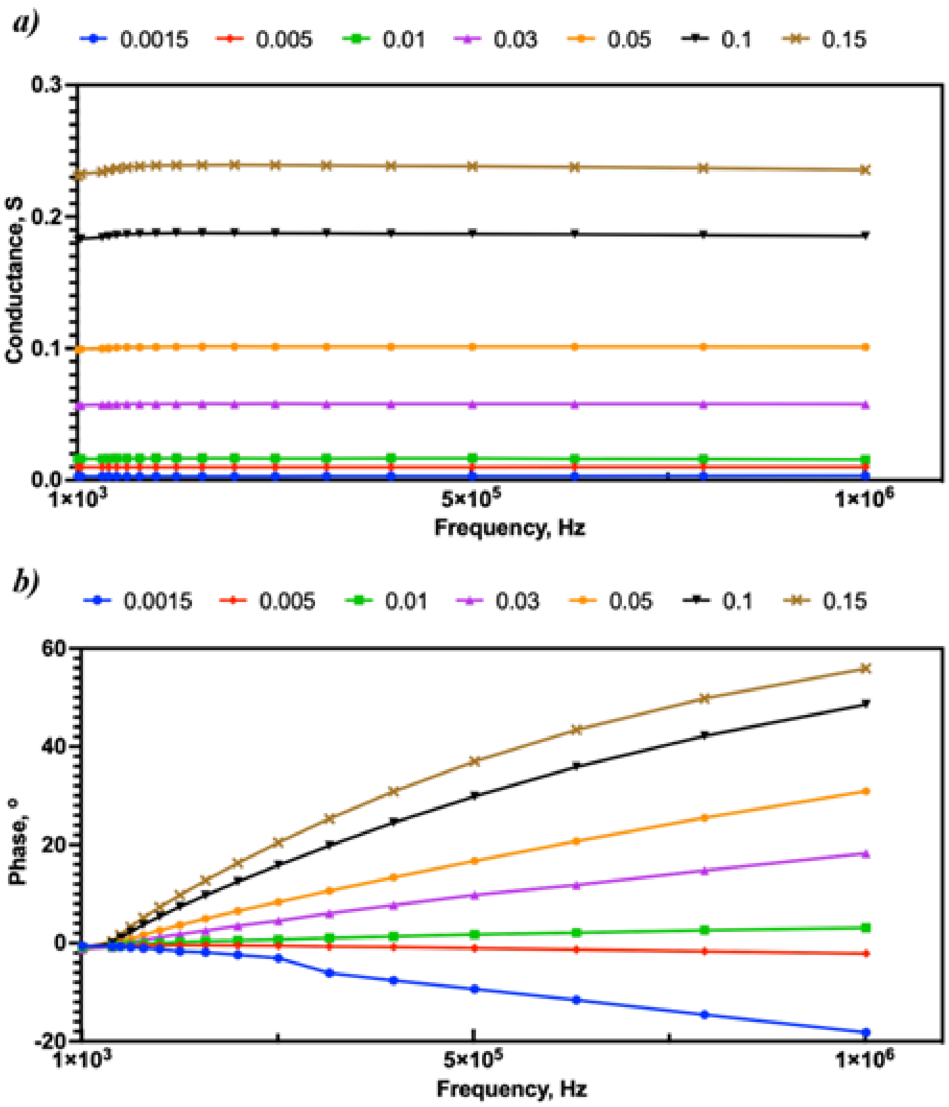

Figure 24. **(**a) Conductance spectra of NaCl solutions with concentrations ranging from 0.0015 m to 0.15 m. These spectra have been used to calculate the probe constant (k). (b) corresponding phase shift for NaCl solutions with concentrations ranging from 0.0015 m to 0.15 m

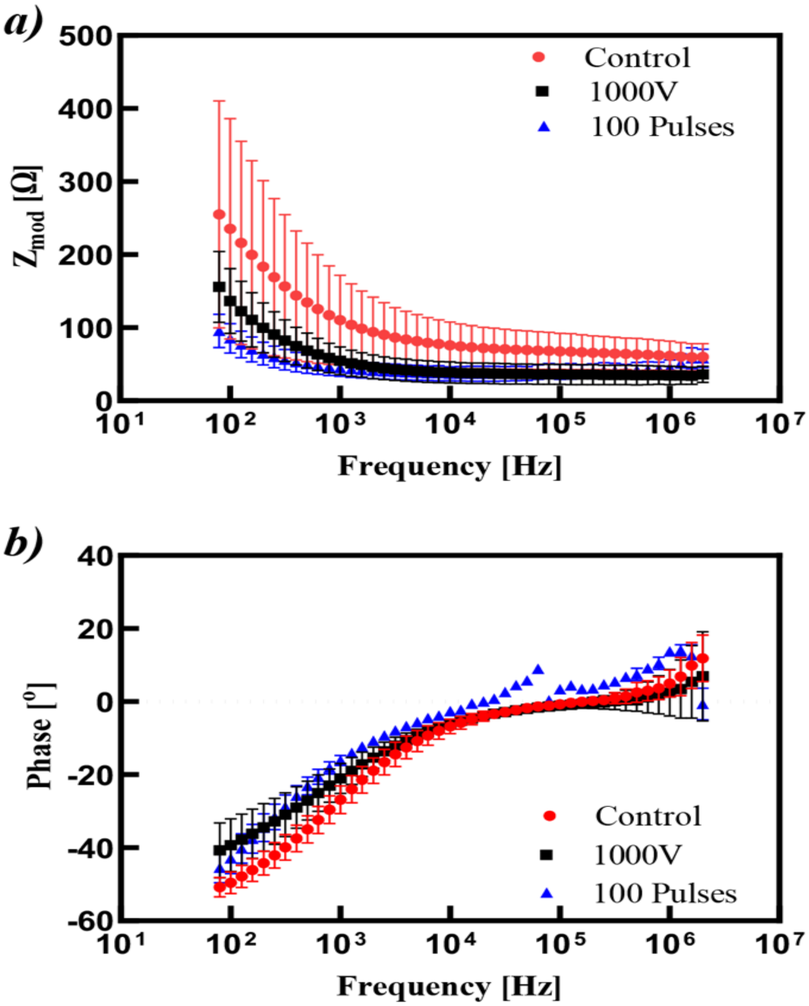

Figure 25. Mean Impedance Modulus and Phase Shift from 80 H_z to 2 MHz of Unexposed and PEF-Exposed AF Cartilage. PEF exposures included a single 100 µsPEF with 1000 V applied, or 100 pulses of 100 µsPEF with 500 V applied. (a) Shows the mean impedance modulus with one standard deviation as error bars. Unexposed cartilage is indicated by the red circles, and the single and the multiple-pulse exposed tissue is marked by back squares and blue triangles, respectively. (b) Shows the mean phase shift with one standard deviation error bars of unexposed and PEF-exposed tissues

5.3.2 Impedance Spectra of AF Fibrocartilage

The average impedance modulus and phase with standard deviation for the unexposed (control) and exposed (one exposed to a single pulse of 100 μsPEF at 4 kV/cm and the other exposed to multiple, 100 pulses of 100 μs duration at 2 kV/cm) tissues are shown in Figure 26. The impedance moduli of exposed and unexposed tissues vary with frequency, with the complex impedance decreasing with increasing frequency. Within the frequency range < 20 kH_z, the impedance moduli decrease after pulse exposures (Fig. 3(a)). Further decreases in impedance moduli occur following multiple pulse exposures. For unexposed AF tissues, the mean impedance modulus varies from 255.0 ± 139 **Ω** over 80 H_z to 2 MH_z the magnitude of the impedance modulus of unexposed AF tissue varied by an average of 50.8 % for all measurements. Across the same frequency range, the PEF-exposed tissue has an impedance modulus ranging from 155.7 ± 43.6 **Ω** with a variance of 55.5 % for tissue exposed to 1 pulse of 100 µs duration at 4 kV/cm. After exposure to 100 pulses of 100 µs duration at 2 kV/cm, the impedance modulus ranges 95.7 ± 18.5 **Ω** to 58.0 ± 10.3 **Ω** with a variance of 28.3%. The impedance modulus and phase were significantly different ($p<0.05$) between the control and exposed tissues at all frequencies. It can be seen in the data reported in Fig. 3(a) that, at higher frequencies, >10^5 H_z, the variation in the complex impedance between PEF-exposed tissue and the control decreases. This is because, at higher frequencies, the capacitive response of the cell membrane reduces allowing current to travel though the tissue with less impedance, hence the less effect of PEF observed. The very minimal variations observed may be attributed to the residual plasma membrane response in the control samples and PEF effect on the extracellular matrix. Similar observations are made for the equivalent conductivity reported in Fig. 5(b).

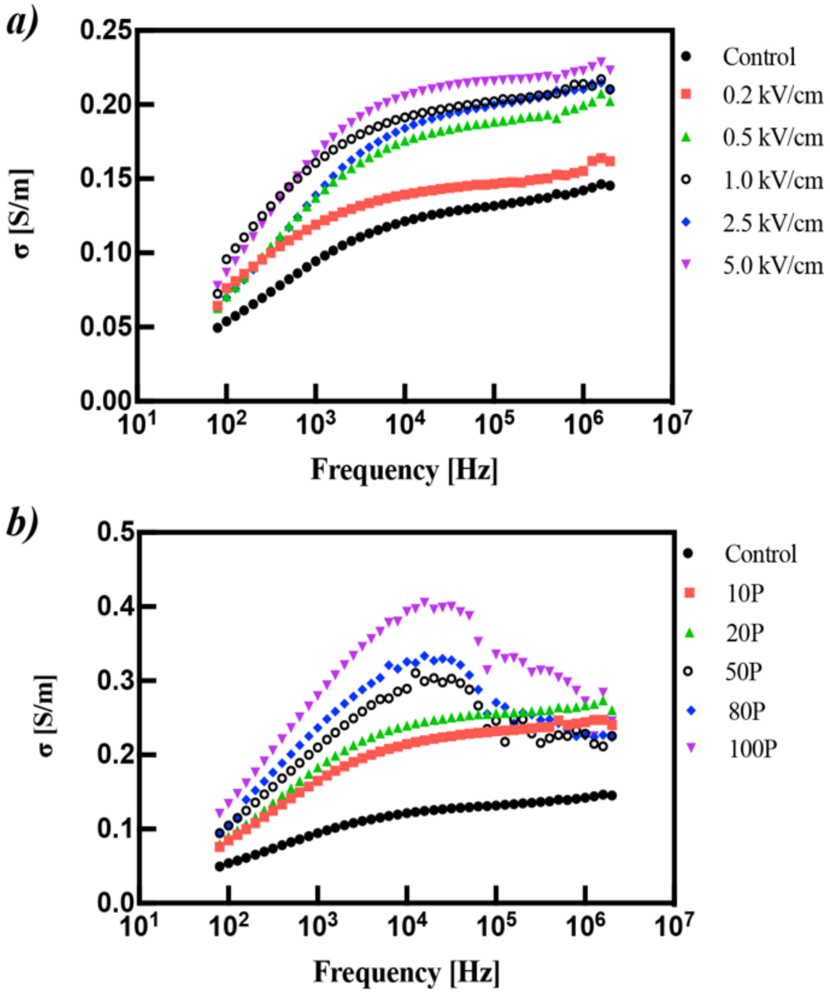

Figure 26. Mean Electrical Conductivity, Σ, of Unexposed and PEF-Exposed AF Cartilage

In figure 27 above, (a) Shows the electrical conductivity of AF cartilage treated with a single pulse of 100 µsPEF with applied voltage ranging from 500 V to 1000 V. The resulting conductivity is reported across the measurement frequency range of 100 Hz to 1 MHz. The difference in mean electrical conductivity between unexposed and PEF-exposed tissue is statistically significant ($p < 0.05$) for all frequencies. (b) The electrical conductivities of tissue treated with a range of 10 to 100 pulses of 100 µsPEF with 500 V applied are plotted as a function of frequency. Data for unexposed and multiple-pulse PEF-treated tissue across all measurements are statistically significantly different ($p < 0.05$) for almost all frequencies. (Error bars not shown for visual clarity.)

The phase data show capacitive responses for the unexposed tissue with a maximum phase shift of -3.9 ^{0} at 20 kH_z, where source current leads the measurement voltage (Fig. 3(b)). The data for tissue samples exposed to 1 pulse of 100 µs duration at 4 kV/cm also demonstrate a maximum phase shift of -3.9 ^{0} at 20 kH_z, like that observed for the unexposed tissue. However, a different phase response is observed for tissue exposed to 100 pulses of 100 µs duration at 2 kV/cm. The phase shift at 20 kH_z is 0.05 ^{0}, which suggests more resistive behaviour of the multiple PEF-treated tissue. The high variation in the measured data is not unexpected and can be attributed to factors such as electrode polarization, tissue heterogeneity, and inherent sample-to-sample difference and tissue desiccation. During experiments, both PEF-exposure and impedance measurement were done within 2 min to reduce tissue drying.

5.3.3 Electrical Properties of AF Fibrocartilage

The equivalent tissue conductivity has been determined using the calibration approach and probe constant, K, as described above. Figure 27 presents the conductivity spectra of unexposed and µsPEF-treated fibrocartilage tissue samples. The data show a frequency-dependent σ_{eq} for cartilage tissue exposed to both single- and multiple-pulse of PEF. The σ_{eq} value increases with magnitude of electric field for tissue treated with single pulses and with number of multiple pulses. Changes in σ_{eq} were more pronounced at 20 kH_z, corresponding to the maximum phase shift in Figure 27(b). At 20 kH_z, σ_{eq} of AF cartilage increases from 0.13 $\pm$ 0.05 S/m to 0.19 $\pm$ 0.06 after PEF of < 1 kV/cm for single-pulse exposures (Fig. 24(a)). Given multiple pulses at 2 kV/cm, σ_{eq} increases from 0.13 $\pm$ 0.05 S/m to 0.40 $\pm$ 0.09 S/m at 20 kHz (Fig. 24(b)).

Our initial hypothesis of PEF exposures having a significant effect on the electrical properties of the cartilage is further ascertained based on the reported p-value. From statistical analysis, a p -value < 0.05 indicates that the observed changes in tissue equivalent conductivity because of PEF exposures as reported in Fig. 24 are statistically significant. Therefore, measuring tissue electrical conductivity can be used to quantify the effects of PEF exposures on cartilage tissues.

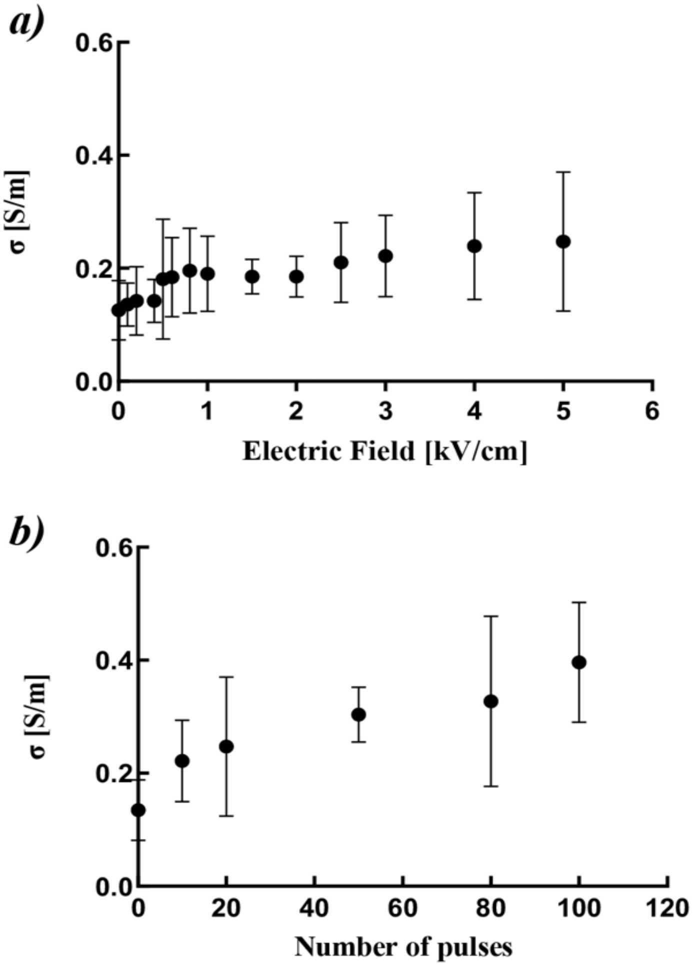

Figure 27. Plot of Mean σ_{eq} at 20 Kh$_z$ for PEF-Treated Samples as a Function of the Applied Electric Field and the Number of Pulses. (a) Mean σ_{eq} at 20 kH$_z$ increases for AF cartilage exposed to 1 pulse of 100 µsPEF with increasing electric field strength, as compared to paired, unexposed controls. (b) Mean σ_{eq} at 20 kH$_z$ increases for AF cartilage exposed to increasing number of pulses (10 to 100), as compared to paired, unexposed controls

5.3.4 PEF-Induced Cell Permeability to Fluorophores

Cell permeation following PEF exposure commonly is measured by the influx of a fluorescent molecule, such as the ethidium homodimer (red, for "dead"), that otherwise would not penetrate the cell plasma membrane. Additionally, depressed fluorescence intensity of calcein (green, for “live”) inside a cell indicates loss of membrane integrity and interruption of intracellular esterase activity. Cell survival for PEF-exposed AF cartilage is expressed as the ratio of the number of live cells to the sum of live and dead cell counts, expressed as a percentage. The percentage of live cells in PEF-exposed tissue is compared to unexposed, control AF tissues, indicating decreased survival with increasing electric field strength (Fig. 25(a)) and number of pulses (Fig. 25(b)). Representative fluorescence microscopy images with the Live/Dead assay show nearly all cells are green and alive in controls, whereas more red and dead cells appear with more intense PEF exposures (Fig. 26). Data presented from the Live/Dead microscopy assay (Fig. 25) illustrate cell survival trends comparable those of σ_{eq} (Fig. 24).

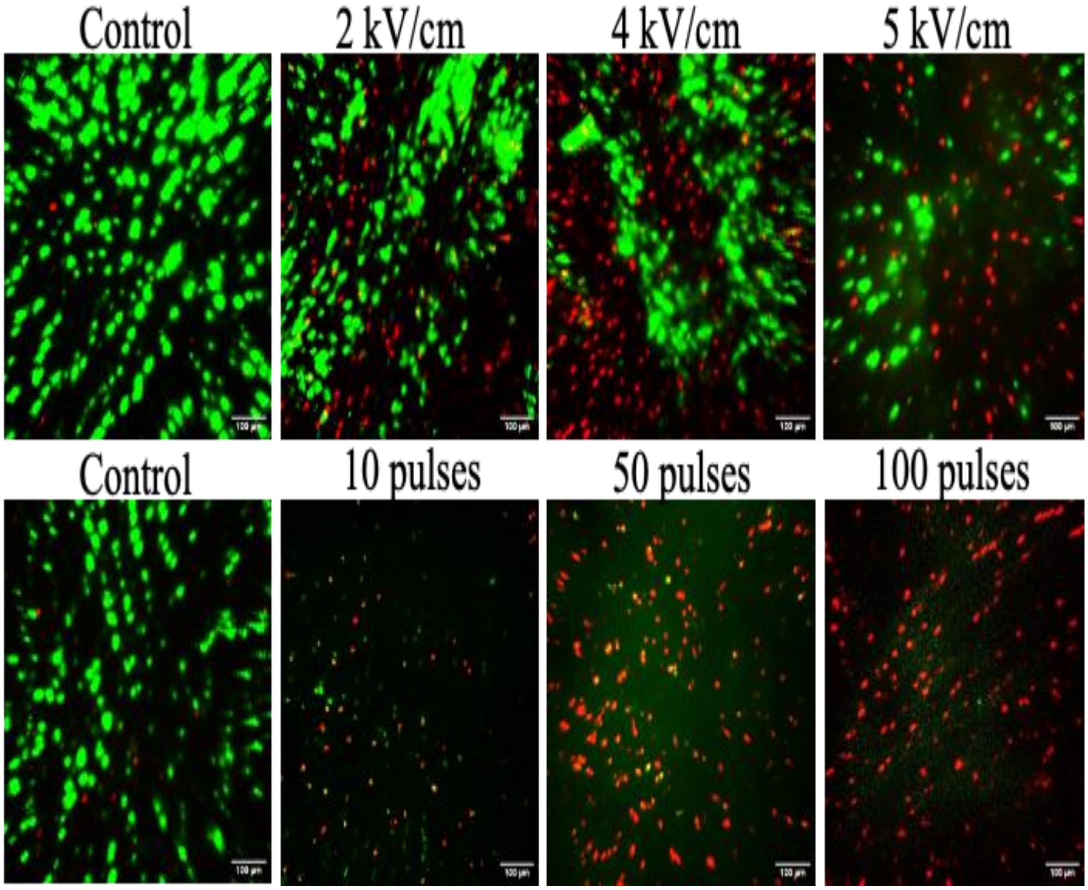

Figure 28. Representative Live/Dead Assay Confocal Fluorescence Microscopy Images of AF Cells within Unexposed (Control) and PEF-Exposed Cartilage Tissue. Control images show cells are only stained bright green (live), whereas increasing electric field strength (top) and number of pulses (bottom) exhibit increased number of cells stained red (dead). Each image represents a projection of maximum intensity from a Z-stack combining 6 images. Image contrast has been enhanced for visualization. Scale bars represent 100 µm

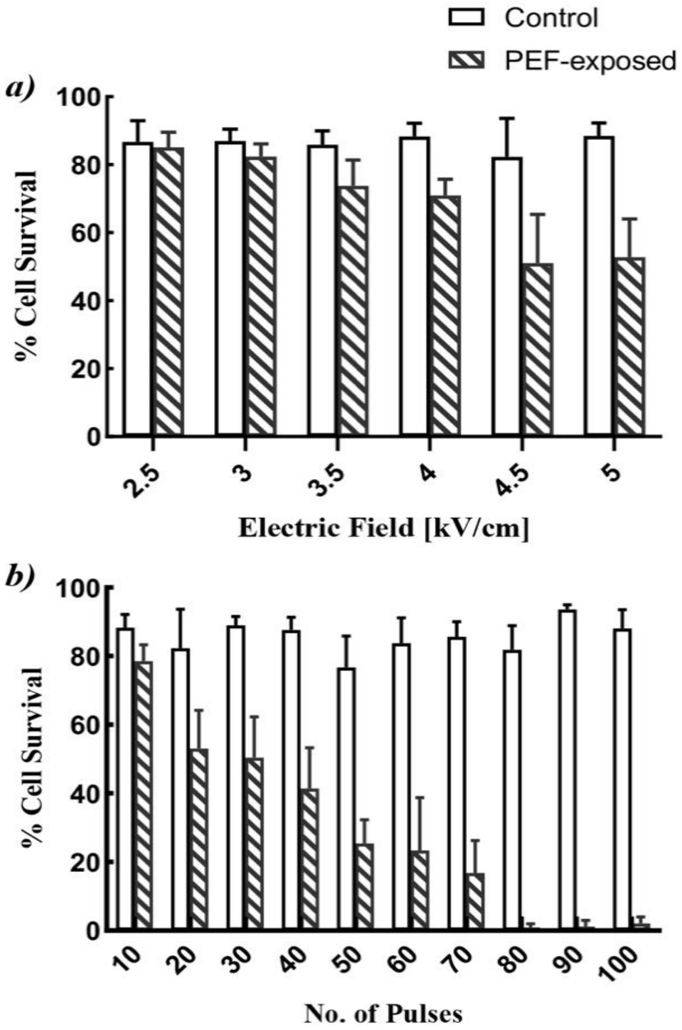

Figure 29. Cell survival in AFtissue following $\mu sPEF$ treatment has been determined using a Live/Dead Assay with Calcein-AM/Ethd-III. Cell survival decreases in tissue treated with a single pulse of 100 µsPEF with increasing electric field strengths of 2.5 kV/cm to 5 kV/cm, as compared to paired, unexposed tissue. (b) Cell survival decreases in response to treating tissue samples with increasing number of pulses (10 to 100) of 100 µsPEF at 2.5 kV/cm. Error bars represent one standard deviation ($p < 0.01$)

5.3.5 Effective Dose Response

The biological effects of PEF exposure often depend on the total *SDD* or specific dose delivered. The total *SED* can be used as a universal metric to quantify effects caused by PEF exposure according to (4), which accounts for variation of both E and n, SED [kJ/g] is calculated and used to compare results from EIS measurements and Live/Dead assays. Plotting the percent change in σ_{eq} from EIS and in cell survival from Live/Dead assay reveals similar trends in the curves from the two methods (Fig. 8). The curves appear to cross-over around 50 %, and the median lethal dose (LD_{50}) of PEF exposure for AF cells in bovine AF cartilage is about 0.283 kJ/g.

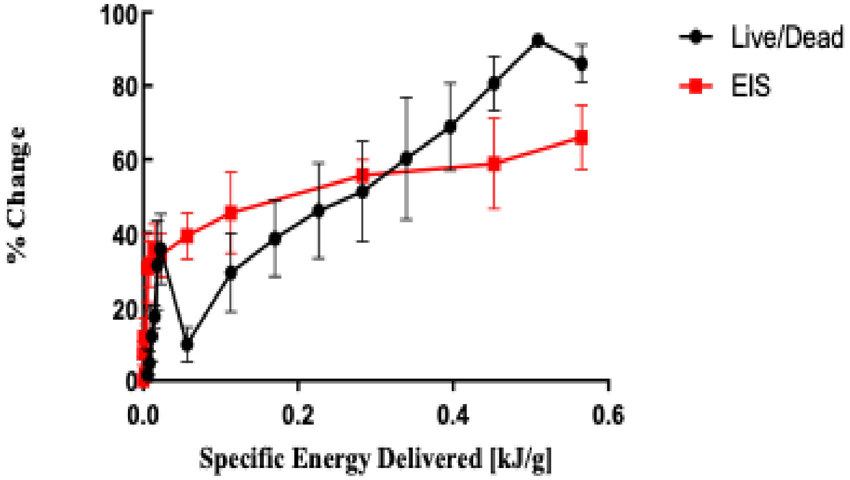

Figure 30. The percent changes in af cell survival (Live/Dead) and tissue conductivity (EIS) rise together with increasing total SED from PEF Exposure. Error bars represent one standard deviation

5.4 Discussions

Two electrically conductive compartments exist in biological tissues – extracellular and intracellular spaces, which are separated by the cell plasma membrane. The intact cell membrane is like an ultrathin capacitor with high resistance that separates the intracellular components from the extracellular environment. This makes conduction of current across the tissue highly frequency-dependent [30]. The tissue impedance spectrum and conductivities across a frequency range therefore reflect the properties and structures of tissues. The impedance and phase spectra reported herein for the unexposed AF cartilage are consistent with those reported for other cartilage types [31], [32]. For AF cartilage, impedance increases steeply at low frequencies because the cells and extracellular structures of the AF cartilage are highly aligned and interconnected. At low frequencies, the low currents applied only travel within extracellular fluids surrounding the cells' highly resistant plasma membranes, giving rise to high impedance. As the frequency of the applied current increases, tissue impedance decreases due to the predominantly capacitive behavior of the lipid bilayer. PEF exposure leads to a transient breakdown of the dielectric barrier presented by the lipid bilayer, causing electropermeabilization which decreases the resistivity of the cell plasma membrane. This explains the lower impedance values in the PEF-exposed cartilage. Conductivity (the inverse of resistivity) likewise increases with the dielectric breakdown and electropermeabilization of biomembrane.

The increase in tissue conductivity following PEF exposure is consistent with that of many biological tissues reported in the literature [172,261–263,276,277] [177,182], although this is the first report of the effects of PEF exposure on AF cartilage to our knowledge. The AF tissue's σ_{eq} increased with more intense PEF exposures, especially with higher *n*, and total *SED*. Notably, this study has been conducted on dissected tissue exposed to air and at room temperature. These factors can contribute to the variability in the conductivity measurements. The conductivity of biological tissue has been shown to be temperature dependent [37]–[39]. The temperature changes as a result of PEF exposures can be derived though calculating the power input of the electrical pulses. The power input, $\dot{W}$ per pulse was estimated using the equation.

$$\dot{W} = t_p f \left(\frac{V^2}{R}\right) \tag{17}$$

where $t_p$is the pulse width, f is the repetition frequency, V the applied voltage and R the resistance. The associated temperature change in the tissue was estimated with the equation.

$$\Delta T = \frac{\dot{W}\Delta t}{mc_p} \tag{18}$$

where $\Delta t$is the total duration of the applied pulse, m is the weight of the tissue and c_p the specific heat capacity of the tissue. The power input of a single 100 μsPEF at 500 V is 6.3 W with the associated temperature change at 10^{-7} ^{0}C. At 1000 V, a single 100 μsPEF inputs 20.8 W with estimated temperature changes also at 10^{-7} ^{0}C. For the multiple pulses investigated, 100 pulse at 500 V inputted 568.2 W with estimated temperature change of 10^{-5} ^{0}C.

Tissue conductivity post-mortem also can be affected by the rapid redistribution of tissue fluid, which is similar to the vascular occlusion effects that occur due to PEF exposures and cellular changes that occur several hours post-mortem [263]. To mitigate some of these effects, all experiments were performed 4 h post-mortem. Another potential source of error is a lack of pressure control between the two parallel plates, and the flow of current can be impeded by formation of ionic layers at the surface of the electrodes. Maintaining tight contact between the electrode and tissue is paramount for the accuracy of the data collected using the two-electrode EIS configuration. Current flow though the dielectric tissue also contributes to Joule heating, and although μsPEF is a non-thermal technique, small temperature gradient changes alter conductivity properties in the system. Additionally, large deviations σ_{eq} can be explained by the AF tissue anatomy. The AF cartilage is made of tightly packed collagen fibres and cells, which reduces the pathways for current to flow, leading to large extracellular resistance. Upon PEF exposure, membrane resistance decreases, and the relative conductivity of the AF tissue increases. The presented results capture changes in both cells and ECM, especially at higher total *SED* and with repeated pulses that build consecutively on induced changes. This could explain the shift in slopes from single to multiple pulse exposures seen in Fig. 8 for both Live/Dead and EIS curves. One way to estimate the changes in the ECM as a result of PEF-exposure will be to disrupt the cell membrane in the tissue by freeze-thawing cycles prior to pulse treatments. This way, the changes observed cannot be attributed to the permeation of the cell membrane.

The above-noted drawbacks of *ex vivo* impedance measurements have to do with the physiological condition of the dissected tissue as compared to *in vivo* conditions. However, isolated tissue enables the characterization of uniform sample. Accurate translation of voltage and current across a desired tissue structure helps determine conductivity without the interference of macroscopic anatomical structures.

To validate the assumption that conductivity changes are related to electropermeabilization of cells in the AF cartilage, the fluorescence intensities of calcein and ethidium homodimer dyes were quantified and compared to changes in σ_{eq}. Similar trends are observed between the optical measurements and impedance measurements. The high sensitivity of the cells to PEF exposures results in cell permeabilization and increased tissue conductivity. The lethal dose data show an LD_{50} for both measurement conditions around 0.283 kJ/g. Overall, PEF exposure response measurements from EIS agree well with the optical measurements and existing experimental data. This suggests EIS is advantageous for quantifying responses to *in vivo* PEF exposures, as well as decellularization and recellularization in both *ex vivo* and *in vivo* processes. The EIS technique has the potential to measure in real-time pulse-on-pulse effects in both tissue and cell which can give more details on the dynamics of the change in tissue electrical properties. However, our EIS instrumentation is not equipped to monitor membrane permeation and impedance changes at a shorter timescale. That said, the 2 min time PEF-exposures and impedance measurements is a good time resolution to measure physiological changes.

5.5 Conclusion

EIS and conductivity measurements of biological tissues following PEF exposures is a fast, sensitive, and reliable approach to quantify the effectiveness of µsPEF applications. This study measured the conductivity changes as a result of exposing AF cartilage to different sets of parameters of µsPEF. The conductivity analysis compared favorably when compared to optical measurements. EIS is sensitive enough to detect small changes (< 10 %). Further studies are needed to continue making EIS a more reliable and effective tool to quantify biological tissue response to PEF exposure in vivo. Our future efforts will focus on using EIS to compare decellularization methods, investigate structural changes in cartilage following PEF exposures, and delineate thermal effects of PEF exposures.

Chapter 6

Electrokinetic Transport of Charged Molecules Across AF Tissue with PEF

6.1 Introduction

A charged particle in a liquid electrolyte under the application of an electric field experiences Coulombic forces leading to enhanced migration of the charged particle [197,202,203]. This is known as the electrokinetic phenomenon, which encompasses electrophoresis [280], electroosmosis [281], dielectrophoresis [282] and electrical streaming potential [283].

Electrokinetics is used to enhance the transport of molecules which would otherwise be transported slowly by diffusion. The different aspects of the electrokinetic phenomenon contribute to the functions of many biological tissues and have practical applications in DNA separations and transfection [198,220], microfluidics [284], tissue histology [206,285] and drug delivery [286].

Tissue electrophoresis is used in combination with chemical and biological agents to remove light scattering molecules from the tissue to enable deep imaging into the tissue by a process known as tissue clearing [221]. For example, in the tissue clearing protocol CLARITY, a detergent captures the lipids within micelles. Electrophoresis carries the negatively charged micelles along the path of the electric field. Electrophoretic tissue clearing enhances the speed of extraction from weeks to hours for a mouse brain [221,222,224,287]. However, if the electric field is strong, it causes formation of acidic bubbles and increased temperature leading to loss of tissue integrity. Also, in the tissue clearing protocol called Stochastic Electrotransport, Kim et al. used electrophoretic flow in a rotational electric field to drive electromobile molecules into and out of the tissue [225]. The rotational field reduces the applied electric field strength required to achieve transport of the molecules. However, the high voltage and rotation speed may result in thermal and mechanical damage to the tissue. The mobility of the charged molecules depends on the applied electric fields, but strong electric fields cause increased temperatures as a result of Joule heating [288].

Due to the flow of current, Joule heating becomes an inevitable part of the electrokinetic flow process. This internal heat source leads to significant increase in temperature in the liquid. Elevated temperatures can be detrimental to biological samples [289], whereas in microfluidic applications it can be beneficial [290]. Most material properties are temperature-dependent. Hence, Joule heating affects the physical properties of liquid electrolytes, including: fluid viscosity, dielectric constant, thermal conductivity, and electrical conductivity [209,291]. The temperature gradient causes band broadening and dispersion leading to inefficient separation and irreproducible results [209]. Therefore, Joule heating limits the amplitude of electric potential that can be applied for efficient electrokinetic applications. Herein, we hypothesize that pulsed electric fields (PEF) mitigates Joule heating and associated temperature gradient effects while achieving comparable electrophoretic mobilities of small molecules in gel electrophoresis when compared to direct current (DC) electric fields.

The rate of migration as well as the direction of migration of the charged particles are influenced by both the type and amplitude of the applied electric fields. The DC and PEF have different mechanisms of attaining the stationary velocity of the charged particle relative to the electrolyte medium when the electric field is switched on [4]. When a PEF is turned on, a constant field amplitude is applied and removed at regular time intervals. At pulse start-up, the instance of electrophoretic flow induces migration of the charged particles. When the field is removed, the electrophoretic migration halts quickly, and electroosmotic flow briefly continues movement of the bulk fluid [281]. Usually, the electroosmotic flow is in opposite direction to the electrophoretic flow, which impedes electrophoretic migration of the charged particles [197]. For the DC field, a constant field amplitude is applied, and the electrophoretic migration of the charged particles is initiated when the DC field switches on and is maintained until the field is completely removed. To compute the electrophoretic mobilities of the particles experiencing the different field waveforms, the duty cycle becomes an important parameter.

In this study, we measure the electrophoretic mobility of electromobile particles under DC and pulsed electric fields across fibrocartilage tissue and agarose gel. The temperature changes induced in the electrolyte to quantify the effects of Joule heating. Fibrocartilage tissue consists of an extracellular matrix (ECM) with a hydrated polyelectrolyte containing fixed negative charges on the proteoglycans embedded in a collagen network, with corresponding positive charges distributed in the matrix fluid [14]. The cells within the ECM contain DNA which are negatively charged as result of the sulphate group attached. Fibrocartilage tissue such as the annulus fibrosus has a peculiar ultrastructure and composition defined by the orientation of the fiber network and 60 – 70 % hydration [46–50,65,292–294]. The tissue electro-clearing techniques described above have been used successfully with soft tissues such as brain and kidney but not for tendons, cartilages and fibrocartilages [221]. Electro-clearing techniques can be beneficial for decellularization of fibrocartilage tissue for tissue engineering. Also, the technique can enhance the physiological and cytological characterization of thick 3D tissues such as fibrocartilage [295].

The electrophoretic mobility of charged particles in biological tissue can be measured from the relative difference in velocity of cationic dyes passing though the tissue sample in an agarose gel under an applied electric field. Electrophoretic mobility can be used to estimate the transport of charged biomolecules in the tissue. Here, we use Pyronin Y and Safranin O as model cationic dyes. Safranin O binds ionically to the negatively charged group of chondroitin sulfate on the glycosaminoglycan component of the proteoglycans. Hence, the metachomatic nature of the dye can be used to quantify the proteoglycan content of the tissue [296,297]. Pyronin Y on the other hand binds to both DNA and RNA, and hence, it is used to quantify nucleic acid content and migration [298]. The electrophoretic mobility of the cationic dyes has been measured for the DC and pulsed fields across an agarose gel and though the fibrocartilage tissue embedded within the gel.

6.2 Materials and Method

6.2.1 Dynamic Electrokinetics

The dynamic responses of molecular motion due to electrophoresis and electroosmosis can be expressed though characteristic times, τ_{ep} and τ_{eo}, respectively, which are on the order of ($\mathcal{O}$):

$$\tau_{eo} = \mathcal{O}\left(\frac{\rho r_c^2}{\mu}\right) \tag{19}$$

$$\tau_{ep} = \mathcal{O}\left(\frac{\rho_p a^2}{\mu}\right) \tag{20}$$

where r_c is pore radius, ρ_p is the density of the particle, and a is the particle radius [281]. Assuming the particles behave as hard spheres, the Stokes radii of Pyronin Y (molecular weight, MW_{PY} = 302.8 Da, $\rho_{p,PY}$ = 0.64 g/cm^3) and Safranin O (MW_{SO} = 350.8 Da, $\rho_{p,SO}$ = 1.01 g/cm^3) are a_{PY} = 5.72 Å and a_{SO} = 5.16 Å, respectively. With a viscosity of the buffer solution, μ = 1.01 cP, the electrophoretic characteristic times are $\tau_{ep,PY}$ = 2.08 x 10^{-10} s and $\tau_{ep,SO}$ = 2.67 x 10^{-10} s. Electrophoretic mobility of the dyes occurs approximately in-phase with the applied electric field. Dye molecules accelerate and move steadily (or decelerate and stop) within picoseconds of changes in the electric field.

Electroosmotic motion depends on matrix characteristics. Transport properties though annulus fibrosus tissues are anisotropic [208,299], and particles encounter different ranges of pore sizes based on orientation of the tissue sample. Annular tissue consists of interconnected, concentric lamellae that have alternating collagen fiber orientations. An extrafibrillar matrix containing a high concentration of proteoglycans also impacts the permeability of solutes within the annular tissue. Considering an approximate interlamellar pore radius in bovine annular tissue to be $r_{c,IL}$ = 25 μm [3], and density of the buffer as ρ = 1.05 g/cm^3, the electroosmotic characteristic time is $\tau_{eo,IL}$ = 0.65 s. However, pore radii though the lamellae and extrafibrillar matrix are on the order of $r_{c,L}$ = 50 nm, resulting in $\tau_{eo,L}$ = 2.6 x 10^{-6} s. Pore radii in 1 % agarose also are on the order of 50 nm. Samples have been oriented during experimentation such that dyes should move though the lamellae, in which case the microsecond-duration electroosmotic-driven acceleration and deceleration of dyes occurs relatively in-phase with the millisecond periods of dynamic field changes applied. Thus, linear analysis of dye movement over time is used.

Within the micro- and nanochannels of this system, electrokinetic fluid flow reaches steady-state on the order of milliseconds. Thermal diffusion has a characteristic time on the order of seconds [267]. Steady-state heat transfer due to Joule heating during the dynamic field changes used in this study is not established.

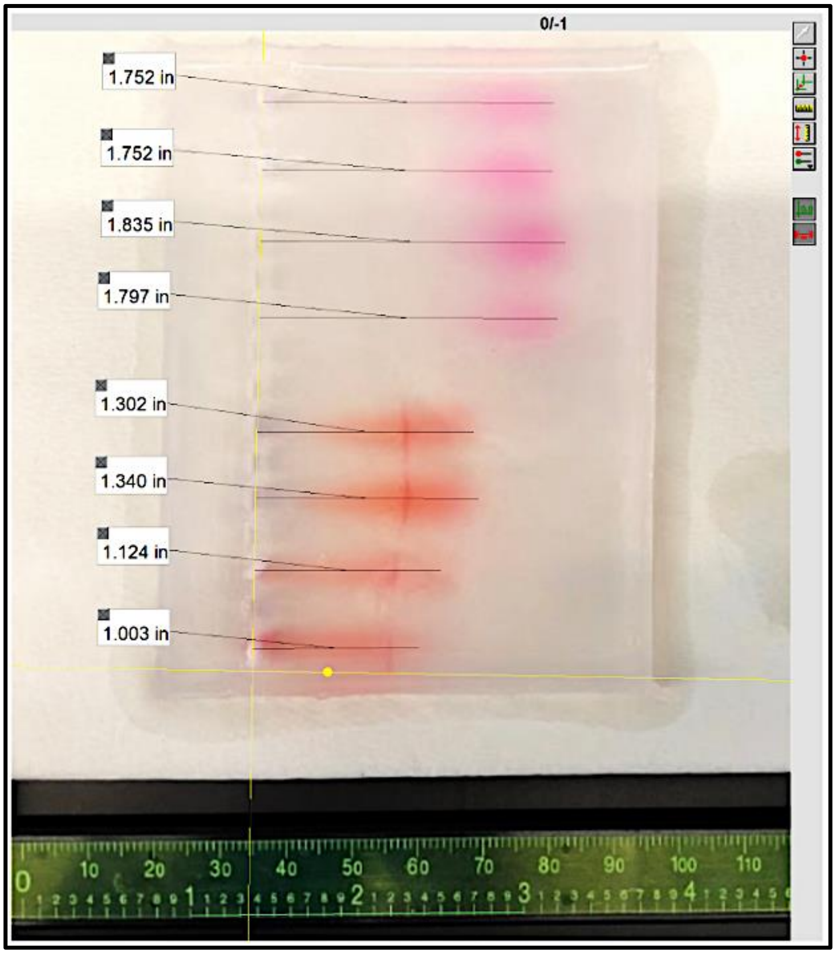

*Figure 31***.** Representative picture shows image analysis of dye movement though tissue and agarose gel following electrophoresis. The top four lanes contain Pyronin Y (pink), while the bottom four lanes contain Safranin O (red). The thin, vertical yellow line indicates the exit plane from tissue samples, which occupy the top two and bottom two lanes. Between are blank control lanes. Tissue samples have been inserted immediately adjacent to dye-loading wells. The total dye migration distance is indicated by values on the left side of the image, after calibration using the ruler on the bottom

6.2.2 Electrokinetic Mobility Determination

The distance of the total observed electrokinetic movement was measured using ImageJ (Fiji) [275] and its measure function (Fig. 1). As shown in Fig. 1, the caliper was included in the image for fiducial purpose. The caliper was used to calibrate the scale in ImageJ using the set scale function. Lines were drawn along the length of the lanes to the leading edge of the visible dye front. The distances for each test lane were recorded, and the observed velocity was calculated for the dye though the tissue, $\vec{u}_{obs}$ [202].

$$\vec{u}_{obs} = \frac{w}{t(1 - \frac{D_i - w}{D_0})} \tag{21}$$

where w is the width of the tissue (mm), t is the time the field was run (s), D_i is the distance traveled by the dye in the sample lane (mm), and D_0 is the average distance in the control lane of the respective field (mm). The observed electrokinetic mobility ($\vec{u}_{obs}$) was then calculated using $\vec{u}_{obs}$from (18).

$$\mu_{obs} = \frac{\vec{u}_{obs}}{E} \tag{22}$$

where E is the electric field strength (V/cm). This approach assumes constant dye velocity thoughout the total experimental time. This is the case for the DC field, but the sawtooth waveform exhibits constant acceleration and deceleration. A temporally symmetric, positive polarity sawtooth field is applied. Since dye molecules move in phase with dynamic changes in electric field strength, per above, the average observed velocities for the sawtooth and square pulse waveforms are used to calculate the corresponding average, observed electrophoretic mobilities. Thus, Equation (19) is modified to factor in the 50% duty cycle of the pulsed and root mean square voltage for the sawtooth pulses in (20) and (21), respectively, as:

$$\mu_{obs,pulse} = \frac{\vec{u}_{obs}}{0.5E} \tag{23}$$

$$\mu_{obs,saw} = \frac{\vec{u}_{obs}}{0.577E} \tag{24}$$

6.2.3 Experimental Setup

The gel was prepared using 1 mL of 50X Tris-borate-EDTA (TBE) buffer (VWR Chemicals, OH, USA; Lot#: 22K1056681) mixed with 49 mL of deionized water. Once mixed, a 500 mg agarose tablet (Bulldog Bio, NH, USA; Lot#: 50201.1008) was added to the solution to make a 1 % wt/vol agarose solution. The solution was thus mixed and microwaved from 30 s and then mixed until clear. It was cast in a 10 cm by 8 cm Expedeon Mini-fast Horizontal Submarine MGU-303 electrophoresis system (Abcam, Waltham, MA, USA). A 1X Tris-acetate-EDTA (TAE) (G-Bioscience, MO, USA; Lot#: 181508) solution was used as the electrolyte. Two dye solutions were prepared, Pyronin Y (MP Biomedicals, OH, USA; Lot#: M4621) and Safranin O (Ward's Science, NY, USA; Lot#: AD-18143), by adding 5 mg of the respective dye and 3 mg of sucrose to 7 mL of the previously prepared 1X TBE Buffer. The dyes have a Na^+ that is ionically bonded to Cl^-, and hence the dyes have an overall +1 charge in aqueous solution. For tests with cartilage tissue, frozen sectioned tissue samples from whole bovine tails acquired from a local abattoir (Bringhurst Meats, Berlin, NJ, USA) were thawed, weighed, and placed in the wells of the gel. Tissue samples were cylindrical with 2 mm thickness and 6 mm diameter. Up to 7 μL of the respective dye solution was added to the wells.

The chamber was connected to an Extech DCP60 (Nashua, NH, USA) power supply for DC electric field application and an A-M Systems Model 4100 Isolated High-Power Stimulator (Sequim, WA, USA) for the square and sawtooth pulsed field applications (Fig. 2). A potential of + 60 V, giving an electric field strength of 6 V/cm, was applied across the gel for 60 min. Images of the gel were acquired at 5 min intervals. A pulse duration of 10 ms within a 20 ms period was applied. Millisecond pulse durations have been shown to induce migration of DNA though nanopores during electrotransfection [218–220]. Also, the pulsed duration was selected to allow for full development of the electrokinetic flow [280,281]. Temperature measurements were taken and recorded using a fiber-optic sensor connected to a Fluoroptic® thermometer (Luxtron® 790, Advanced Energy, Inc., Denver, CO, USA), an infrared temperature gun, and a thermal imaging camera (FLIR ONE Pro, Teledyne FLIR, Wilsonville, OR, USA) for consistency every 5 min.

6.2.4 Statistical Analysis

Two-way ANOVA with Tukey's multiple comparisons tests and graphs were made in GraphPad (San Diego, CA, USA) Prism 9.4.0. Confidence interval? Sample size?

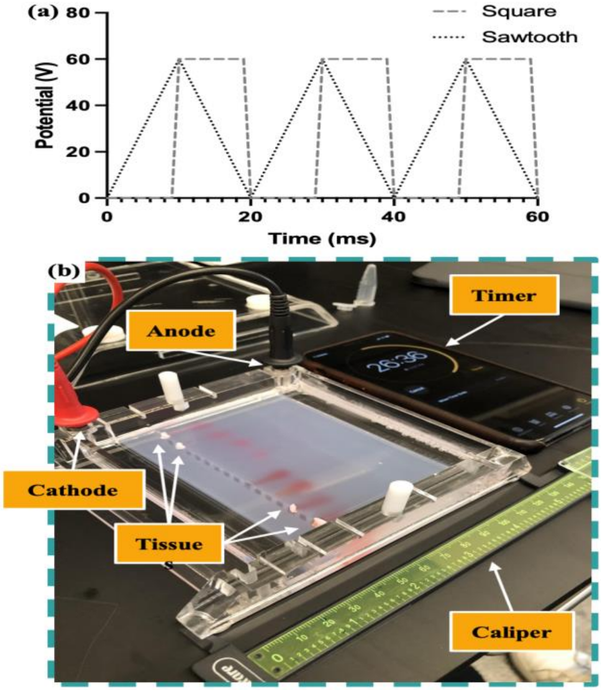

*Figure 32***.** Applied potential Waveforms and Electrophoresis experimental setup. a) Monopolar square and sawtooth pulses of + 60 V are applied with a 20 ms period. Square pulses have a duration of 10 ms. Sawtooth pulses have a linear ascension and descension each of 10 ms duration. (b) A commercial horizontal electrophoresis chamber contains agarose gel in TBE buffer. Tissue samples are embedded within the agarose gel, adjacent to microwells into which dye is injected before initiating electrophoresis. Pyronin Y is in the top four lanes of the gel, and Safranin O is in the bottom four lanes. For visual reference during experiments, a timer and calipers are shown

6.3 Results and Discussion

6.3.1 Electrophoretic Mobilities

Application of electric fields enhance the transport of the cationic Pyronin Y and Safranin O, as expected [202]. The 6.0 V/cm DC field application results in similar electrophoretic mobilities of Pyronin Y ($3.53 \times 10^{-5} \pm 0.31 \times 10^{-5}$ cm^2/V·s) and Safranin O ($2.59 \times 10^{-5} \pm 0.32 \times 10^{-5}$ cm^2/V·s) though bovine intervertebral annulus fibrosus fibrocartilage tissue (Fig. 3(a)). These values are on the same order of magnitude (and approximately double) of those reported for Pyronin Y in bovine tendon fibrocartilage within a 6.7 V/cm DC field [202]. Fiber density and proteoglycan content likely contribute to variation of these values for the different tissue sources. All control measurements of the dyes' migration within agarose gel result in electrophoretic mobilities that are significantly greater than in the tissue (Fig. 3(b)).

Electrophoretic migration of the dyes though a section of annulus fibrosus tissue is driven not only with DC but also pulsed fields. All the tested conditions cause significant migration of each dye within the 60 min duration of application, with DC causing the farthest migration of both dyes. Although the distances traveled by the dyes is greatest when in the DC fields, DC fields result in the lowest electrophoretic mobilities when the pulsed fields' duty cycle of 50 % is considered (2). Comparing Figs. 3(a) and 3(b), the electrophoretic mobility of the dyes is two to three times greater for the agarose gel (Fig. 3(b)) than is reported for the tissue sample (Fig. 3(a)). It is also observed that the mean electrophoretic mobility is higher for Pyronin Y than for Safranin O for all test conditions. Safranin O's lower electrophoretic mobility is consistent with it interacting more strongly with chondroitin sulfate groups on ECM components bound into the tissue. Notably, square pulses result in a significant difference in electrophoretic mobility in the fibrocartilage tissue between Pyronin Y ($4.39 \text{x } 10^{-5} \pm 1.19 \text{ x } 10^{-5}$ $cm^2/V{\cdot}s$) and Safranin O ($2.72 \text{ x } 10^{-5} \pm 0.48 \text{ x } 10^{-5}$ $cm^2/V{\cdot}s$), and square pulses provide a significantly higher electrophoretic mobility than sawtooth pulses for Pyronin Y ($3.04 \text{ x } 10^{-5} \pm 0.23 \text{ x } 10^{-5}$ $cm^2/V{\cdot}s$) in tissue (Fig. 3(a)).

(a) Tissue

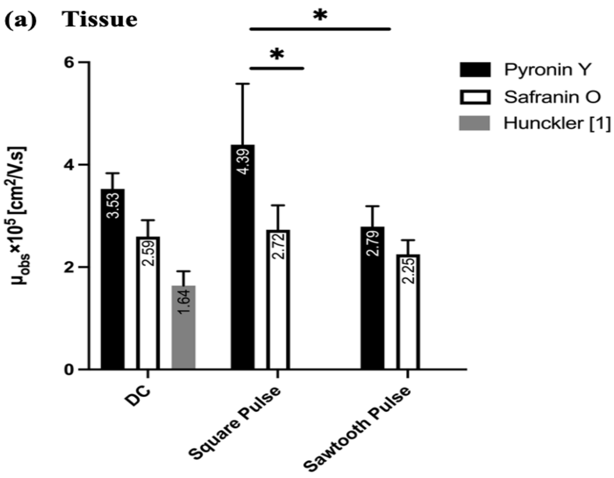

(b) Agarose

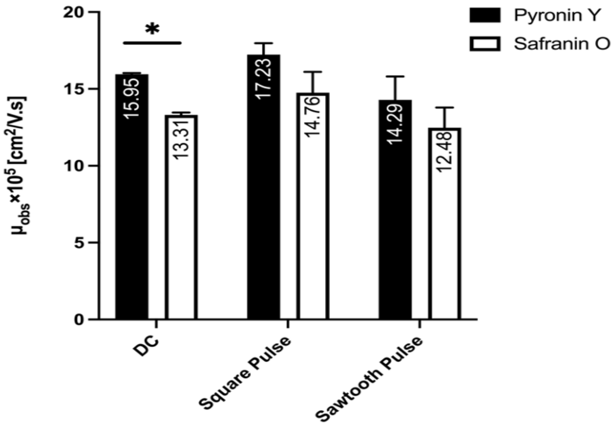

Figure 33. Electrophoretic Mobility, μ_e (Cm^2/V·S) of Pyronin Y and Safranin O in (A) Tissue and (B) Agarose Gel within Different Forms of Electric Field Application (DC, Square Pulse, Or Sawtooth Pulse). Mean values are shown within each column. Error bars represent one standard deviation across n = 3 independent experiments per condition. Statistical significance from the ANOVA results is represented as * $P \leq 0.05$. Note the y-axes of (a) and (b) are scaled differently

6.3.2 Gel Temperature and Joule Heating

Temperature influences molecular motion, and the application of an external electric field generates thermal energy and heat flow within materials. Therefore, we measured the temperature of the middle of the agarose gel thoughout our experiments. The gel’s temperature during DC field application rises by 5.03 ± 0.55 ºC within 30 min (Fig. 4). The DC current steadily increases the temperature of the gel then finally plateaus after 30 min. The increase in temperature can be attributed to Joule heating within the gel when current is applied. The temperature change plateaus after some time because a thermal equilibrium is reached between the gel and the surroundings. At this point, the heat loss equals the heat generation in the system. Temperature changes remain within 1.70 ± 0.36 ºC and 1.30 ± 2.56 ºC of the initial temperature during the entire 60 min for square and sawtooth pulse applications, respectively. Running the experiment with half the electric field strength (3 V/cm) showed no noticeable changes in temperature and no quantifiable particle mobility (results not shown). The different temperatures and their different rates of change for the thee modes of field application suggest electrical power generates much of the thermal energy change [209,288,300]. In our experiment, applying a DC current of 24 mA resulted in a temperature increase of 5.03 ± 0.55 ºC. However, in CLARITY applications, current of 1.2 A is applied across the chamber [287], necessitating the need for liquid perfusion across the chamber to dissipate heat.

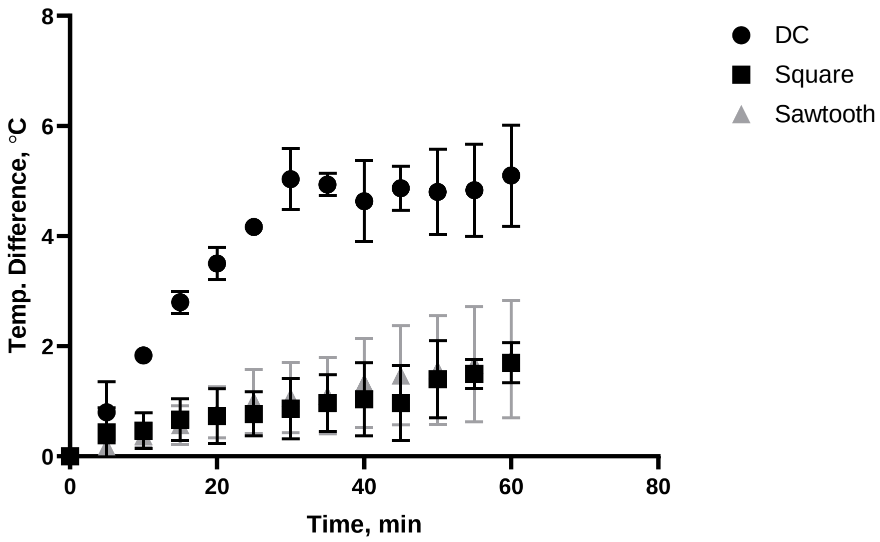

Figure 34. Mean Difference in Temperature of Center of Agarose Gel in TBE Buffer During Electrophoresis using different forms of Applied Electric Field. The difference is relative to the initial room temperature recorded at the beginning of each experiment. Error bars represent one standard deviation across n = 3 independent experiments per condition

6.4 Conclusion

Pulsed electrophoresis using square and sawtooth waveforms drives small, charged molecules though fibrocartilage tissue with a reduced rate of temperature increase compared to DC electrophoresis. Limiting thermal accumulation and corresponding changes molecular motion bolsters electrophoresis as an analytical technique for physiologically-relevant tissues. Furthermore, square pulses are shown to separate small molecules of similar size and charge that differentially interact the cartilage, adding to the technique’s capability. These results also suggest a benefit to preclinical electroextraction, decellularization, or electro-clearing applications that seek to limit collateral damage to tissues while accelerating the removal of certain types of biomolecules from a biomaterial sample to be examined or implanted.

Chapter 7

Enhanced Annulus Fibrosus Tissue Decellularization Using Pulsed Electric Fields

7.1 Introduction

Repairing the annulus fibrosus (AF) tissue of the intervertebral disc (IVD) has proved to be a challenging task for the past decade [301,302]. Intervertebral disc disease is known to be frequently associated with lower back pain [60,66], with prevalence of over 80% and significant health economic burden [3,60,66,228,230]. Common treatment methods include surgical fusion, discectomy, and total disc replacement. However, these procedures are often associated with limited mobility in the spine and potentially accelerated injury to adjacent discs [41]. Therefore, tissue engineering of both the NP and AF have been investigated. Preferably, a minimally invasive approach that preserves most of the anatomical structures and restore disc height and physiological flexibility [3]. Nucleus replacement prostheses are able to restore disc height and flexibility, but there is a high risk of the nucleus extruding though the intervertebral disc cavity [43,303,304]. Repair techniques address the persistent re-herniation of the IVD though the annulus and enhance the development and repair of the nucleus pulposus. An improved method is required to seal the annulus to keep the nucleus prosthesis in place. Early attempts to address this problem were with early AF closure devices including insertion of solid mechanical barriers and suturing and gluing techniques [37,41] but were only partly successful due to implant dislocation and damage to adjacent soft tissue by solid implants [305].

Therefore, innovative biological repair strategies are needed to enhance AF repair. Cell-based therapy; injection of growth factors; and enzymatic inhibitors have shown great potential to repair the tissue at the onset of disc disease [40]. However, growth factors and enzymatic inhibitors have short half-lives, limiting their ability to fully treat disc degeneration [42]. AF tissue engineering strategies combine scaffolds with healthy cell sources to provide the required avenue to develop AF tissue. Several synthetic AF scaffold designs have been developed, including polyamide nanofibers, alginate/chitosan hybrid fibers, demineralized bone matrix gelatin/polycaprolactone triol malate, and demineralized and decellularized bone. Synthetic scaffolds show good elastic properties and allow for AF cell attachment and proliferation [38,39,41,44,45,61,62,118,306]. However, these artificial scaffolds are not able to mimic or replicate composition and microstructure of AF tissue due to the complicated nature of the lamellar structure and uneven distribution of components [3], [40], [62], [307].

Decellularized AF tissue advantageously retains most mechanical structure and properties of native AF tissue [3]. The native matrix proteins furthermore reduce the risk of rejection following implantation. Allograft tissue scaffolds do not require anticoagulant and have superior hemodynamic properties. Unfortunately, the supply of allograft scaffolds is limited [164]. Decellularized exogenous tissue grafts on the other hand are readily available. Xenograft scaffolds function well as a support material and regulate cellular functions, such as cell survival, proliferation, morphogenesis and differentiation [166]. Several techniques, categorized into chemical, biological and physical methods have been used to decellularize exogenous biological tissues [164–166]. Chemical agents such as Triton X-100 and sodium dodecyl sulphate (SDS), and biological agents such as

Trypsin/Ethylenediaminetetraacetic acid (EDTA), have been used to decellularize AF tissue [3]. However, these agents significantly reduce the glycosaminoglycan (GAG) content of the tissue and disrupt tissue ultrastructure. Cell removal by chemical and biological agents usually is diffusion limited which makes it dependent on tissue thickness and temperature [3],[166].

Beyond a given threshold of the transmembrane potential, the damage to the membrane becomes significant, leading to loss in cell homeostasis and eventual cell death, a phenomenon known as irreversible electroporation (IRE) [168,169,171]. Philips et al. demonstrated the potential of decellularizing arterial constructs by controlled cell ablation using IRE [188,190]. In the study, both pin and plate electrode set-ups were used to deliver up to 90 pulses of 100 µs pulses to the artery at 1.75 kV/cm field strength. They showed that decellularization can be achieved with NTIRE and the body’s host response. However, this study was conducted *in vivo*, and the extent of cell ablation was not measured. Thermal damage to biological tissue starts at 42 °C [308], and ECM could be damaged by Joule heating associated with IRE [309]. Joule heating is influenced by pulse parameters, and prior studies have used a pulse frequency of 1 Hz to minimize heating effects [188,190,211]. Though these studies reported no thermal damage, the temperature change due to Joule heating was not experimentally measured.

In this study, NTIRE is employed to controllably ablate cells in explanted AF tissue using PEF of microsecond durations (μsPEF). The extent of tissue electroporation can be detected optically by fluorescence microscopy or electrically by bioimpedance spectroscopy [177,268,274]. After the non-thermal ablation of the cells, longer millisecond pulses are applied to electrokinetically extract cellular materials and immunogenic materials leaving an intact ECM. The parameters for inducing cell death and subsequent extraction were determined in prior studies [252,310]. For comparison, bovine AF tissue samples were decellularized with establish methods such as using Triton X-100 and SDS as detergents [8,164,311]. The decellularized constructs are compared by means of DNA and GAG content assay and histological analysis of the components of the scaffolds. The results show that PEF decellularized scaffold retained the critical biochemical and structural components of the ECM whiles efficiently removing the DNA and cellular materials in a shorter time.

7.2 Materials and Method

7.2.1 AF Tissue Harvesting

Whole bovine tails were acquired freshly harvested from a local abattoir (Bringhurst Meats, Berlin, NJ, USA) without the skin to reduce contamination. Intact intervertebral discs (IVDs) were dissected using #10 and #22 scalpels and a band saw within 4 h of sacrifice under sterile conditions and kept hydrated in saline solution. The fresh AF tissue was isolated and sectioned with 6 mm biopsy punches along the circumference of the disc, perpendicular to annular fibre orientation. The sectioned AF tissue samples were immediately prepared for the decellularization.

7.2.2 Decellularization with PEF

A BTX® Gemini X2 electroporation system (Holliston, MA, USA) with stainless steel calliper electrodes was used to expose AF tissue at room temperature. Tissue samples of 6 mm diameter and 2 mm thickness were sandwiched between filter paper soaked in 1X Tris-borate-EDTA (TBE) buffer solution. Callipers were closed gently until the sandwiched sample completely contacted the pad and electrode surfaces. The pulse parameters used, 50 pulses of 100 µsPEF at 500,V were determined to disrupt the membranes of the cells in the AF tissue to release the intracellular components without disrupting the extracellular membrane [164]. After ablation with the short intense pulses, the tissue samples are then placed in a custom chamber (Appendix D) and subjected to electrokinetic flow with relatively longer millisecond pulses. The chamber was connected to an A-M Systems Model 4100 Isolated High-Power Stimulator (Sequim, WA, USA) to continuously deliver PEF of 10 ms duration. A potential of + 100 V, giving an electric field strength of 20 V/cm, was applied across the platinum electrodes within the chamber for 3 h. The pulse parameters were selected such that no thermal damage is caused to the tissue as a result of Joule heating [310]. Then AF samples were incubated with 0.2 µg/mL RNase A and 0.2 mg/mL DNase I at 37^0C for 24 h. Finally, decellularized AF was washed with PBS for 24 h to remove residual reagents. The control samples were also washed in PBS.

7.2.3 Detergent Decellularization Methods

Triton X-100: Bovine AF tissue sections were placed PBS and subjected to 3 cycles of freeze-thawing. Then AF samples were agitated in Tris-HCl buffer with 3% Triton X-100 (Sigma), 0.1% EDTA and 10 KIU/mL aprotinin at 4^0C for 48 h. The solution was changed every 24 h. Then AF samples were incubated with 0.2 µg/mL RNase A and 0.2 mg/mL DNase I at 37^0C for 24 h. Finally, decellularized AF was washed with PBS for 24 h to remove residual reagents. All steps were conducted under continuous shaking.

SDS: Two groups of bovine AF sections were placed PBS and subjected to 3 cycles of freeze-thawing. After 3 cycles of freeze-thawing, group one of AF samples were decellularized with 10Mm Tris-HCI buffer containing 0.5% SDS (Sigma), 0.1% EDTA and 10 KIU/ml aprotinin at room temperature for 72h. Group two of the AF samples were decellularized with 10Mm Tris-HCI buffer containing 1% SDS (Sigma), 0.1% EDTA and 10 KIU/ml aprotinin at room temperature for 48 h. The decellularized solution was refreshed every 24 h. Decellularized AF was incubated with 0.2 µg/mL RNase A and 0.2 mg/ mL DNase I at 37 °C for 24 h, then washed with PBS for 24 h to remove residual reagents. All steps were conducted under continuous shaking.

7.2.4 Decellularization Efficacy

7.2.4.1 DNA Quantification. Total DNA was extracted from known weights of lyophilized native and decellularized tissue samples using the Blood dsDNA Miniprep System (Promega Reliaprep), according to the manufacturer's instructions. Extracted DNA was quantified at an absorbance of 260 nm (Nanoquant quartz microplate with, Tecan Infinite F200Pro plate reader) and expressed in ng/mg^{-1} of dry tissue weight.

7.2.4.2 GAG Quantification. Known weights of lyophilized NP, iAF and oAF samples were digested in papain solution (5mM L-cystine hydrochloride, (Sigma-Aldrich),: 5 mM EDTA,; and 800 kU.ml-1 papain, (AppliChem),; pH 6.0) at 60^{0}C for 24 h. Sulfated GAG content was quantified according to the Blyscan sGAG assay kit manual (Biocolor, Carrickfergus, UK). Briefly, chondroitin sulfate standard and test samples (40µL) were added to flat bottom 96-well plates with 250µL 1,9 di-methylmethylene blue (DMMB); (Biocolor). After 2 min, the absorbance at 525 nm was measured. The GAG concentration of the test samples was interpolated from the linear region of the standard curve, taking into account the dilution factor, and expressed in µg.mg^{-1} dry weight. The GAG concentration in µg.mg^{-1} was normalized against the GAG content in dry weight of the AF tissue.

7.2.4.3 Histology. After decellularization, tissue specimens (n = 10) were mounted with optimal cutting temperature (OCT) compound and cryosectioned at 10 µm thick by use of a microtome, Cryostar NX50 (Thermo Scientific) and mounted on glass slides. Hematoxylin and eosin (H & E) staining (Leica Biosystems) was used to evaluate the cellular content and general structure of the AF. Proteoglycan was visualized by Safranin O (Ward's Science) staining. Sirius red (Biocolor) stain was used to visualize collagen distribution and orientation on an Olympus CKX53 using the Moticam X camera.

7.2.4.4 Scanning Electron Microscopy (SEM). Decellularization and control AF samples were freeze-dried, cut along the transverse plane by use of a sharp blade, then loaded onto aluminum studs, sputter-coated with gold, and examined under a field emission scanning electron microscope (Phenom^{TM} Pure). Morphological changes were compared before and after treatment.

7.2.5 Cytotoxicity Assay

7.2.5.1 Isolation and Culture of AF Cells. Whole bovine tails were acquired from a local abattoir (Bringhurst Meats, Berlin, NJ, USA) without the skin to reduce contamination. Intact IVDs are dissected within 4 h of sacrifice while being kept hydrated in saline. Under aseptic conditions, AF tissue was isolated with a 6 mm diameter biopsy punch (Integra) and transferred into a specimen container. The isolated fibrocartilage tissue was minced and incubated overnight in collagenase P solution, made by dissolving 50 µg of collagenase enzyme (Rockland Immunochemical, Philadelphia, PA, USA) in 10 mL growth media. The growth media consist of Dulbecco's modified Eagle Medium (DMEM) (Thermo Fisher Scientific, Bridgewater, NJ, USA) supplemented with 10 % fetal bovine serum (Thermo Fisher Scientific, Bridgewater, NJ, USA) and 1 % antibiotic antimycotic

(Thermo Fisher Scientific, Bridgewater, NJ, USA). After digestion, the suspension is sieved though a 100 μm cell strainer, centrifuged at 1200 rpm for 5 min, and the pellet re-suspended in fresh growth media. The cells were counted and seeded in monolayer cell culture flasks at a concentration of 2×10^5 cells/mL then incubated at 95 % humidity, 5 % CO2 and 37 ^{o}C until 90 % confluency. The medium was changed every 3 days. Cells at passage 3 were used in this study.

7.2.5.2 Cell Seeding. Prior to cell seeding, PEF-decellularized AF was disinfected with 70% ethanol, thoroughly rinsed in sterile PBS for 24 h, and immersed in DMEM containing 10% FBS and 1% antibiotics for 24 h. The liquid on the surface of decellularized AF was dried by use of sterile filter paper, then 100μL of cells suspension containing $1x10^6$ AF cells was seeded onto each decellularized AF sample. After the 1 h later, the decellularized AF sample was turned over and another 100 μl cell suspension was seeded onto the surface. The cell-containing constructs were incubated for 2 h before the culture medium was added. Culture medium was changed every 2 days.

7.2.5.3 Cell Distribution and Viability Assessment. After 7 days culture, the viability of cells seeded into scaffolds was detected by a Live/Dead fluorescence assay kit (Biotium Kit # 30002, Fremont, CA, USA), which included ethidium homodimer III (EthD-III) as the “dead” dye and Calcein AM as the “live” dye. The manufacturer’s protocol was followed for the Live/Dead assay. Briefly, 5 μL of 4 mM Calcein AM and 20 mL of 2 mM EthD-III was added to 10 mL PBS. Samples were incubated in this PBS and dye solution. Imaging was performed using a Thorlabs Confocal Microscopy Upgrade (Newton, NJ, USA) attached to an Olympus IX-73 microscope (Tokyo, Japan). Image processing and analysis was performed using Fiji/ImageJ2 [275].

7.3 Results

7.3.1 Quantification of DNA and GAG

There was a reduction in the mean total DNA content in all the decellularized AF, compared to the cellular control. The mean total DNA content in all decellularized tissue constructs was below 50 ng $*mg^{-1}$ dry weight ($p < 0.001$) (Figure 35A).

The normalized GAG content was lower in decellularized than control AF samples ($p<0.05$) The GAG content in PEF-decellularized samples was closest to that in natural AF, and higher than that in the detergent-decellularized samples ($p<0.05$) (Figure 35B). The GAG content was lower in samples treated with SDS and Triton X-100 ($p<0.05$).

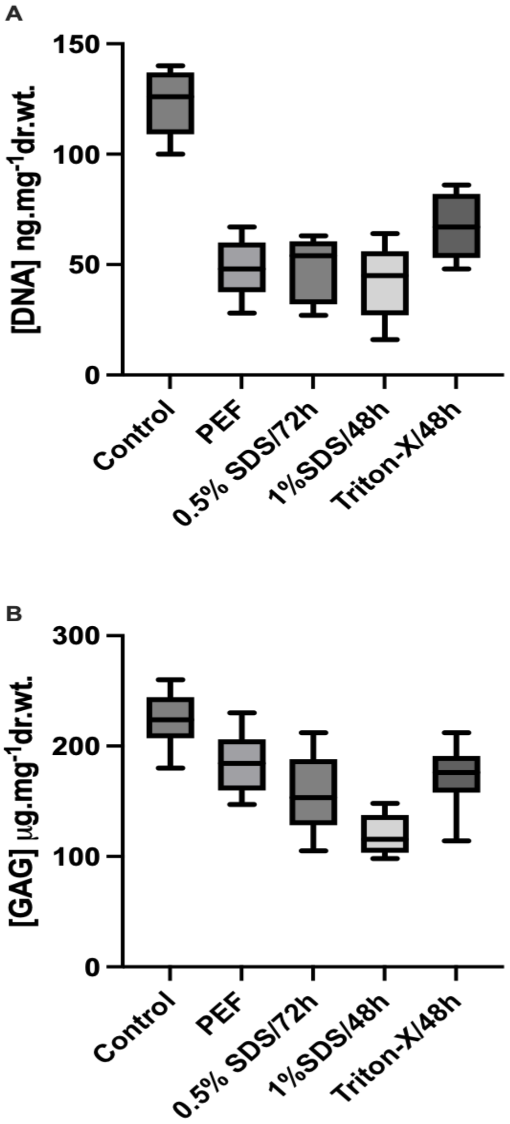

Figure 35. Mean Total DNA Content in Dry Decellularized Bovine AF Tissue (A) and Mean Total GAG Content in Dry Decellularized Bovine AF Tissue (B)

7.3.2 SEM and Histology

Macroscopically, after decellularization, AF tissue swelled, and the central voids became smaller as compared with natural AF. The decellularization groups did not differ macroscopically. In control samples, collagen fibers were arranged orderly, with a concentric lamellar structure. Treated samples showed a concentric lamellar structure, with no difference from natural AF, and the arrangement of collagen fibers was the same when compared to the native AF tissue as shown in Figure 36 below.

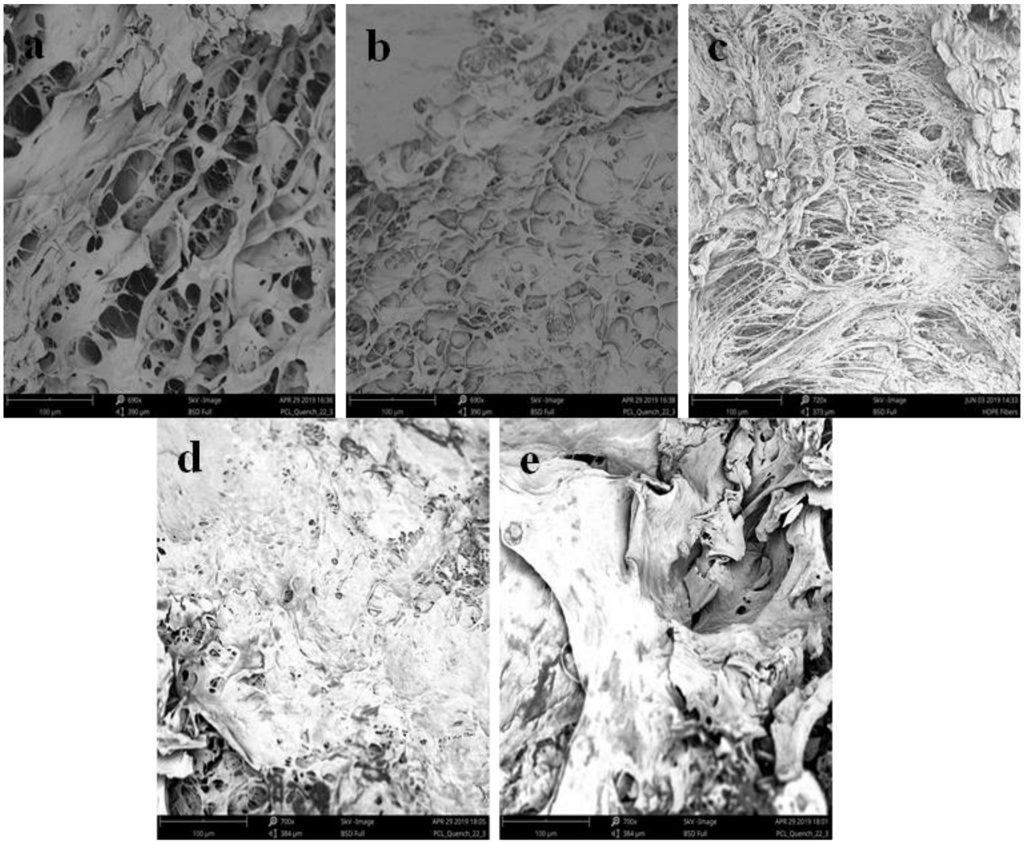

Figure 36. Scanning Electron Microscopy Images of Native Bovine AF Tissue. (a) and decellularized constructs (b -e). (b) AF tissue decellularized with PEF, (c) AF tissue decellularized with 0.5% SDS for 72 h, (d) AF tissue decellularized with 1% SDS for 48 h and (e) AF tissue decellularized with 3% Triton-X100

In H&E staining shown in Figure 37, control AF samples showed many cells scattered among collagen fibers, which were compact with an ordered arrangement. Decellularized PEF, Triton X-100 and SDS-treated samples showed no cells, and the mesh of collagen fibers was looser in Triton X-100 and SDS samples than in PEF-treated and control samples. PEF-treated samples retained the concentric lamellar arrangements of collagen, similar to natural AF. Safranin O staining showed that both natural AF and decellularized AF were rich in proteoglycans, but staining was less dense in detergent-decellularized samples than PEF decellularized and natural AF samples (Figure 38). Proteoglycan content may have decreased during the decellularization process with detergents. Sirius red staining showed enriched collagen content in both natural and all decellularized AF constructs, as shown in Figure 39.

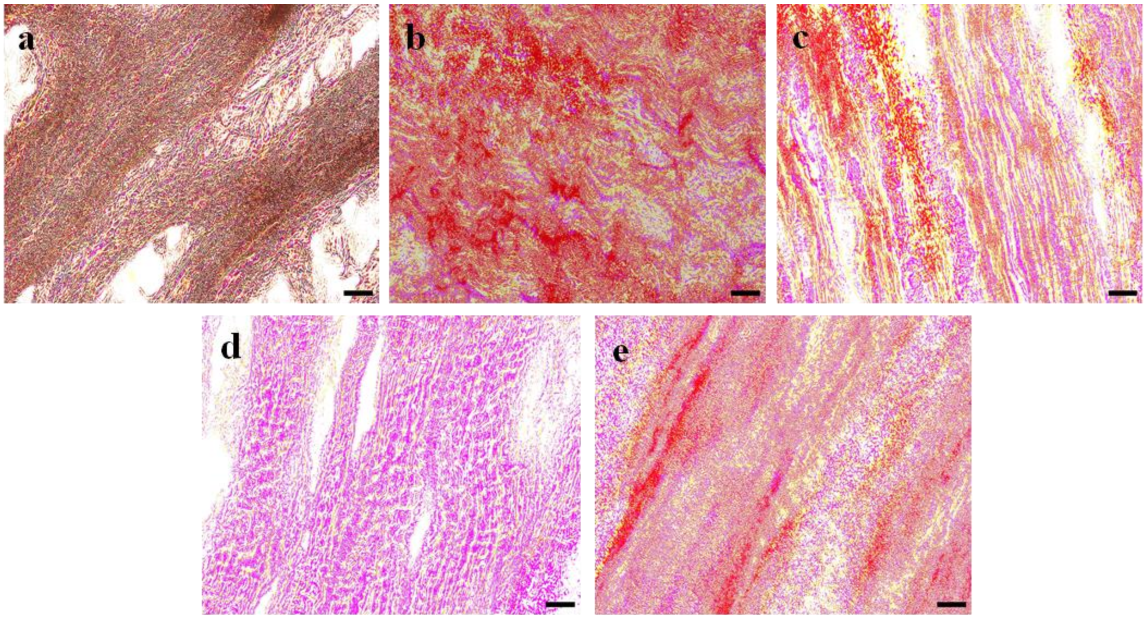

Figure 37. Images of H&E-Stained Native Bovine AF Tissue. (a) and decellularized bovine AF tissue (b – e). (b) AF tissue decellularized with PEF, (c) AF tissue decellularized with 0.5% SDS for 72 h, (d) AF tissue decellularized with 1% SDS for 48 h and (e) AF tissue decellularized with 3% Triton-X100. All images toke at 20X magnification with 100 μm scale bars

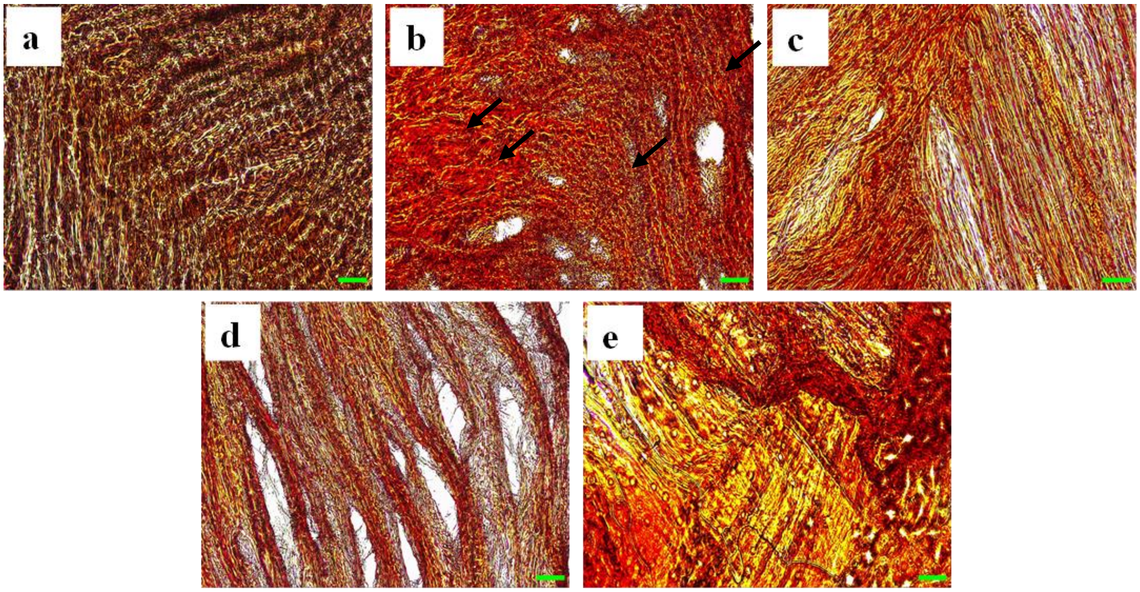

*Figure 38***.** Safranin O Staining of Cross-Section of Bovine AF Tissue for GAG Distribution. (a) Control, (b) PEF, (c) 0.5% SDS, (d) 1% SDS, (e) 3% Triton X-100. Scale bar: 100 μm

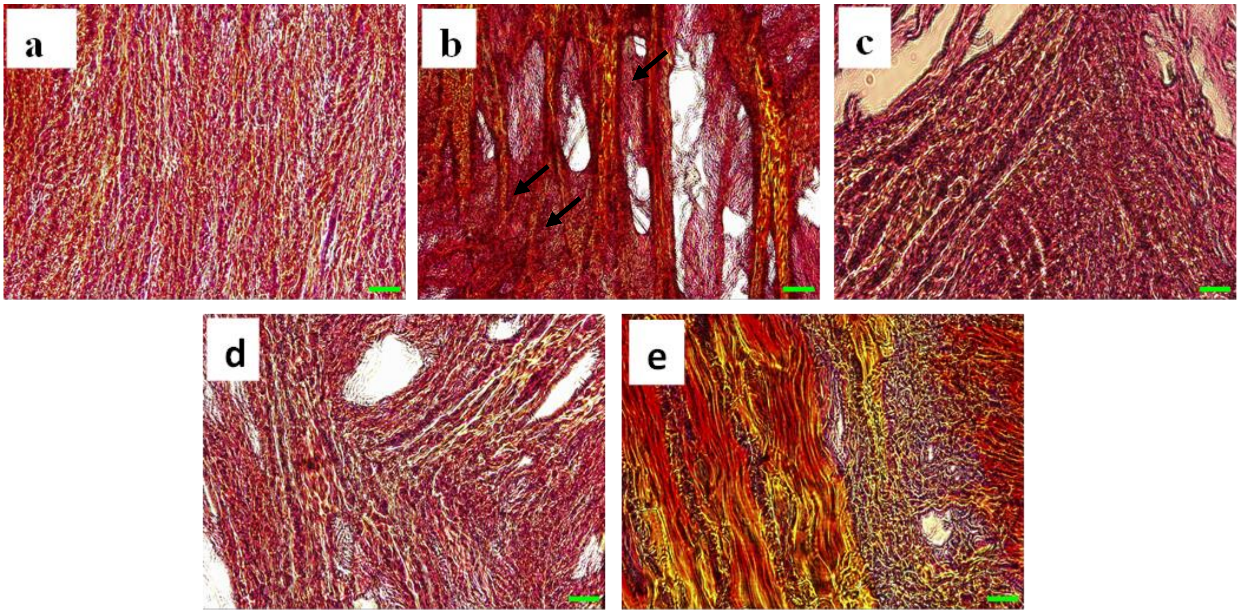

Figure 39. Sirius Red Staining of Cross-Section of Bovine AF Tissue for GAG Distribution. (a) Control, (b) PEF, (c) 0.5% SDS, (d) 1% SDS, (e) 3% Triton X-100. Scale bar: 100 μm

7.4 Discussion

We have investigated short intense µsPEF fields for cell ablation and longer msPEF for extraction to decellularize bovine AF. The histological structure and biochemical properties of the PEF-decellularized AF scaffold are compared to those of AF scaffolds decellularized with ionic detergents SDS and Triton X-100. PEF-decellularized AF tissue retains the major ECM components after thorough cell removal, preserves the concentric lamellar structure and tensile mechanical properties, and possesses favorable biocompatibility. Therefore, PEF it is a suitable candidate for processing scaffold material for AF tissue engineering.

Before using acellular matrices for tissue engineering, it is essential to eliminate their immunogenicity. The primary immunogenic factors in tissue are cells, which contain histocompatibility antigens (human leukocyte antigen) on their membrane surfaces as lipoproteins or glycoproteins. These antigens vary genetically among individuals and can trigger an immune response by recipient T cells, leading to rejection and inflammation after allogeneic cell transplantation. Therefore, to prevent immune rejection, inflammation, and potential transplant rejection, it is necessary to remove the cells from the extracellular matrix (ECM) before using it as a scaffold. Our histological analysis (H&E staining) demonstrates that PEF is as effective as the ionic detergents at removing cells. Previously, decellularization with SDS and Triton X-100 has been shown to completely eliminate nuclear material in many biological tissues. However, the efficacy of cell removal with these detergents remains controversial, as nuclear material was observed in some applications. The effectiveness of detergents in decellularization depends on the material's ultrastructural organization, and the concentration of detergents also influences the efficiency of decellularization. In a recent study by Chan et al., bovine intervertebral discs are decellularized using 0.1% SDS to create a natural intervertebral disc scaffold, but many dead cells remain according to Live/Dead staining. In contrast, our study shows that PEF decellularization results in no cells remaining comparable to 0.5% and 1% SDS in the decellularized AF ECM.

Collagen and GAGs are the primary constituents of the AF ECM. They play a crucial role in facilitating cellular attachment, survival, migration, proliferation, and differentiation. An ideal decellularized AF ECM should have collagen and GAG levels similar to those found in the natural AF. Our analysis reveals no difference in collagen content between the decellularized AF and control samples, indicating that there was no loss of collagen during the decellularization process using PEF, Triton X-100 or SDS. However, the decellularization did lead to a reduction in GAG content, especially when detergents were used, whereas PEF treatment results in GAG levels closest to those of the control samples. The preservation of collagen and the loss of GAG may be attributed to their relative distribution within and between the lamellae. The proteoglycan-rich ground substance surrounds the orderly arranged collagen fibers, and this matrix, containing abundant proteoglycans and GAG, is more susceptible to the decellularization solution and therefore more likely to be lost during the decellularization process compared to collagen.

The AF, which is shaped like a ring composed of multiple layers of fibro-cartilaginous tissue, possesses a unique angle-ply architecture that is crucial for withstanding various physiological loads in the spine for normal functioning. Upon decellularization, examination though H&E staining and SEM reveals that the concentric lamellar structure remains well-preserved following PEF processing However, when

Triton X-100 is employed, the concentric lamellar structure shows slight disturbances, and some collagen fractures are observed in the H&E staining. In contrast, SDS causes severe destruction of the concentric lamellar structure, resulting in significant gaps between collagen fibers, as observed in both the H&E staining and SEM images. These findings align with the documented effects of SDS treatment. SDS, an anionic detergent with a negatively charged head-group, has the ability to bind and denature soluble and membrane-bound proteins. It disrupts non-covalent bonds within proteins, leading to the loss of their native conformation.

The biocompatibility of treated samples, a crucial characteristic of decellularized scaffolds in tissue engineering, has been assessed in our study. During the decellularization process, various chemicals such as EDTA, RNase A, and DNase I are utilized. It is important to ensure that these chemicals are completely removed from the tissue, as their presence post-decellularization could be toxic to host cells upon implantation of the scaffold in vivo. To address this concern, we have performed thorough washing of the specimens in PBS following decellularization to eliminate any remaining agents. Subsequently, we reseed the matrices with isolated bovine AF cells and evaluate the toxicity of the scaffolds using Live/Dead staining. The Live/Dead staining reveals the absence of dead cells, further confirming the non-cytotoxic nature of the PEF decellularized scaffolds (Figure 40).

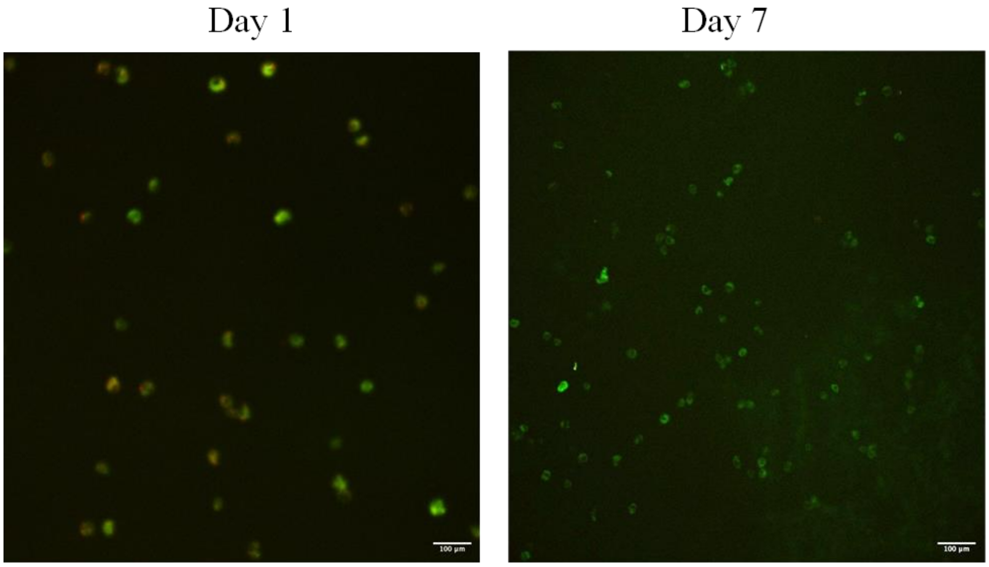

Figure 40. Confocal Fluorescence Images of AF Cells Seeded In PEF- Decellularized AF Tissue Scaffolds. Green Fluorescence of Calcein Indicates Living Cells

7.5 Conclusion

This study demonstrates the feasibility of using PEF as a tissue engineering tool to decellularize bovine AF matrices to create native scaffolds. The ECM of PEF-treated constructs compare favorably to native AF tissue and in some regards are better than constructs decellularized using SDS or Triton X-100. The PEF-decellularized scaffolds have been tested for cell removal efficiency, preservation of matrix components, microstructure, and cytotoxicity. We conclude from our findings that PEF processing fulfills the two main of a requirements xenograft, acellularity and high susceptibility to recellularization with AF cells. An in vivo study is still needed to determine whether such novel scaffolds have potential for IVD tissue engineering implantation.

Chapter 8

Conclusions

8.1 Summary

Severe back injuries and chonic pain require surgical replacement of damaged intervertebral disc (IVD) cartilage at later stages of disease. Several types of artificial implants have been developed, but each fall short in replicating native cartilage tissue. I have been developing an electrochemical method for quick and efficient preparation of a natural replacement made from bovine cartilage. Animal tissue like this is more readily available and easier to source. Exposure of bovine IVD tissue to an upper theshold pulsed electric field (PEF) dose kills the bovine cells without causing thermal damage to the tissue, and successive PEF exposures at lower magnitudes accelerates removal of immunogenic biomolecules via electrophoresis, combined with controlled perfusion of optimized aqueous solutions. This approach results in a natural scaffold ready for verifying biocompatibility and mechanical strength. My initial efforts have characterized the effects of microsecond pulsed electric fields (μsPEF) on primary bovine AF fibroblast-like cells in vitro. The AF primary cells are isolated from fresh bovine IVDs and cultured to confluence in culture medium. The cells have been exposed to PEFs of 10 and 100 μs durations with different numbers of pulses and applied electric field strengths. Experiments have determined the optimal PEF parameters for inducing cell death by non-thermal irreversible electroporation. Next, I have established low-intensity and minimally heating PEF-induced electrokinetic flow for molecular extraction by determining the electrophoretic mobility of charged molecules within the AF cartilage tissue. Finally, a biocompatible AF scaffold has been produced using PEF and electrolyte solutions in a custom-designed bioreactor. PEF application achieves decellularization of cartilage tissue in a matter of 3 h compared chemical methods that take days, while conserving the desired biomolecules and ultrastructure of the tissue matrix.

8.2 Novel Contributions

This thesis presents several novel contributions to the field of tissue engineering and electrokinetic transport, focusing on the optimization of Pulsed Electric Fields (PEF) for various biomedical applications. To begin with, the thesis demonstrates significant advancements in enhancing the proliferation and migration rates of fibroblast-like AF primary cells using 10 µs PEF. By meticulously optimizing PEF parameters, the study achieved a notable increase in cell proliferation (25-30%) and migration rates (30-40%). These improvements are attributed to the more efficient nutrient uptake and signaling due to membrane permeabilization, underscoring the potential of PEF in cellular engineering.

The application of Electrochemical Impedance Spectroscopy (EIS) for measuring physiological changes in AF cartilage represents another key contribution. The thesis details the development of EIS techniques capable of detecting subtle changes (as little as 10%) in the electrical properties of cartilage, providing a valuable tool for diagnosing early stages of degeneration or assessing the efficacy of tissue repair strategies. A crucial part of the research also involved determining the extent of electropermeabilization in AF cartilage tissue following PEF exposure. By employing EIS, the thesis offers novel methodologies for quantifying specific changes in electrical properties, providing insights into the effects of PEF on tissue properties.

Additionally, the thesis addresses the challenge of reducing Joule heating in electrokinetic transport across bovine cartilage using PEF. The research successfully reduced Joule heating by up to 50-60%, enhancing the efficiency of transport processes and presenting a significant leap in electrokinetic transport methodologies. The creation of an acellular bovine AF tissue scaffold using a combination of µsPEF and msPEF marks a significant advancement in tissue scaffolding. The optimized scaffold, with its balance in pore size and mechanical strength, showed a 30-40% improvement in tissue compatibility, highlighting the potential of PEF in scaffold engineering.

Furthermore, the thesis includes the development of a novel method for the decellularization of a biocompatible xenograft for annular repair. By using µsPEF and msPEF, the study achieved over 90% cell removal while maintaining structural integrity, leading to a 20-30% improvement in graft integration, a significant contribution to regenerative medicine.

Finally, the fabrication of a bioreactor for the decellularization of biological tissues using a combination of PEF and perfusion is a noteworthy engineering feat. This bioreactor design has led to a 40-50% increase in decellularization efficiency and a 20-30% reduction in processing time, setting a new standard in tissue decellularization technologies.

Overall, these contributions not only present significant advancements in the understanding and application of PEF in biomedical engineering but also open up new avenues for future research and potential clinical applications.

8.3 Future Work and Recommendations

The ex vivo decellularization of scaffold and conducting in vitro research to evaluate the biocompatibility of the scaffold has been successful. However, to translate these findings into clinical applications, rigorous in vivo animal studies are crucial to assess their safety, efficacy, and host tissue integration. While significant progress has been made in the in vitro characterization of the scaffold, in vivo animal studies play a pivotal role in bridging the gap between preclinical research and clinical translation. These studies provide a comprehensive understanding of the scaffold-host interactions, tissue integration, and functional outcomes.

Choosing appropriate animal models is a critical aspect of designing in vivo studies for decellularized TESs. Considerations include selecting species that closely resemble human physiology and possess relevant tissue properties. While no animal model can perfectly replicate the complexity of human biology, careful selection can offer valuable insights into the scaffold's performance and potential adverse effects. Commonly used animal models, such as rodents, pigs, and non-human primates, are often chosen based on their physiological similarities to humans and the tissue of interest.

The study design is essential for generating reliable and reproducible data. Clearly defining research objectives and outcomes is crucial to guide the experimental approach. Additionally, sample size estimation and statistical analysis should be performed to ensure adequate statistical power. Ethical considerations and compliance with regulatory guidelines must be prioritized to ensure the welfare of the animals and adherence to ethical principles. In vivo studies focusing on decellularized tissue-engineered scaffolds (TESs) will significantly benefit from advancements in surgical implantation techniques. Future experiments should incorporate the use of biopsied, decellularized scaffolds, both with and without seeded annulus fibrosus (AF) cells, reintegrated into the disc specimen. Conducting comprehensive whole disc cultures will be crucial to evaluate the scaffold's integration and functionality within a more intricate tissue system. Attention must be paid to the surgical approach, especially considering the specific tissue targets and the desired functional outcomes. The handling and fixation of the scaffold during implantation need to be meticulously managed to ensure optimal integration and reduce the likelihood of post-surgical complications. Furthermore, exploring minimally invasive techniques could be a pivotal area of research. Such methods would likely decrease surgical trauma and promote quicker recovery, benefiting both the research efficacy and animal welfare.

Observing Immunogenic Factors and MSC Interaction with Bovine AF Scaffolds: A detailed examination of how mesenchymal stem cells (MSCs) interact with these scaffolds is essential to gain deeper insights into cellular responses and the potential for tissue regeneration. Additionally, the assessment of biocompatibility and immunogenicity is crucial to better understand the host response to the scaffold. Conducting histological analyses will be instrumental in evaluating tissue integration, remodeling, and identifying any signs of inflammation or foreign body reactions. Furthermore, investigating the mechanical properties and stability of the scaffold is vital for understanding its long-term durability and functionality. To comprehensively assess the efficacy of the scaffold in tissue restoration, functional assessments should be carried out. These could include measuring the extent of tissue regeneration and monitoring functional recovery post-implementation. Such investigations would provide valuable data on the scaffold's performance and its potential application in clinical settings.

Observing Regeneration of ECM between Allograft and Host Tissue: To ensure the effective and safe implementation of decellularized Tissue Engineering Scaffolds (TESs) in clinical settings, it is crucial to conduct long-term follow-up studies. These studies are essential for evaluating the durability and longevity of these scaffolds. A key aspect of this research should focus on observing the regeneration of the extracellular matrix (ECM) between the allograft and host tissue. For a thorough assessment, employing advanced imaging techniques and molecular analysis is recommended. Non-invasive imaging modalities will be instrumental in visualizing the scaffold's integration within the host tissue over extended periods. Concurrently, molecular analysis should be employed to gain insights into the cellular interactions, signaling pathways, and the overall tissue remodeling processes that occur post-implantation. Integrating the data from both imaging and molecular studies will provide a comprehensive understanding of the scaffold's performance. This approach will not only shed light on the biocompatibility and functional integration of the TESs but also help in monitoring potential adverse effects or complications that may arise over time. The insights gained from these long-term studies will be invaluable in refining the design and application of TESs, ultimately leading to improved outcomes in tissue engineering and regenerative medicine.

References

1. Butler, R. J., Marchesi, S., Royer, T. & Davis, I. S. The Effect of a Subject-Specific Amount of Lateral Wedge on Knee. *J. Orthop. Res. Sept.* **25**, 1121–1127 (2007).

2. Kazezian, Z. *et al.* Gene Expression Profiling Identifies Interferon Signalling Molecules and IGFBP3 in Human Degenerative Annulus Fibrosus. *Scientific Reports* vol. 5 (2015).

3. Xu, H. *et al.* Comparison of Decellularization Protocols for Preparing a Decellularized Porcine Annulus Fibrosus Scaffold. **9**, 1–13 (2014).

4. Torre, O. M., Mroz, V., Bartelstein, M. K., Huang, A. H. & Iatridis, J. C. Annulus fibrosus cell phenotypes in homeostasis and injury: implications for regenerative strategies. *Ann. N. Y. Acad. Sci.* **1442**, 61–78 (2019).

5. Fernandez, C., Marionneaux, A., Gill, S. & Mercuri, J. Biomimetic nucleus pulposus scaffold created from bovine caudal intervertebral disc tissue utilizing an optimal decellularization procedure. *J. Biomed. Mater. Res. - Part A* **104**, 3093–3106 (2016).

6. Hestbaek, L. *et al.* The course of low back pain in a general population. Results from a 5-year prospective study. *J. Manipulative Physiol. Ther.* **26**, 213–219 (2003).

7. Park, C. K. Total disc replacement in lumbar degenerative disc diseases. *J. Korean Neurosurg. Soc.* **58**, 401–411 (2015).

8. Gilpin, A. & Yang, Y. Decellularization Strategies for Regenerative Medicine: From Processing Techniques to Applications. *Biomed Res. Int.* **2017**, (2017).

9. Davalos, R. V. Irreversible Electroporation to Create Tissue Scaffolds. vol. 2 (2017).

10. Buchmann, L., Bloch, R. & Mathys, A. Comprehensive pulsed electric field (PEF) system analysis for microalgae processing. *Bioresour. Technol.* **265**, 268–274 (2018).

11. Zhu, N. *et al.* Design of a treatment chamber for low-voltage pulsed electric field sterilization. *Innov. Food Sci. Emerg. Technol.* **42**, 180–189 (2017).

12. Ohshima, T., Tanino, T., Kameda, T. & Harashima, H. Engineering of operation condition in milk pasteurization with PEF treatment. *Food Control* **68**, 297–302 (2016).

13. Leong, S. Y., Richter, L. K., Knorr, D. & Oey, I. Feasibility of using pulsed electric field processing to inactivate enzymes and reduce the cutting force of carrot (Daucus carota var. Nantes). *Innov. Food Sci. Emerg. Technol.* **26**, 159–167 (2014).

14. Bansal, V., Sharma, A., Ghanshyam, C., Singla, M. L. & Kim, K. H. Influence of pulsed electric field and heat treatment on Emblica officinalis juice inoculated with Zygosaccharomyces bailii. *Food Bioprod. Process.* **95**, 146–154 (2015).

15. Milani, E. A., Alkhafaji, S. & Silva, F. V. M. Pulsed Electric Field continuous pasteurization of different types of beers. *Food Control* **50**, 223–229 (2015).

16. Huang, K. & Wang, J. Designs of pulsed electric fields treatment chambers for liquid foods pasteurization process: A review. *J. Food Eng.* **95**, 227–239 (2009).

17. Shams, S. & Patel, C. B. Anti-cancer mechanisms of action of therapeutic alternating electric fields (tumor treating fields [TTFields]). *J. Mol. Cell Biol.* **14**, 1–16 (2022).

18. Ballash, G. A. *et al.* Pulsed electric field application reduces carbapenem- and colistin-resistant microbiota and blaKPC spread in urban wastewater. *J. Environ. Manage.* **265**, (2020).

19. Mousazadeh, M. *et al.* A critical review on the existing wastewater treatment methods in the COVID-19 era: What is the potential of advanced oxidation processes in combatting viral especially SARS-CoV-2? *J. Water Process Eng.* **49**, (2022).

20. Golberg, A. *et al.* Energy-efficient biomass processing with pulsed electric fields for bioeconomy and sustainable development. *Biotechnol. Biofuels* **9**, 1–22 (2016).

21. Puértolas, E., López, N., Condón, S., Raso, J. & Álvarez, I. Pulsed electric fields inactivation of wine spoilage yeast and bacteria. *Int. J. Food Microbiol.* **130**, 49–55 (2009).

22. Ranjha, M. M. A. N. *et al.* A critical review on pulsed electric field: A novel technology for the extraction of phytoconstituents. *Molecules* **26**, 1–23 (2021).

23. Donsì, F., Ferrari, G. & Pataro, G. Applications of pulsed electric field treatments for the enhancement of mass transfer from vegetable tissue. *Food Eng. Rev.* **2**, 109–130 (2010).

24. Golberg, A. *et al.* Skin rejuvenation with non-invasive pulsed electric fields. *Sci. Rep.* **5**, 1–18 (2015).

25. Sundelacruz, S. & Kaplan, D. L. Stem cell- and scaffold-based tissue engineering approaches to osteochondral regenerative medicine. *Semin. Cell Dev. Biol.* **20**, 646–655 (2009).

26. Sundelacruz, S., Levin, M. & Kaplan, D. L. Role of membrane potential in the regulation of cell proliferation and differentiation. *Stem Cell Rev. Reports* **5**, 231–246 (2009).

27. Tapias, L. F. & Ott, H. C. Decellularized scaffolds as a platform for bioengineered organs. *Curr. Opin. Organ Transplant.* **19**, 145–152 (2014).

28. Yuan, X., Arkonac, D. E., Chao, P. H. G. & Vunjak-Novakovic, G. Electrical stimulation enhances cell migration and integrative repair in the meniscus. *Sci. Rep.* **4**, 1–12 (2015).

29. Chalidis, B., Sachinis, N., Assiotis, A. & Maccauro, G. Stimulation of bone formation and fracture healing with pulsed electromagnetic fields: biologic responses and clinical implications. *Int. J. Immunopathol. Pharmacol.* **24**, 17–20 (2011).

30. Iwasa, K. & Reddi, A. H. Pulsed Electromagnetic Fields and Tissue Engineering of the Joints. *Tissue Eng. - Part B Rev.* **24**, 144–154 (2018).

31. HOLLINSHEAD, W. H. Anatomy of the Spine. *J. Bone Jt. Surg.* **47**, 209–215 (1965).

32. Spinal Anatomy. *Spinal Anat.* 7–14 (2020) doi:10.1007/978-3-030-20925-4.

33. Mathis, J. M. Ch 2 Spine Anatomy. *Percutaneous Vertebroplasty and Kyphoplasty* 8–32 (2006).

34. Scalon, V. C. & Sanders, T. *Essentials of Anatomy and Physiology*. (F. A. Davis Company, 2007).

35. Lumbal vertebrae (L1-L5). https://www.anatomystandard.com/Columna_Vertebralis/Vertebrae_Lumbales/Typical_Lumbar.html.

36. Illien-jünger, S., Walter, B. A., Mayer, J. E., Hecht, A. C. & Iatridis, J. C. and Their Applications to Study Pathogenesis and Repair. doi:10.1007/978-3-7091-1535-0.

37. Bron, J. L., Van Der Veen, A. J., Helder, M. N., Van Royen, B. J. & Smit, T. H. Biomechanical and in vivo evaluation of experimental closure devices of the annulus fibrosus designed for a goat nucleus replacement model. *Eur. Spine J.* **19**, 1347–1355 (2010).

38. Long, R. G., Torre, O. M., Hom, W. W., Assael, D. J. & Iatridis, J. C. Design requirements for annulus fibrosus repair: Review of forces, displacements, and material properties of the intervertebral disk and a summary of candidate hydrogels for repair. *J. Biomech. Eng.* **138**, (2016).

39. Yang, C. H. *et al.* The effect of annular repair on the failure strength of the porcine lumbar disc after needle puncture and punch injury. *Eur. Spine J.* **25**, 906–912 (2016).

40. Jin, L., Shimmer, A. L. & Li, X. The challenge and advancement of annulus fibrosus tissue engineering. 1090–1100 (2013) doi:10.1007/s00586-013-2663-2.

41. Heuer, F., Ulrich, S., Claes, L. & Wilke, H. J. Biomechanical evaluation of conventional anulus fibrosus closure methods required for nucleus replacement: Laboratory investigation. *J. Neurosurg. Spine* **9**, 307–313 (2008).

42. Sedaghatpour, D. D., Laudier, D. M., Hecht, A. C., Qureshi, S. A. & Iatridis, J. C. Development of a Bovine Decellularized Extracellular Matrix-Biomaterial for Nucleus Pulposus Regeneration. 876–888 (2016) doi:10.1002/jor.23088.

43. Wilke, H. J., Heuer, F., Neidlinger-Wilke, C. & Claes, L. Is a collagen scaffold for a tissue engineered nucleus replacement capable of restoring disc height and stability in an animal model? *Eur. Spine J.* **15**, (2006).

44. Fu, L. jie *et al.* Effect of a New Annular Incision on Biomechanical Properties of the Intervertebral Disc. *Orthop. Surg.* **8**, 68–74 (2016).

45. Rickers, K., Bendtsen, M., Le, D. Q. S., Veen, A. J. der & Bünger, C. E. Biomechanical evaluation of annulus fibrosus repair with scaffold and soft anchors in an ex vivo porcine model. *Sicot-J* **4**, 38 (2018).

46. Baldit, A. *et al.* Annulus fibrosus microstructure : an explanation to local heterogeneities To cite this version : HAL Id : hal-01219449. (2015).

47. Mengoni, M. *et al.* Derivation of inter-lamellar behaviour of the intervertebral disc annulus. *J. Mech. Behav. Biomed. Mater.* **48**, 164–172 (2015).

48. Tavakoli, J., Elliott, D. M. & Costi, J. J. Structure and mechanical function of the inter-lamellar matrix of the annulus fibrosus in the disc. *J. Orthop. Res.* **34**, 1307–1315 (2016).

49. Vergari, C. *et al.* Bovine and degenerated human annulus fibrosus: a microstructural and micromechanical comparison. *Biomech. Model. Mechanobiol.* **16**, 1475–1484 (2017).

50. Ambard, D. & Cherblanc, F. Mechanical behavior of annulus fibrosus: A microstructural model of fibers reorientation. *Ann. Biomed. Eng.* **37**, 2256–2265 (2009).

51. Urban, J. P. G. & Roberts, S. Degeneration of the intervertebral disc. **5**, (2003).

52. Keyes, Donald C.; Compere, E. L. THE NORMAL AND PATHOLOGICAL PHYSIOLOGY OF THE NUCLEUS PULPOS... : JBJS.

53. Setton, L. A. & Chen, J. Mechanobiology of the Intervertebral Disc and Relevance to Disc Degeneration. *J. Bone Jt. Surg.* **88**, 52–57 (2006).

54. Detiger, S. E. L. *et al.* Translational challenges for the development of a novel nucleus pulposus substitute: Experimental results from biomechanical and in vivo studies. *J. Biomater. Appl.* **30**, 983–994 (2016).

55. Collin, E. C. *et al.* Unique glycosignature for intervertebral disc and articular cartilage cells and tissues in immaturity and maturity. *Sci. Rep.* **6**, 1–12 (2016).

56. Newell, N., Carpanen, D., Evans, J. H., Pearcy, M. J. & Masouros, S. D. Mechanical Function of the Nucleus Pulposus of the Intervertebral Disc under High Rates of Loading. *Spine (Phila. Pa. 1976).* **44**, 1035–1041 (2019).

57. Hwang, P. Y., Chen, J., Jing, L., Hoffman, B. D. & Setton, L. A. The role of extracellular matrix elasticity and composition in regulating the nucleus pulposus cell phenotype in the intervertebral disc: A narrative review. *J. Biomech. Eng.* **136**, 1–10 (2014).

58. Schmitz, T. C. *et al.* Characterization of biomaterials intended for use in the nucleus pulposus of degenerated intervertebral discs. *Acta Biomater.* **114**, 1–15 (2020).

59. Alexander, L. A., Hancock, E., Agouris, I., Smith, F. W. & MacSween, A. The response of the nucleus pulposus of the lumbar intervertebral discs to functionally loaded positions. *Spine (Phila. Pa. 1976).* **32**, 1508–1512 (2007).

60. McGuire, R. M. The Development of a Biomimetic Patch for Annulus Fibrosus Repair. (Clemson University In, 2015).

61. Scheibler, A. G. *et al.* Feasibility of the annulus fibrosus repair with in situ gelating hydrogels – A biomechanical study. *PLoS One* **13**, 1–15 (2018).

62. Christiani, T. R., Baroncini, E., Stanzione, J. & Vernengo, A. J. In vitro evaluation of 3D printed polycaprolactone scaffolds with angle-ply architecture for annulus fibrosus tissue engineering. *Regen. Biomater.* **6**, 175–184 (2019).

63. Rickers, K., Bendtsen, M., Le, D. Q. S., Veen, A. J. Der & Bünger, C. E. Biomechanical evaluation of annulus fibrosus repair with scaffold and soft anchors in an ex vivo porcine model. *Sicot-J* **4**, 0–5 (2018).

64. Long, R. G., Torre, O. M., Hom, W. W., Assael, D. J. & Iatridis, J. C. Design requirements for annulus fibrosus repair: Review of forces, displacements, and material properties of the intervertebral disk and a summary of candidate hydrogels for repair. *J. Biomech. Eng.* **138**, 1–14 (2016).

65. Tavakoli, J. & Costi, J. J. Ultrastructural organization of elastic fibres in the partition boundaries of the annulus fibrosus within the intervertebral disc. *Acta Biomater.* **68**, 67–77 (2018).

66. Isaacs, J. L. Micromechanics of the Annulus Fibrosus: Role of Biomolecules in Mechanical Function. (Drexel University, 2012).

67. Wei, Z. *et al.* Comprehensive assessment of in vivo lumbar spine intervertebral discs using a 3D adiabatic T1ρ prepared ultrashort echo time (UTE-Adiab-T1ρ) pulse sequence. *Quant. Imaging Med. Surg.* **12**, 269–280 (2022).

68. Xiao, L. *et al.* Molecular Detection and Assessment of Intervertebral Disc Degeneration via a Collagen Hybridizing Peptide. *ACS Biomater. Sci. Eng.* **5**, 1661–1667 (2019).

69. Kayalioglu, G. *The Vertebral Column and Spinal Meninges*. *The Spinal Cord* (Elsevier Ltd, 2009). doi:10.1016/B978-0-12-374247-6.50007-9.

70. Chen, W. H. *et al.* Intervertebral disc regeneration in an ex vivo culture system using mesenchymal stem cells and platelet-rich plasma. *Biomaterials* **30**, 5523–5533 (2009).

71. Raastad, J., Reiman, M., Coeytaux, R., Ledbetter, L. & Goode, A. P. The association between lumbar spine radiographic features and low back pain: A systematic review and meta-analysis. *Semin. Arthritis Rheum.* **44**, 571–585 (2015).

72. Passias, P. G. *et al.* Segmental lumbar rotation in patients with discogenic low back pain during functional weight-bearing activities. *J. Bone Jt. Surg.* **93**, 29–37 (2011).

73. Sung, B. & Kim, M. H. Liquid-crystalline nanoarchitectures for tissue engineering. *Beilstein J. Nanotechnol.* **9**, 205–215 (2018).

74. MacLean, J. J., Roughley, P. J., Monsey, R. D., Alini, M. & Iatridis, J. C. In vivo intervertebral disc remodeling: Kinetics of mRNA expression in response to a single loading event. *J. Orthop. Res.* **26**, 579–588 (2008).

75. Adam, C., Rouch, P. & Skalli, W. Inter-lamellar shear resistance confers compressive stiffness in the intervertebral disc: An image-based modelling study on the bovine caudal disc. *J. Biomech.* **48**, 4303–4308 (2015).

76. McDonnell, E. E. & Buckley, C. T. Investigating the physiological relevance of ex vivo disc organ culture nutrient microenvironments using in silico modeling and experimental validation. *JOR Spine* **4**, 1–16 (2021).

77. Deng, R. *et al.* Mechanical stimulation promotes MSCs healing the lesion of intervertebral disc annulus fibrosus. *Front. Bioeng. Biotechnol.* **11**, 1–11 (2023).

78. Maltseva, V. Effect of Pb exposure on the cells and matrix of the intervertebral disc of rats. *Regul. Mech. Biosyst.* **8**, 217–223 (2017).

79. Li, M. *et al.* Elastin Blends for Tissue Engineering Scaffolds. *J. Biomed. Mater. Res. Part A* **79**, 963–73 (2006).

80. Bhunia, B. K., Kaplan, D. L. & Mandal, B. B. Silk-based multilayered angle-ply annulus fibrosus construct to recapitulate form and function of the intervertebral disc. *Proc. Natl. Acad. Sci. U. S. A.* **115**, 477–482 (2018).

81. Ji, M. liang *et al.* Preclinical development of a microRNA-based therapy for intervertebral disc degeneration. *Nat. Commun.* **9**, 1–14 (2018).

82. Hodgkinson, T. *et al.* Regenerative response of degenerate human nucleus pulposus cells to GDF6 stimulation. *Int. J. Mol. Sci.* **21**, 1–14 (2020).

83. Ge, Y. *et al.* Pyroptosis and Intervertebral Disc Degeneration: Mechanistic Insights and Therapeutic Implications. *J. Inflamm. Res.* **15**, 5857–5871 (2022).

84. Chiou, S. Y., Hellyer, P. J., Sharp, D. J., Newbould, R. D. & Patel, M. C. Relationships between the integrity and function of lumbar nerve roots as assessed by diffusion tensor imaging and neurophysiology. 893–903 (2017) doi:10.1007/s00234-017-1869-0.

85. Liu, C. *et al.* Changes in resting-state functional connectivity in nonacute sciatica with acupuncture modulation : A preliminary study. doi:10.1002/brb3.1494.

86. Xin, L. *et al.* Minimal invasive annulotomy for induction of disc degeneration and implantation of poly (lactic-co-glycolic acid) (PLGA) plugs for annular repair in a rabbit model. *Eur. J. Med. Res.* **21**, 1–11 (2016).

87. Peng, Y. *et al.* Genipin-crosslinked decellularized annulus fibrosus hydrogels induces tissue-specific differentiation of bone mesenchymal stem cells and intervertebral disc regeneration. *J. Tissue Eng. Regen. Med.* **14**, 497–509 (2020).

88. Xin, L. *et al.* Effects of annulus defects and implantation of poly(lactic-co-glycolic acid) (PLGA)/fibrin gel scaffolds on nerves ingrowth in a rabbit model of annular injury disc degeneration. *J. Orthop. Surg. Res.* **12**, 1–11 (2017).

89. De Decker, S., Warner, A. S. & Volk, H. A. Prevalence and breed predisposition for thoracolumbar intervertebral disc disease in cats. *J. Feline Med. Surg.* **19**, 419–423 (2017).

90. Kague, E. *et al.* 3D assessment of intervertebral disc degeneration in zebrafish identifies changes in bone density that prime disc disease. *Bone Res.* **9**, 1–16 (2021).

91. Dickinson, P. J. & Bannasch, D. L. Current Understanding of the Genetics of Intervertebral Disc Degeneration. *Front. Vet. Sci.* **7**, 1–13 (2020).

92. Hanaei, S. *et al.* Association of IL10 and TGFB single nucleotide polymorphisms with intervertebral disc degeneration in Iranian population: A case control study. *BMC Med. Genet.* **19**, 1–10 (2018).

93. Jin, P. *et al.* Diabetes and intervertebral disc degeneration: A Mendelian randomization study. *Front. Endocrinol. (Lausanne).* **14**, 1–6 (2023).

94. Shao, Z. *et al.* RNA-binding protein HuR suppresses senescence through Atg7 mediated autophagy activation in diabetic intervertebral disc degeneration. *Cell Prolif.* **54**, 1–13 (2021).

95. Li, F. *et al.* Development and Validation of a Novel Nomogram to Predict the Risk of Intervertebral Disc Degeneration. *Mediators Inflamm.* **2022**, (2022).

96. Wang, C. *et al.* Magnetization transfer ratio mapping of intervertebral disc degeneration. *Magn. Reson. Med.* **64**, 1520–1528 (2010).

97. Zheng, Y. *et al.* Core-shell oxygen-releasing fibers for annulus fibrosus repair in the intervertebral disc of rats. *Mater. Today Bio* **18**, 100535 (2023).

98. Blanquer, S. B. G., Grijpma, D. W. & Poot, A. A. Delivery systems for the treatment of degenerated intervertebral discs. *Adv. Drug Deliv. Rev.* **84**, 172–187 (2015).

99. Li, B. *et al.* Engeletin Alleviates the Inflammation and Apoptosis in Intervertebral Disc Degeneration via Inhibiting the NF-κB and MAPK Pathways. *J. Inflamm. Res.* **15**, 5767–5783 (2022).

100. Rodeo, S. A., Monibi, F., Dehghani, B. & Maher, S. Biological and Mechanical Predictors of Meniscus Function: Basic Science to Clinical Translation. *J. Orthop. Res.* **38**, 937–945 (2020).

101. Liu, C. *et al.* The Upregulation of COX2 in Human Degenerated Nucleus Pulposus: The Association of Inflammation with Intervertebral Disc Degeneration. *Mediators Inflamm.* **2021**, (2021).

102. Meng, Z., Zheng, J., Fu, K., Kang, Y. & Wang, L. Curative Effect of Foraminal Endoscopic Surgery and Efficacy of the Wearable Lumbar Spine Protection Equipment in the Treatment of Lumbar Disc Herniation. *J. Healthc. Eng.* **2022**, (2022).

103. Ford, J., Hahne, A., Surkitt, L., Chan, A. & Richards, M. The evolving case supporting individualised physiotherapy for low back pain. *J. Clin. Med.* **8**, (2019).

104. Proks, P. *et al.* Vertebral formulae and congenital vertebral anomalies in guinea pigs: A retrospective radiographic study. *Animals* **11**, 1–15 (2021).

105. Shields, L. B. E., Iyer, V. G., Zhang, Y. P., Burger, J. T. & Shields, C. B. Parsonage-Turner Syndrome Following COVID-19 Vaccination: Clinical and Electromyographic Findings in 6 Patients. *Case Rep. Neurol.* 58–67 (2022) doi:10.1159/000521462.

106. Gu, J. & Xie, L. Significance of oxidative stress in the diagnosis and subtype classification of intervertebral disc degeneration. (2023).

107. Ibrahim, A. A. G. *et al.* Degenerative Disc Diseases: A Brief Review. *J. Pharm. Res. Int.* **33**, 282–286 (2021).

108. Rabin, M. L., Earnhardt, M. C., Patel, A., Ganihong, I. & Kurlan, R. Postural, Bone, and Joint Disorders in Parkinson's Disease. *Mov. Disord. Clin. Pract.* **3**, 538–547 (2016).

109. Mohamed Weheida, S., Elsayed Khatab, H., Abdel Mowla Ahmed Abdel Mowla, H. & Mohamed Mohamed, H. Effect of Applying an Educational Program on Knowledge and Self-Care Activities of Patients Undergoing Lumbar Discectomy. *Egypt. J. Heal. Care* **13**, 1334–1350 (2022).

110. DiStefano, T. J. *et al.* Development of a two-part biomaterial adhesive strategy for annulus fibrosus repair and ex vivo evaluation of implant herniation risk. *Biomaterials* **258**, 120309 (2020).

111. Liu, J. *et al.* Biomechanical properties of a novel nonfusion artificial vertebral body for anterior lumbar vertebra resection and internal fixation. *Sci. Rep.* **11**, 1–10 (2021).

112. Wang, F., Cheung, C. W. & Wong, S. S. C. Regenerative medicine for the treatment of chronic low back pain: a narrative review. *J. Int. Med. Res.* **51**, (2023).

113. Tekari, A., Chan, S. C. W., Sakai, D., Grad, S. & Gantenbein, B. Angiopoietin-1 receptor Tie2 distinguishes multipotent differentiation capability in bovine coccygeal nucleus pulposus cells. *Stem Cell Res. Ther.* **7**, 1–12 (2016).

114. Phan, K. *et al.* Primary Versus Revision Discectomy for Adults With Herniated Nucleus Pulposus: A Propensity Score–Matched Multicenter Study. *Glob. Spine J.* **8**, 810–815 (2018).

115. Alkosha, H. & Zidan, A. Early Outcome of Sciatica after Redo Surgeries for Recurrent Lumbar Disc Herniation. *Egypt. Spine J.* **9**, 19–26 (2014).

116. Shin, S. Its Association With Postoperative Spinal Infection. **24**, 20–24 (2016).

117. Muheremu, A. *et al.* Halo-pelvic traction for severe kyphotic deformity secondary to spinal tuberculosis. *Med. (United States)* **96**, 28–31 (2017).

118. Likhitpanichkul, M. *et al.* Fibrin-genipin adhesive hydrogel for annulus fibrosus repair: Performance evaluation with large animal organ culture, in situ biomechanics, and in vivo degradation tests. *Eur. Cells Mater.* **28**, 25–38 (2014).

119. Meisel, H. J. *et al.* Cell Therapy for Treatment of Intervertebral Disc Degeneration: A Systematic Review. *Glob. Spine J.* **9**, 39S-52S (2019).

120. Chen, S. *et al.* TGF-β signaling in intervertebral disc health and disease. *Osteoarthr. Cartil.* **27**, 1109–1117 (2019).

121. Zhang, H. *et al.* Stromal cell-derived factor-1 and its receptor CXCR4 are upregulated expression in degenerated intervertebral discs. *Int. J. Med. Sci.* **11**, 240–245 (2014).

122. Serigano, K. *et al.* Effect of cell number on mesenchymal stem cell transplantation in a canine disc degeneration model. *J. Orthop. Res.* **28**, 1267–1275 (2010).

123. van Hout, W. M. M. T., van der Molen, A. B. M., Breugem, C. C., Koole, R. & van Cann, E. M. Reconstruction of the alveolar cleft: Can growth factor-aided tissue engineering replace autologous bone grafting? A literature review and systematic review of results obtained with bone morphogenetic protein-2. *Clin. Oral Investig.* **15**, 297–303 (2011).

124. Moriguchi, Y. *et al.* Total disc replacement using tissue-engineered intervertebral discs in the canine cervical spine. *PLoS One* **12**, 1–18 (2017).

125. Xu, B. *et al.* Intervertebral disc tissue engineering with natural extracellular matrix-derived biphasic composite scaffolds. *PLoS One* **10**, 1–16 (2015).

126. Lee, S. S., Santschi, M. & Ferguson, S. J. A Biomimetic Macroporous Hybrid Scaffold with Sustained Drug Delivery for Enhanced Bone Regeneration. *Biomacromolecules* **22**, 2460–2471 (2021).

127. Kubina, R. *et al.* Fisetin, a Potent Anticancer Flavonol Exhibiting Cytotoxic Activity against Neoplastic Malignant Cells and Cancerous Conditions: A Scoping, Comprehensive Review. *Nutrients* **14**, (2022).

128. Wang, Q., Atluri, K., Tiwari, A. K. & Babu, R. J. Exploring the Application of Micellar Drug Delivery Systems in Cancer Nanomedicine. *Pharmaceuticals* **16**, 433 (2023).

129. Hiraishi, S. *et al.* Discogenic cell transplantation directly from a cryopreserved state in an induced intervertebral disc degeneration canine model. *JOR Spine* **1**, 1–9 (2018).

130. Xu, J. *et al.* BMP7 enhances the effect of BMSCs on extracellular matrix remodeling in a rabbit model of intervertebral disc degeneration. *FEBS J.* **283**, 1689–1700 (2016).

131. Rahmi, G. *et al.* Designing 3D mesenchymal stem cell sheets merging magnetic and fluorescent features: When cell sheet technology meets image-guided cell therapy. *Theranostics* **6**, 739–751 (2016).

132. Pereira, C. L. *et al.* Mesenchymal Stem/Stromal Cells seeded on cartilaginous endplates promote Intervertebral Disc Regeneration through Extracellular Matrix Remodeling. *Sci. Rep.* **6**, 1–17 (2016).

133. Peng, Y. *et al.* Decellularized Disc Hydrogels for hBMSCs tissue-specific differentiation and tissue regeneration. *Bioact. Mater.* **6**, 3541–3556 (2021).

134. Edd, J. F., Horowitz, L., Davalos, R. V., Mir, L. M. & Rubinsky, B. In vivo results of a new focal tissue ablation technique: Irreversible electroporation. *IEEE Trans. Biomed. Eng.* **53**, 1409–1415 (2006).

135. Iatridis, J. C., Kang, J., Kandel, R. & Risbud, M. V. New horizons in spine research: Intervertebral disc repair and regeneration. *J. Orthop. Res.* **35**, 5–7 (2017).

136. Spillekom, S. *et al.* Increased osmolarity and cell clustering preserve canine notochordal cell phenotype in culture. *Tissue Eng. - Part C Methods* **20**, 652–662 (2014).

137. Richardson, S. M. Arthritis Research & Therapy identification of normal and degenerate human intervertebral disc cell Transcriptional profiling of bovine intervertebral disc cells : implications for identification of normal and Addresses : *Injury* 1–20 (2010).

138. Su, Y. *et al.* A hierarchically ordered compacted coil scaffold for tissue regeneration. *NPG Asia Mater.* **12**, 4–13 (2020).

139. Edgar, L. *et al.* Heterogeneity of scaffold biomaterials in tissue engineering. *Materials (Basel).* **9**, (2016).

140. Tazi, N. *et al.* Hydroxyapatite bioactivated bacterial cellulose promotes osteoblast growth and the formation of bone nodules. *AMB Express* **2**, 1–10 (2012).

141. Ghuman, H. & Modo, M. Biomaterial applications in neural therapy and repair. *Chinese Neurosurg. J.* **2**, 1–8 (2016).

142. Lv, B. *et al.* Functionalized multidimensional biomaterials for bone microenvironment engineering applications: Focus on osteoimmunomodulation. *Front. Bioeng. Biotechnol.* **10**, 1–19 (2022).

143. Marew, T. & Birhanu, G. Three dimensional printed nanostructure biomaterials for bone tissue engineering. *Regen. Ther.* **18**, 102–111 (2021).

144. Zhang, Q., Li, M., Hu, W., Wang, X. & Hu, J. Spidroin-Based Biomaterials in Tissue Engineering: General Approaches and Potential Stem Cell Therapies. *Stem Cells Int.* **2021**, (2021).

145. Soto-Quintero, A., González-Alva, P., Covelo, A. & Hernández, M. A. Study of the in vitro degradation and characterization of the HaCat keratinocytes adherence on electrospun scaffolds based polyvinyl alcohol/sodium alginate. *J. Appl. Polym. Sci.* **139**, 1–14 (2022).

146. Chou, S. F. & Woodrow, K. A. Relationships between mechanical properties and drug release from electrospun fibers of PCL and PLGA blends. *J. Mech. Behav. Biomed. Mater.* **65**, 724–733 (2017).

147. Kim, Y. S., Majid, M., Melchiorri, A. J. & Mikos, A. G. Applications of decellularized extracellular matrix in bone and cartilage tissue engineering. *Bioeng. Transl. Med.* **4**, 83–95 (2019).

148. Lan, X. *et al.* Bioprinting of human nasoseptal chondrocytes-laden collagen hydrogel for cartilage tissue engineering. *FASEB J.* **35**, 1–14 (2021).

149. Bezuidenhout, D., Limbert, G., Moscato, F. & Davies, N. H. 1,2,$,. 1–22 (2020).

150. Ong, K. L., Yun, B. M. & White, J. B. New biomaterials for orthopedic implants. *Orthop. Res. Rev.* **7**, 107–130 (2015).

151. Huong, L. Three - dimensional scaffold platform for controlled therapeutic drug and non - viral gene delivery to enhance nerve regeneration and remyelination in spinal cord injuries THREE-DIMENSIONAL SCAFFOLD PLATFORM NON-VIRAL GENE DELIVERY TO ENHANCE. (2018).

152. Baek, K. and Future Insights. 1–37 (2021).

153. Dimitriou, P., Li, J., Tornillo, G., McCloy, T. & Barrow, D. Droplet Microfluidics for Tumor Drug-Related Studies and Programmable Artificial Cells. *Glob. Challenges* **5**, (2021).

154. Dai, R., Wang, Z., Samanipour, R., Koo, K. I. & Kim, K. Adipose-Derived Stem Cells for Tissue Engineering and Regenerative Medicine Applications. *Stem Cells Int.* **2016**, (2016).

155. Hopf, A. *et al.* Optimized Decellularization Protocol for Large Peripheral Nerve Segments: Towards Personalized Nerve Bioengineering. *Bioengineering* **9**, (2022).

156. Hafeez, M. N. *et al.* Tendon Tissue Repair in Prospective of Drug Delivery, Regenerative Medicines, and Innovative Bioscaffolds. *Stem Cells Int.* **2021**, (2021).

157. O'Rourke, S. A., Dunne, A. & Monaghan, M. G. The Role of Macrophages in the Infarcted Myocardium: Orchestrators of ECM Remodeling. *Front. Cardiovasc. Med.* **6**, 1–12 (2019).

158. Bernhard, J. C. & Vunjak-Novakovic, G. Should we use cells, biomaterials, or tissue engineering for cartilage regeneration? *Stem Cell Res. Ther.* **7**, 3–11 (2016).

159. Rioux, Y., Fradette, J., Maciel, Y., Bégin-Drolet, A. & Ruel, J. Biofabrication of Sodium Alginate Hydrogel Scaffolds for Heart Valve Tissue Engineering. *Int. J. Mol. Sci.* **23**, (2022).

160. Casarin, M., Morlacco, A. & Dal Moro, F. Bladder substitution: The role of tissue engineering and biomaterials. *Processes* **9**, 1–16 (2021).

161. Sokoła-Wysoczańska, E. *et al.* Polyunsaturated fatty acids and their potential therapeutic role in cardiovascular system disorders—a review. *Nutrients* **10**, 1–21 (2018).

162. Sedlář, A. *et al.* Interaction between galectin-3 and integrins mediates cell-matrix adhesion in endothelial cells and mesenchymal stem cells. *Int. J. Mol. Sci.* **22**, (2021).

163. Silvestre, J. S. *et al.* Transplantation of Bone Marrow-Derived Mononuclear Cells in Ischemic Apolipoprotein E-Knockout Mice Accelerates Atherosclerosis Without Altering Plaque Composition. *Circulation* **108**, 2839–2842 (2003).

164. Rieder, E. *et al.* Decellularization protocols of porcine heart valves differ importantly in efficiency of cell removal and susceptibility of the matrix to recellularization with human vascular cells. *J. Thorac. Cardiovasc. Surg.* **127**, 399–405 (2004).

165. Kasimir, M. T. *et al.* Comparison of different decellularization procedures of porcine heart valves. *Int. J. Artif. Organs* **26**, 421–427 (2003).

166. Crapo, P. M., Gilbert, T. W. & Badylak, S. F. An overview of tissue and whole organ decellularization processes. *Biomaterials* **32**, 3233–3243 (2011).

167. Akiyama, H. & Heller, R. *Bioelectrics*. (Springer Japan, 2017). doi:10.1007/978-4-431-56095-1_1.

168. Rubinsky, B. *Irreversible Electroporation*. (Springer-Verlag Berlin Heidelberg, 2010). doi:10.1007/978-3-642-05420-4.

169. Neumann, Eberhard; Pakhomov, Andrei G.; Miklavčič, Damijan; Markov, M. Advanced electroporation techniques in biology and medicine-CRC Press (2010).pdf. (2010).

170. Miklavčič, D. *et al.* The importance of electric field distribution for effective in vivo electroporation of tissues. *Biophys. J.* **74**, 2152–2158 (1998).

171. Davalos, Rafael V. Garcia, Paulo A. Edd, J. F. Thermal effects of irreversible electroporation. *Irreversible Electroporation Clin. Pract.* 121–136 (2017) doi:10.1007/978-3-319-55113-5_9.

172. Trainito, C., Claudia, M. & Trainito, I. Study of cell membrane permeabilization induced by pulsed electric field – electrical modeling and characterization on biochip To cite this version : HAL Id : tel-01254036 DE L ' UNIVERSITE PARIS-SACLAY ,. (2016).

173. Kuang, W. & Nelson, S. O. Low-frequency dielectric properties of biological tissues: A review with some new insights. *Trans. Am. Soc. Agric. Eng.* **41**, 173–184 (1998).

174. Pethig, R. Dielectric properties of biological materials: Biophysical and medical applications. *IEEE Trans. Electr. Insul.* **EI-19**, 453–474 (1984).

175. Martinsen, O. G., Grimnes, S., Schwan, H. P., Rikshospitalet, O. & ... Interface phenomena and dielectric properties of biological tissue. *Encycl. Surf. Colloid Sci.* 2643–2652 (2002).

176. Gabriel, C. Dielectric properties of biological tissue: Variation with age. *Bioelectromagnetics* **26**, 12–18 (2005).

177. Bhonsle, S. P., Arena, C. B., Sweeney, D. C. & Davalos, R. V. Mitigation of impedance changes due to electroporation therapy using bursts of high-frequency bipolar pulses. *Biomed. Eng. Online* **15**, (2015).

178. Bera, T. K. Bioelectrical Impedance and the Frequency Dependent Current Conduction Through Biological Tissues: A Short Review. *IOP Conf. Ser. Mater. Sci. Eng.* **331**, (2018).

179. Davalos, R. V., Rubinsky, B. & Otten, D. M. A feasibility study for electrical impedance tomography as a means to monitor tissue electroporation for molecular medicine. *IEEE Trans. Biomed. Eng.* **49**, 400–403 (2002).

180. Garcia, P. A., Rossmeisl, J. H., Neal, R. E., Ellis, T. L. & Davalos, R. V. A parametric study delineating irreversible electroporation from thermal damage based on a minimally invasive intracranial procedure. *Biomed. Eng. Online* **10**, (2011).

181. García-Sánchez, T., Voyer, D., Poignard, C. & Mir, L. M. Physiological changes may dominate the electrical properties of liver during reversible electroporation: Measurements and modelling. *Bioelectrochemistry* **136**, (2020).

182. Fesmire, C. C., Petrella, R. A., Kaufman, J. D., Topasna, N. & Sano, M. B. Irreversible electroporation is a thermally mediated ablation modality for pulses on the order of one microsecond. *Bioelectrochemistry* **135**, 107544 (2020).

183. Beitel-White, Natalie ; Lorenzo, Melvin F.; Zhao. Yajun; Brock, Rebecca M.; Coutermarsh-Ott, Sheryl; Manuchehrabadi, Navid; Allen, Irvin C.; Davalos, R. V. Multi-tissue Analysis on the Impact of Electroporation on Electrical and Thermal Properties. *Physiol. Behav.* **176**, 139–148 (2016).

184. Halter, R. J., Hartov, A., Paulsen, K. D., Schned, A. & Heaney, J. Genetic and least squares algorithms for estimating spectral EIS parameters of prostatic tissues. *Physiol. Meas.* **29**, (2008).

185. Shao, F. *et al.* Tissue discrimination by bioelectrical impedance during PLL resection in anterior decompression surgery for treatment of cervical spondylotic myelopathy. *J. Orthop. Surg. Res.* **14**, 1–8 (2019).

186. Kim, H. B. *et al.* Effects of different applied voltages of irreversible electroporation on prostate cancer in a mouse model. *Sci. Rep.* **12**, 1–9 (2022).

187. Del Rosal, B., Sun, C., Loufakis, D. N., Lu, C. & Jaque, D. Thermal loading in flow-through electroporation microfluidic devices. *Lab Chip* **13**, 3119–3127 (2013).

188. Phillips, M., Maor, E. & Rubinsky, B. Nonthermal irreversible electroporation for tissue decellularization. *J. Biomech. Eng.* **132**, 1–8 (2010).

189. Davalos, R. V., Mir, L. M. & Rubinsky, B. Tissue ablation with irreversible electroporation. *Ann. Biomed. Eng.* **33**, 223–231 (2005).

190. Phillips, M., Maor, E. & Rubinsky, B. Principles of tissue engineering with nonthermal irreversible electroporation. *J. Heat Transfer* **133**, 1–8 (2011).

191. Walsh, W. R. & Guzelsu, N. Electrokinetic behavior of intact wet bone: Compartmental model. *J. Orthop. Res.* **9**, 683–692 (1991).

192. Yang, B. *et al.* Comparison of electrical impedance tomography and intracranial pressure during dehydration treatment of cerebral edema. *NeuroImage Clin.* **23**, 101909 (2019).

193. Faraji, A. H., Jaquins-Gerstl, A. S., Valenta, A. C., Ou, Y. & Weber, S. G. Electrokinetic Convection-Enhanced Delivery of Solutes to the Brain. *ACS Chem. Neurosci.* **11**, 2085–2093 (2020).

194. Scholz, F. Electroanalytical methods: Guide to experiments and applications. *Electroanal. Methods Guid. to Exp. Appl.* 1–359 (2010) doi:10.1007/978-3-642-02915-8.

195. Grodzinsky, A. J. *Fields, Forces, and Flows in Biological Systems*. (Garland Science, 2019).

196. Yan, D., Nguyen, N. T., Yang, C. & Huang, X. Visualizing the transient electroosmotic flow and measuring the zeta potential of microchannels with a micro-PIV technique. *J. Chem. Phys.* **124**, (2006).

197. Khairulina, K., Chung, U. Il & Sakai, T. New design of hydrogels with tuned electro-osmosis: A potential model system to understand electro-kinetic transport in biological tissues. *J. Mater. Chem. B* **5**, 4526–4534 (2017).

198. Upcroft, P. & Upcroft, J. A. Comparison of properties of adarose for electrophoresis of DNA. **618**, 19–27 (1993).

199. Slater, G. W. *et al.* Theory of DNA electrophoresis (~ 1999-2002 1/2). *Electrophoresis* **23**, 3791–3816 (2002).

200. ThermoFisher Scientific. Nucleic Acid Gel Electrophoresis - A Brief Overview and History.

201. Viovy, J. L. Electrophoresis of DNA and other polyelectrolytes: Physical mechanisms. *Rev. Mod. Phys.* **72**, 813–872 (2000).

202. Hunckler, M. D., Tilley, J. M. R. & Roeder, R. K. Molecular transport in collagenous tissues measured by gel electrophoresis. *J. Biomech.* **48**, 4087–4092 (2015).

203. Minor, M., Van Der Linde, A. J., Van Leeuwen, H. P. & Lyklema, J. Dynamic aspects of electrophoresis and electroosmosis: A new fast method for measuring particle mobilities. *J. Colloid Interface Sci.* **189**, 370–375 (1997).

204. Petersen, N. J., Nikolajsen, R. P. H., Mogensen, K. B. & Kutter, J. P. Effect of Joule heating on efficiency and performance for microchip-based and capillary-based electrophoretic separation systems: A closer look. *Electrophoresis* **25**, 253–269 (2004).

205. Huang, M. & Lai, F. C. Effects of joule heating on ehd-enhanced natural convection in an enclosure. *8th AIAA/ASME Jt. Thermophys. Heat Transf. Conf.* 1851–1858 (2002) doi:10.2514/6.2002-3318.

206. Reynaud, B. & Quinn, T. M. Tensorial electrokinetics in articular cartilage. *Biophys. J.* **91**, 2349–2355 (2006).

207. Zhu, J. J., Grodzinsky, A. J. & Smith, A. C. Transport Studies of Chondroitin Sulfate Disaccharide Through Articular Cartilage by by. (1997).

208. Travascio, F. & Gu, W. Y. Simultaneous measurement of anisotropic solute diffusivity and binding reaction rates in biological tissues by FRAP. *Ann. Biomed. Eng.* **39**, 53–65 (2011).

209. Cetin, B. & Li, D. Effect of Joule heating on electrokinetic transport. *Electrophoresis* **29**, 994–1005 (2008).

210. Maor, E., Ivorra, A., Mitchell, J. J. & Rubinsky, B. Vascular smooth muscle cells ablation with endovascular nonthermal irreversible electroporation. *J. Vasc. Interv. Radiol.* **21**, 1708–1715 (2010).

211. Sano, M. B. *et al.* Towards the creation of decellularized organ constructs using irreversible electroporation and active mechanical perfusion. *Biomed. Eng. Online* **9**, 1–16 (2010).

212. Buchmann, L., Frey, W., Gusbeth, C., Ravaynia, P. S. & Mathys, A. Effect of nanosecond pulsed electric field treatment on cell proliferation of microalgae. *Bioresour. Technol.* **271**, 402–408 (2019).

213. Laufer, S., Ivorra, A., Reuter, V. E., Rubinsky, B. & Solomon, S. B. Electrical impedance characterization of normal and cancerous human hepatic tissue. *Physiol. Meas.* **31**, 995–1009 (2010).

214. Krishnamoorthy, S., Zhang, Z. & Xu, C. Guided cell migration on a graded micropillar substrate. *Bio-Design Manuf.* **3**, 60–70 (2020).

215. Chao, P. hsiu G., Lu, H. H., Hung, C. T., Nicoll, S. B. & Bulinski, J. C. Effects of applied DC electric field on ligament fibroblast migration and wound healing. *Connect. Tissue Res.* **48**, 188–197 (2007).

216. O'Hare, M. J., Ormerod, M. G., Imrie, P. R., Peacock, J. H. & Asche, W. Electropermeabilization and Electrosensitivity of Different Types of Mammalian Cells. *Electroporation Electrofusion Cell Biol.* 319–330 (1989) doi:10.1007/978-1-4899-2528-2_20.

217. Fitzsimmons, R. J., Gordon, S. L., Kronberg, J., Ganey, T. & Pilla, A. A. A pulsing electric field (PEF) increases human chondrocyte proliferation through a transduction pathway involving nitric oxide signaling. *J. Orthop. Res.* **26**, 854–859 (2008).

218. Zaharoff, D. A., Barr, R. C., Li, C. Y. & Yuan, F. Electromobility of plasmid DNA in tumor tissues during electric field-mediated gene delivery. *Gene Ther.* **9**, 1286–1290 (2002).

219. Wang, S., Zhang, X., Wang, W. & Lee, L. J. Semicontinuous flow electroporation chip for high-throughput transfection on mammalian cells. *Anal. Chem.* **81**, 4414–4421 (2009).

220. Cervia, L. D., Chang, C. C., Wang, L., Mao, M. & Yuan, F. Enhancing Electrotransfection Efficiency through Improvement in Nuclear Entry of Plasmid DNA. *Mol. Ther. - Nucleic Acids* **11**, 263–271 (2018).

221. Du, H., Hou, P., Zhang, W. & Li, Q. Advances in CLARITY-based tissue clearing and imaging (Review). *Exp. Ther. Med.* **16**, 1567–1576 (2018).

222. Richardson, D. S. & Lichtman, J. W. Clarifying Tissue Clearing. *Cell* **162**, 246–257 (2015).

223. Lee, H., Park, J. H., Seo, I., Park, S. H. & Kim, S. Improved application of the electrophoretic tissue clearing technology, CLARITY, to intact solid organs including brain, pancreas, liver, kidney, lung, and intestine. *BMC Dev. Biol.* **14**, 1–7 (2014).

224. Jensen, K. H. R. & Berg, R. W. Advances and perspectives in tissue clearing using CLARITY. *J. Chem. Neuroanat.* **86**, 19–34 (2017).

225. Kim, S. Y. *et al.* Stochastic electrotransport selectively enhances the transport of highly electromobile molecules. *Proc. Natl. Acad. Sci. U. S. A.* **112**, E6274–E6283 (2015).

226. Roberts, S., Evans, H., Trivedi, J. & Menage, J. Histology and pathology of the human intervertebral disc. *J. Bone Jt. Surg. - Ser. A* **88**, 10–14 (2006).

227. Jin, L. *et al.* Annulus fibrosus cell characteristics are a potential source of intervertebral disc pathogenesis. *PLoS One* **9**, (2014).

228. Sakai, D. & Schol, J. Cell therapy for intervertebral disc repair: Clinical perspective. *J. Orthop. Transl.* **9**, 8–18 (2017).

229. Fomby, P. *et al.* Stem cells and cell therapies in lung biology and diseases: Conference report. *Ann. Am. Thorac. Soc.* **12**, 181–204 (2010).

230. Benneker, L. M. *et al.* Cell therapy for intervertebral disc repair: Advancing cell therapy from bench to clinics. *Eur. Cells Mater.* **27**, 5–11 (2014).

231. Hu, B. *et al.* Intervertebral disc-derived stem/progenitor cells as a promising cell source for intervertebral disc regeneration. *Stem Cells Int.* **2018**, (2018).

232. Sakai, D. & Andersson, G. B. J. Stem cell therapy for intervertebral disc regeneration: Obstacles and solutions. *Nat. Rev. Rheumatol.* **11**, 243–256 (2015).

233. Dubey, A. K., Gupta, S. D. & Basu, B. Optimization of electrical stimulation parameters for enhanced cell proliferation on biomaterial surfaces. *J. Biomed. Mater. Res. - Part B Appl. Biomater.* **98 B**, 18–29 (2011).

234. Vadlamani, R. A. *et al.* Nanosecond pulsed electric field induced proliferation and differentiation of osteoblasts and myoblasts. *J. R. Soc. Interface* **16**, (2019).

235. Pakhomov, A. G. *et al.* Membrane permeabilization and cell damage by ultrashort electric field shocks. *Arch. Biochem. Biophys.* **465**, 109–118 (2007).

236. Breton, M. & Mir, L. M. Microsecond and nanosecond electric pulses in cancer treatments. *Bioelectromagnetics* **33**, 106–123 (2012).

237. Čemažar, M. *et al.* Effect of electric-field intensity on electropermeabilization and electrosensitivity of various tumor-cell lines in vitro. *Electromagn. Biol. Med.* **17**, 263–272 (1998).

238. Saulis, G. *et al.* Theoretical analysis and experimental determination of the relationships between the parameters of the electric field pulse required to electroporate the cells. *IEEE Trans. Plasma Sci.* **41**, 2913–2919 (2013).

239. Hanna, H., Denzi, A., Liberti, M., André, F. M. & Mir, L. M. Electropermeabilization of Inner and Outer Cell Membranes with Microsecond Pulsed Electric Fields: Quantitative Study with Calcium Ions. *Sci. Rep.* **7**, 1–14 (2017).

240. Casciati, A. *et al.* Effects of Ultra-Short Pulsed Electric Field Exposure on Glioblastoma Cells. *Int. J. Mol. Sci.* **23**, (2022).

241. Ibey, B. L. *et al.* Selective cytotoxicity of intense nanosecond-duration electric pulses in mammalian cells. *Biochim. Biophys. Acta - Gen. Subj.* **1800**, 1210–1219 (2010).

242. Hartig, M., Joos, U. & Wiesmann, H. P. Capacitively coupled electric fields accelerate proliferation of osteoblast-like primary cells and increase bone extracellular matrix formation in vitro. *Eur. Biophys. J.* **29**, 499–506 (2000).

243. Brighton, C. T., Jensen, L., Pollack, S. R., Tolin, B. S. & Clark, C. C. Proliferative and synthetic response of bovine growth plate chondrocytes to various capacitively coupled electrical fields. *J. Orthop. Res.* **7**, 759–765 (1989).

244. Jezierska-Wozniak, K. *et al.* Migration of human mesenchymal stem cells stimulated with pulsed electric field and the dynamics of the cell surface glycosylation. *Migr. Hum. mesenchymal stem cells Stimul. with pulsed Electr. F. Dyn. cell Surf. glycosylation* 122382 (2017) doi:10.1101/122382.

245. Tai, G., Tai, M. & Zhao, M. Electrically stimulated cell migration and its contribution to wound healing. *Burn. Trauma* **6**, 1–7 (2018).

246. Funk, R. H. W. Endogenous electric fields as guiding cue for cell migration. *Front. Physiol.* **6**, 1–8 (2015).

247. Chang, K., Chang, W. H. S., Wu, M. L. & Shih, C. Effects of Different Intensities of Extremely Low Frequency Pulsed Electromagnetic Fields on Formation of Osteoclast-Like Cells. *Bioelectromagnetics* **24**, 431–439 (2003).

248. Lohmann, C. H. *et al.* Pulsed electromagnetic field stimulation of MG63 osteoblast-like cells affects differentiation and local factor production. *J. Orthop. Res.* **18**, 637–646 (2000).

249. Aaron, R. K., Boyan, B. D., Ciombor, D. M. K., Schwartz, Z. & Simon, B. J. Stimulation of Growth Factor Synthesis by Electric and Electromagnetic Fields. *Clin. Orthop. Relat. Res.* 30–37 (2004) doi:10.1097/00003086-200402000-00006.

250. Jamil, M. M. A., Zaltum, M. A. M., Youseffi, M. & Javid, F. Study on Pulse Electric Field Exposure Effect on HeLa Cells for Wound Healing Application. *J. Phys. Conf. Ser.* **1372**, (2019).

251. Safaei, Z. & Thompson, G. L. Histone deacetylase 4 and 5 translocation elicited by microsecond pulsed electric field exposure is mediated by kinase activity. 1–21 (2022) doi:10.3389/fbioe.2022.1047851.

252. Atsu, P. M. & Thompson, G. L. Electrical impedance decreases in annulus fibrosus cartilage exposed to microsecond pulsed electric fields ex vivo Electrical impedance decreases in annulus fibrosus cartilage exposed to microsecond pulsed electric fields ex vivo.

253. May, R. D. *et al.* Efficient nonviral transfection of primary intervertebral disc cells by electroporation for tissue engineering application. *Tissue Eng. - Part C Methods* **23**, 30–37 (2017).

254. Tanori, M. *et al.* Microsecond Pulsed Electric Fields: An Effective Way to Selectively Target and Radiosensitize Medulloblastoma Cancer Stem Cells. *Int. J. Radiat. Oncol. Biol. Phys.* **109**, 1495–1507 (2021).

255. Hsieh, C. H., Lu, C. H., Chen, W. T., Ma, B. L. & Chao, C. Y. Application of non-invasive low strength pulsed electric field to EGCG treatment synergistically enhanced the inhibition effect on PANC-1 cells. *PLoS One* **12**, 1–17 (2017).

256. Bera, T. K., Jampana, N. & Lubineau, G. A LabVIEW-based electrical bioimpedance spectroscopic data interpreter (LEBISDI) for biological tissue impedance analysis and equivalent circuit modelling. *J. Electr. Bioimpedance* **7**, 35–54 (2016).

257. Hernández-Balaguera, E., López-Dolado, E. & Polo, J. L. Obtaining electrical equivalent circuits of biological tissues using the current interruption method, circuit theory and fractional calculus. *RSC Advances* vol. 6 22312–22319 (2016).

258. Ramos, A., Raizer, A. & Marques, J. L. B. A new computational approach for electrical analysis of biological tissues. *Bioelectrochemistry* **59**, 73–84 (2003).

259. Clemente, F., Romano, M., Bifulco, P. & Cesarelli, M. EIS measurements for characterization of muscular tissue by means of equivalent electrical parameters. *Meas. J. Int. Meas. Confed.* **58**, 476–482 (2014).

260. Yao, J. *et al.* Evaluation of electrical characteristics of biological tissue with electrical impedance spectroscopy. *Electrophoresis* **41**, 1425–1432 (2020).

261. Oshin, E. A., Guo, S. & Jiang, C. Determining tissue conductivity in tissue ablation by nanosecond pulsed electric fields. *Bioelectrochemistry* **143**, 107949 (2022).

262. Pereira, R. N., Galindo, F. G., Vicente, A. A. & Dejmek, P. Effects of pulsed electric field on the viscoelastic properties of potato tissue. *Food Biophys.* **4**, 229–239 (2009).

263. Neal, R. E., Garcia, P. A., Robertson, J. L. & Davalos, R. V. Experimental characterization and numerical modeling of tissue electrical conductivity during pulsed electric fields for irreversible electroporation treatment planning. *IEEE Trans. Biomed. Eng.* **59**, 1076–1085 (2012).

264. Gantenbein, B., S. Croft, A. & Larraillet, M. Mammalian Cell Viability Methods in 3D Scaffolds for Tissue Engineering. *Fluoresc. Methods Investig. Living Cells Microorg.* (2020) doi:10.5772/intechopen.93078.

265. Haemmerich, D., Schutt, D. J., Wright, A. W., Webster, J. G. & Mahvi, D. M. Electrical conductivity measurement of excised human metastatic liver tumours before and after thermal ablation. *Physiol. Meas.* **30**, 459–466 (2009).

266. Gabriel, C., Peyman, A. & Grant, E. H. Electrical conductivity of tissue at frequencies below 1 MHz. *Phys. Med. Biol.* **54**, 4863–4878 (2009).

267. Costa, E. L. V., Lima, P. G. & Amato, M. B. R. Electrical impedance tomography. *Curr. Opin. Crit. Care* **15**, 18–24 (2009).

268. Boone, K., Barber, D. & Brown, B. Imaging with electricity: Report of the European Concerted Action on Impedance Tomography. *J. Med. Eng. Technol.* **21**, 201–232 (1997).

269. Bayford, R. H. Bioimpedance Tomography (Electrical Impedance Tomography). *Annu. Rev. Biomed. Eng.* **8**, 63–91 (2006).

270. Boone, K. G. & Holder, D. S. Current approaches to analogue instrumentation design in electrical impedance tomography. *Physiol. Meas.* **17**, 229–247 (1996).

271. Gun, L., Ning, D. & Liang, Z. Effective Permittivity of Biological Tissue: Comparison of Theoretical Model and Experiment. *Math. Probl. Eng.* **2017**, (2017).

272. Vorlíček, J., Oppl, L. & Vrba, J. Measurement of complex permittivity of biological tissues. *PIERS 2010 Cambridge - Prog. Electromagn. Res. Symp. Proc.* 599–601 (2010).

273. Dean, D. A.; Ramanathan, T.; Machado, D.; Sundararajan, R. Electrical Impedance Spectroscopy Study of Biological Tissues. *Mol. Cell. Biochem.* **23**, 1–7 (2012).

274. Prakash, S. *et al.* Ex vivo electrical impedance measurements on excised hepatic tissue from human patients with metastatic colorectal cancer. *Physiol. Meas.* **36**, 315–328 (2015).

275. Schindelin, J. *et al.* Fiji: An open-source platform for biological-image analysis. *Nat. Methods* **9**, 676–682 (2012).

276. Rubinsky, B., Onik, G. & Mikus, P. Irreversible electroporation: A new ablation modality - Clinical implications. *Technol. Cancer Res. Treat.* **6**, 37–48 (2007).

277. Šel, D. *et al.* Sequential finite element model of tissue electropermeabilization. *IEEE Trans. Biomed. Eng.* **52**, 816–827 (2005).

278. Chang, I. Finite element analysis of hepatic radiofrequency ablation probes using temperature-dependent electrical conductivity. *Biomed. Eng. Online* **2**, 1–18 (2003).

279. Miklavčič, D., Pavšelj, N. & Hart, F. X. Electric Properties of Tissues. *Wiley Encycl. Biomed. Eng.* 1–12 (2006) doi:10.1002/9780471740360.ebs0403.

280. Oddy, M. H. & Santiago, J. G. A method for determining electrophoretic and electroosmotic mobilities using AC and DC electric field particle displacements. *J. Colloid Interface Sci.* **269**, 192–204 (2004).

281. Sadek, S. H., Pimenta, F., Pinho, F. T. & Alves, M. A. Measurement of electroosmotic and electrophoretic velocities using pulsed and sinusoidal electric fields. *Electrophoresis* **38**, 1022–1037 (2017).

282. Lewpiriyawong, N., Yang, C. & Lam Cheong, Y. Dielectrophoretic manipulation of particles in a modified microfluidic H filter with multi-insulating blocks. *Biomicrofluidics* **2**, (2008).

283. Frank, E. H., Grodzinsky, A. J., Koob, T. J. & Eyre, D. R. Streaming potentials: A sensitive index of enzymatic degradation in articular cartilage. *J. Orthop. Res.* **5**, 497–508 (1987).

284. Yan, D., Yang, C., Nguyen, N. T. & Huang, X. A method for simultaneously determining the zeta potentials of the channel surface and the tracer particles using microparticle image velocimetry techinique. *Electrophoresis* **27**, 620–627 (2006).

285. Swartz, M. A. & Fleury, M. E. Interstitial flow and its effects in soft tissues. *Annu. Rev. Biomed. Eng.* **9**, 229–256 (2007).

286. Bajpayee, A. G., Scheu, M., Grodzinsky, A. J. & Porter, R. M. Electrostatic interactions enable rapid penetration, enhanced uptake and retention of intra-articular injected avidin in rat knee joints. *J. Orthop. Res.* **32**, 1044–1051 (2014).

287. Choi, J., Lee, E., Kim, J. H. & Sun, W. FxClear, a free-hydrogel electrophoretic tissue clearing method for rapid de-lipidation of tissues with high preservation of immunoreactivity. *Exp. Neurobiol.* **28**, 436–445 (2019).

288. Sajjadi, S. H., Goharshadi, E. K. & Ahmadzadeh, H. Heat dissipation in slab gel electrophoresis: The effect of embedded TiO 2 nanoparticles on the thermal profiles. *J. Chromatogr. B Anal. Technol. Biomed. Life Sci.* **1118–1119**, 63–69 (2019).

289. Rush, R. S., Cohen, A. S. & Karger, B. L. Influence of Column Temperature on the Electrophoretic Behavior of Myoglobin and α-Lactalbumin in High-Performance Capillary Electrophoresis. *Anal. Chem.* **63**, 1346–1350 (1991).

290. De Mello, A. J., Habgood, M., Lancaster, N. L., Welton, T. & Wootton, R. C. R. Precise temperature control in microfluidic devices using Joule heating of ionic liquids. *Lab Chip* **4**, 417–419 (2004).

291. Song, L. *et al.* Joule heating effects on electrokinetic flows with conductivity gradients. *Electrophoresis* **42**, 967–974 (2021).

292. Vergari, C., Mansfield, J., Meakin, J. R. & Winlove, P. C. Lamellar and fibre bundle mechanics of the annulus fibrosus in bovine intervertebral disc. *Acta Biomater.* **37**, 14–20 (2016).

293. Zhu, D. *et al.* Micro-structure and mechanical properties of annulus fibrous of the L4-5 and L5-S1 intervertebral discs. *Clin. Biomech.* **23**, 74–82 (2008).

294. Pereira, C. L. *et al.* Mesenchymal Stem/Stromal Cells seeded on cartilaginous endplates promote Intervertebral Disc Regeneration through Extracellular Matrix Remodeling. *Sci. Rep.* **6**, 1–17 (2016).

295. Xu, N. *et al.* Fast free-of-acrylamide clearing tissue (FACT) - An optimized new protocol for rapid, high-resolution imaging of three-dimensional brain tissue. *Sci. Rep.* **7**, 1–15 (2017).

296. Király, K. *et al.* Safranin O reduces loss of glycosaminoglycans from bovine articular cartilage during histological specimen preparation. *Histochem. J.* **28**, 99–107 (1996).

297. Banaszkiewicz, P. A. & Kader, D. F. Classic papers in orthopaedics. *Class. Pap. Orthop.* **18**, 1–624 (2014).

298. Darzynkiewicz, Z., Kapuscinski, J., Traganos, F. & Crissman, H. A. Application of pyronin Y(G) in cytochemistry of nucleic acids. *Cytometry* **8**, 138–145 (1987).

299. Gu, W. Y., Lai, W. M. & Mow, V. C. Transport of Multi-Electrolytes in Charged Hydrated Biological Soft Tissues. *Transp. Porous Media* **34**, 143–157 (1999).

300. Xuan, X. Joule heating in electrokinetic flow. *Electrophoresis* **29**, 33–43 (2008).

301. Barth, M., Diepers, M., Weiss, C. & Thomé, C. Two-year outcome after lumbar microdiscectomy versus microscopic sequestrectomy - Part 2: Radiographic evaluation and correlation with clinical outcome. *Spine (Phila. Pa. 1976).* **33**, 273–279 (2008).

302. Barth, M., Weiss, C. & Thomé, C. Two-year outcome after lumbar microdiscectomy versus microscopic sequestrectomy - Part 1: Evaluation of clinical outcome. *Spine (Phila. Pa. 1976).* **33**, 265–272 (2008).

303. Allen, M. J. *et al.* Preclinical Evaluation of a Poly (Vinyl Alcohol) Hydrogel Implant as a Replacement for the Nucleus Pulposus. *Spine (Phila. Pa. 1976).* **29**, 515–523 (2004).

304. Klara, P. M. & Ray, C. D. Artificial nucleus replacement: Clinical experience. *Spine (Phila. Pa. 1976).* **27**, 1374–1377 (2002).

305. Hegewald, A. A. *et al.* Enhancing tissue repair in annulus fi brosus defects of the intervertebral disc : analysis of a bio-integrative annulus implant in an in-vivo ovine model. 405–414 (2015) doi:10.1002/term.

306. Li, Z., Peroglio, M., Grad, S., Eglin, D. & Alini, M. Annulus Fibrosus Repair. *Glob. Spine J.* **4**, s-0034-1376763-s-0034-1376763 (2014).

307. Grunert, P. *et al.* Riboflavin crosslinked high-density collagen gel for the repair of annular defects in intervertebral discs: An in vivo study. *Acta Biomater.* **26**, 215–224 (2015).

308. Chang, I. A. & Nguyen, U. D. Thermal modeling of lesion growth with radiofrequency ablation devices. *Biomed. Eng. Online* **3**, 1–19 (2004).

309. Becker, S. M. & Kuznetsov, A. V. Numerical modeling of in vivo plate electroporation thermal dose assessment. *J. Biomech. Eng.* **128**, 76–84 (2006).

310. Atsu, P. M. *et al.* Electrophoretic Transport Through Fibrocartilage Driven by Square and Sawtooth Pulses With Decreased Joule Heating. *IEEE J. Electromagn. RF Microwaves Med. Biol.* (2023) doi:10.1109/JERM.2023.3264116.

311. Norbertczak, H. T., Ingham, E., Fermor, H. L. & Wilcox, R. K. Decellularized intervertebral discs: A potential replacement for degenerate human discs. *Tissue Engineering - Part C: Methods* vol. 26 565–576 (2020).

Appendix A

In Vitro Evaluation of Cytotoxicity of Metal Coatings

Biocompatibility is a critical aspect in the development and assessment of biomaterials and medical devices, ensuring that these materials are safe and effective when used in medical applications. The concept of biocompatibility revolves around the ability of a material to perform with an appropriate host response in a specific application. This encompasses not only the absence of harmful effects but also the promotion of favorable interactions between the material and the surrounding biological environment. The evaluation of biocompatibility is a multifaceted process, involving a series of tests to assess the interaction of the biomaterial or medical device with the body's tissues and cells. These tests are crucial for determining the safety and efficacy of materials intended for medical use, ranging from implants and prosthetics to tissue scaffolds and drug delivery systems.

In vitro cell culture studies represent the initial phase in the biocompatibility assessment of biomaterials and medical devices. These studies provide essential insights into the cellular responses to the material, such as cytotoxicity, cell proliferation, and inflammatory responses. By employing controlled laboratory conditions, in vitro tests offer a preliminary understanding of how the material interacts with biological systems, which is vital for predicting in vivo behavior. This approach not only helps in screening potential biomaterials efficiently but also reduces the reliance on animal testing in the early stages of development.

The protocols for biocompatibility testing are largely guided by the ISO 10993 standard, a comprehensive set of guidelines that outline the requirements for evaluating the safety of medical devices. This standard encompasses a range of tests, each designed to assess different aspects of biocompatibility, such as cytotoxicity, sensitization, irritation, genotoxicity, and hemocompatibility. The choice of tests depends on the nature of the material, its intended application, and the duration of contact with the body. For instance, materials intended for short-term contact with the skin may require different tests compared to those designed for long-term implantation.

Biocompatibility testing often involves both direct and indirect methods. Direct methods include the evaluation of the material itself, where cells are exposed directly to the biomaterial under study. Indirect methods, on the other hand, involve the use of extracts from the material. These extracts are prepared under controlled conditions to simulate the environment in which the material will be used, and then applied to the cell cultures. This approach is particularly relevant for materials that may release substances over time, as it helps to assess the potential effects of these leachables on biological systems.

The importance of biocompatibility testing cannot be overstated, as it plays a pivotal role in the development of safe and effective medical devices and biomaterials. By adhering to the ISO 10993 standards, researchers and manufacturers can ensure that their products meet the highest safety criteria, thereby protecting patients and enhancing the quality of medical care. As the field of biomaterials continues to evolve, with the development of more complex and sophisticated materials, the role of biocompatibility testing becomes increasingly significant, guiding the safe and responsible advancement of medical technology.

Materials and Method

Substrate preparation

The materials evaluated were the oxides of iridium (Ir), palladium (Pd), rhodium (Rh) and ruthenium (Ru). Silicon (Si) and copper (Cu) were used as negative and positive controls for cell viability, respectively. The test materials were sputter coated onto wells of otherwise untreated six-well cell culture plates. The coating was done such that only one row of the wells were coated and the other was left uncoated for a sham comparison. The plates were sterilized after coating by exposure to UV light for 15 min.

Cell culturing

The NIH Swiss mouse embryo fibroblasts, 3T3 cells were chosen for the basal cytotoxicity test. For neurotoxicity studies, a sub-cloned, immortalized neuronal cell line generated by hybridization of mouse neuroblastoma and post-mitotic rat dorsal root ganglion (DRG), ND7/23 was chosen, since it is commercially available and expresses low-voltage activated calcium channels, making it useful as a model of neuromodulation-based sensory neuron firing. The cells were cultured in Dulbecco's modified eagle's medium (DMEM) supplemented with 10 vol% fetal bovine serum (FBS) and 1 vol% penicillin-streptomycin and incubated at 370C, 5 % CO2 and 95 % humidity. Cells in culture were split at about 90 % confluence using 0.25 w/v% Trypsin-EDTA. The cells were resuspended in DMEM supplemented with 10 vol% FBS and 1 vol% penicillin-streptomycin solution and seeded in the wells coated with the metal oxides and control metals and uncoated polystyrene cell culture wells. The cells were seeded at a concentration of 50×10^4 cells/mL and incubated at physiological conditions. For samples that were incubated for more than 24 h, the media was changed every two days.

Evaluation of cytotoxicity

As prescribed by the ISO 10993, cytotoxicity was evaluated using the alamarBlue™ cell viability assay. The cells were incubated for 24 h, 3 days and 7 days. After the period of incubation, a solution of serum-free media (DMEM) with 10 vol% alamarBlue™ reagent was added and incubated for 5 h. The media solution was then transferred to a 96 well plate, and the absorbance was read with a microplate reader at 570 nm and 650 nm reference. The number of viable cells was obtained by comparing the absorbance of the sample wells to the standard. The percentage of viable cells in the coated wells was calculated by dividing the number of cells from the coated wells by the number of cells from the corresponding uncoated wells and multiplying by 100.

Results: *Viability*

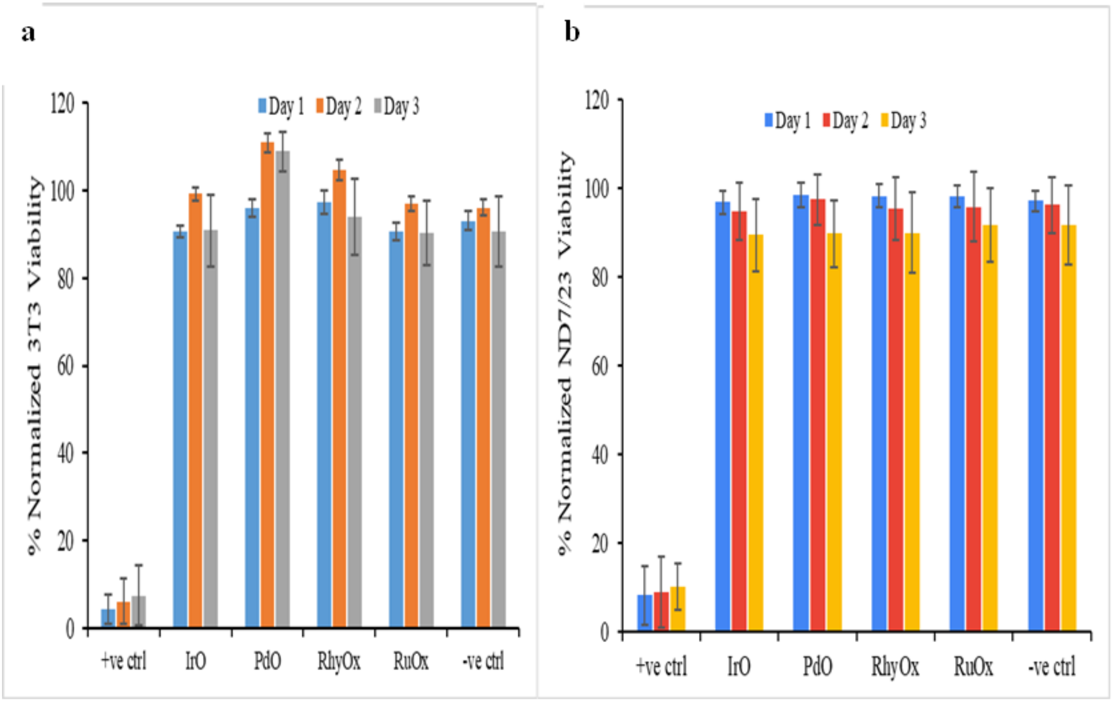

Fig. A1. In vitro analysis of cytotoxicity and neurotoxicity of Iridium oxide (IrO), Palladium oxide (PdO), Rhodium oxide (RhyOx) and Ruthenium oxide (RuOx) coatings. **a)** Normalized cell viability of 3T3 fibroblast cells seeded on the metal oxide coatings and controls with all the oxides showing cytocompatibility with the 3T3 cells. **b)** Normalized cell viability of ND7/23 cells seeded on the metal oxide coatings. All the metal oxides show neurocompatibility and growth kinetics similar to Si, the negative control

The metal oxide coatings were subjected to standard cytotoxicity assay according to ISO 10993 using 3T3 fibroblast and ND7/23 neuronal cell lines. The metal oxides and the negative and positive controls were sputter coated in the well plates. Cells were seeded in the coated wells as well as uncoated well plates. The viability studies were performed after day 0 (24 hr), day 3 and day 7. The cell viabilities from the assay were normalized with the viability from the uncoated wells and reported as a percentage. A material is said to be non-cytotoxic when the normalized cell viability is greater than 70 %. All test materials do not show cytotoxicity after 24 hr including the negative control with both the 3T3 fibroblast cells and ND7/23 neuronal cells. For the 3T3 cells, the normalized cell viabilities for all the test materials exceeded 90 % after 24 hr with RhyOx showing the highest viability at 97 % compared to the 4 % and 92 % for the positive and negative controls respectively. The ND7/23 cell line showed a normalized viability greater than 95 % for all the metal oxides with PbO showing the highest viability at 98 % compared to the 8 % and 97 % for the positive and negative controls respectively. After day 3, all the test materials showed no cytotoxic effects and there was no evidence of apoptotic cell death. The normalized cell viability for the metal oxides were as high as 104 % for RhyOx compared to the 6 % and 96 % recorded for the positive and negative controls respectively, after 3 days of incubation of the 3T3 cell line. The ND7/23 cell showed a viability of a minimum of 95 % for the test materials compared to the 8 % and 96 % of the positive and negative controls respectively. Also on day 7, both cell lines showed high viability with no indication of cytotoxicity. The 3T3 cell line shows normalized viability greater than 82 % for the text metal oxides and the negative control as against a normalized viability of 8 % for the positive control after 7 days of incubation. The minimum viability after day 7 for the ND7/23 cell line was 89 % for the metal oxides and positive control. The negative control showed a viability of 5 %. Since the all the normalized viability of all the metal oxides was higher than 80 % for both cell lines, the metal oxides show good cytocompatibility and neurocompatibility.

Discissions and Conclusion

The study conclusively demonstrates the biocompatibility of the tested metal oxide coatings, as evidenced by the high cell viability percentages and the absence of cytotoxic effects in both 3T3 fibroblast and ND7/23 neuronal cell lines. The results exceed the standard threshold for non-cytotoxic materials, indicating that these metal oxides are not only safe for contact with these cell types but may also support their growth and function.

The findings have significant implications for the application of these metal oxides in biomedical devices, particularly in scenarios where direct contact with tissue or neural components is expected. The compatibility with both fibroblast and neuronal cells broadens the potential use of these materials in diverse medical applications, ranging from implants to neural interfaces.

Future studies could focus on long-term interactions and the in vivo response to these materials to further validate their suitability for clinical applications. Additionally, exploring the mechanisms behind the observed stimulatory effects on cell viability could open new avenues for the development of advanced biomaterials designed to actively promote tissue regeneration and repair.

Appendix B

Raw Data for Chapter 5

Table B1

Probe Calibration with NaCl.

Conc.	**0.0015**	**0.005**	**0.01**	**0.03**	**0.05**	**0.1**	**0.15**
Freq	**Zreal**	**Zreal**	**Zreal**	**Zreal**	**Zreal**	**Zreal**	**Zreal**
Hz	**ohm**	**ohm**	**ohm**	**ohm**	**ohm**	**ohm**	**ohm**
2000098	225.5176	95.9803	64.98318	17.73892	10.48431	5.854586	4.684505
1588770	254.8364	97.2528	64.48311	17.58262	10.10102	5.553677	4.40449
1261934	280.4212	98.3326	64.6349	17.38579	9.94238	5.436526	4.290432
1002480	298.8737	99.0308	63.85088	17.3216	9.8904	5.394919	4.243527
796230.4	311.6277	99.5059	62.01492	17.28545	9.87401	5.370903	4.219372
632519.5	320.3917	99.7395	61.79793	17.28516	9.86947	5.353683	4.204937
502441.4	326.055	99.9558	60.12177	17.29427	9.86884	5.347875	4.195878
399082	327.6031	99.9853	59.88999	17.28451	9.86783	5.340791	4.189502
317050.8	331.0992	100.0831	60.8724	17.27404	9.86572	5.334948	4.18431
251894.5	338.4958	100.2364	60.52472	17.25577	9.86492	5.330231	4.179293
200097.7	337.2055	100.132	60.26687	17.27616	9.86061	5.328215	4.176514
158964.8	336.3911	100.044	60.04454	17.25158	9.86034	5.326988	4.178654
126269.5	337.581	100.1604	59.98805	17.29644	9.86327	5.325217	4.182068
100253.9	336.764	100.1775	59.9064	17.30622	9.87905	5.332438	4.185145
79628.91	336.5248	100.2061	60.634	17.2879	9.89531	5.343608	4.195804
63339.84	336.2306	100.297	60.53994	17.33285	9.90543	5.354444	4.20663

Table B1 (Continued)

Probe Calibration with NaCl.

Conc.	**0.0015**	**0.005**	**0.01**	**0.03**	**0.05**	**0.1**	**0.15**
Freq	**Zreal**	**Zreal**	**Zreal**	**Zreal**	**Zreal**	**Zreal**	**Zreal**
Hz	**ohm**	**ohm**	**ohm**	**ohm**	**ohm**	**ohm**	**ohm**
50332.03	336.3002	100.4146	60.87593	17.37508	9.93281	5.374517	4.224409
40019.53	336.5281	100.4606	61.17617	17.41979	9.96565	5.397799	4.246197
31699.22	336.8017	100.501	61.48188	17.47332	10.00609	5.425292	4.271589
25253.91	336.4847	100.6818	61.50264	17.53709	10.05064	5.457245	4.300916
20097.66	336.9404	100.7933	61.53541	17.60933	10.10482	5.493205	4.333642
15798.61	336.7705	100.8965	61.79684	17.69478	10.16893	5.534631	4.372436
12557.87	337.2564	101.1501	62.23446	17.7932	10.23389	5.582136	4.413774
10011.57	337.2104	101.3228	62.71861	17.89423	10.3094	5.633582	4.459239
7928.241	337.7	101.6057	62.61856	18.0152	10.39332	5.692264	4.512506
6307.871	338.4194	101.8648	63.14841	18.14395	10.48569	5.756333	4.569921
5034.722	338.521	102.1614	62.79438	18.28606	10.58356	5.828445	4.634199
3993.056	339.0173	102.519	62.09379	18.45017	10.69763	5.911335	4.708907
3182.87	339.5625	102.9075	61.73599	18.62749	10.82226	6.003189	4.79363
2519.531	340.1995	103.358	60.30903	18.83012	10.96557	6.112268	4.894615
2000.762	340.9605	103.8592	59.64907	19.05296	11.12495	6.235159	5.010101

Table B1 (Continued)

Probe Calibration with NaCl

Conc.	**0.0015**	**0.005**	**0.01**	**0.03**	**0.05**	**0.1**	**0.15**
Freq	**Zreal**	**Zreal**	**Zreal**	**Zreal**	**Zreal**	**Zreal**	**Zreal**
Hz	**ohm**	**ohm**	**ohm**	**ohm**	**ohm**	**ohm**	**ohm**
1580.669	341.8059	104.4281	60.07885	19.30869	11.30935	6.382608	5.148786
1268.382	342.749	104.9957	60.53173	19.57514	11.50429	6.542566	5.302679
1000.702	343.8341	105.6976	61.07167	19.89677	11.74982	6.745644	5.498615
799.0057	345.0153	106.4324	61.64459	20.2454	12.01891	6.976239	5.71945
628.811	346.4236	107.2842	62.32324	20.6751	12.35412	7.268175	6.000193
502.2321	347.9742	108.1509	63.03306	21.14135	12.72652	7.592419	6.316125
400.1524	349.6439	109.1439	63.83318	21.69062	13.17996	7.983512	6.687452
315.5048	351.5718	110.32	64.76715	22.37053	13.75231	8.473955	7.138087
252.0161	353.6489	111.5449	65.76952	23.13729	14.40555	9.012883	7.623287
200.3205	355.9522	112.9651	66.94769	24.07631	15.20777	9.64726	8.190522
158.0056	358.6569	114.6255	68.36355	25.25236	16.19018	10.40145	8.852475
126.6892	361.4146	116.3979	69.89554	26.57031	17.26448	11.2097	9.53352
100.4464	364.6787	118.545	71.78488	28.22697	18.56938	12.16949	10.29196
79.44915	369.1763	121.3903	74.17895	30.22105	20.07178	13.21724	11.09537

Table B2

Modulus

	10P	**20P**	**30P**	**40P**	**50P**	**60P**	**70P**	**80P**	**90P**	**100P**
Freq	**Zmod**	**Zmod**	**Zmod**	**Zmod**	**Zmod**	**Zmod**	**Zmod**	**Zmod**	**Zmod**	**Zmod**
Hz	**ohm**	**ohm**	**ohm**	**ohm**	**ohm**	**ohm**	**ohm**	**ohm**	**ohm**	**ohm**
2000098	102.9188	92.69319	76.98487	72.67014	73.70354	72.97636	66.79312	65.90794	64.05269	57.98601
1588770	102.6492	84.89275	75.9078	83.15687	73.21215	75.06136	70.44828	67.94557	65.59573	58.20662
1261934	90.66948	78.00789	65.07839	63.64837	63.77372	64.20962	58.33612	57.44112	56.2572	51.08804
1002480	80.91229	70.46152	61.38386	56.09326	61.95745	61.8058	56.86549	52.3454	50.73522	45.18836
796230.4	77.90218	70.05508	58.7424	53.98589	56.50173	55.26805	51.18552	50.7324	49.11528	43.43883
632519.5	79.3171	64.07974	56.33369	54.13215	53.18181	55.16314	49.68361	49.52737	47.20658	42.50619
502441.4	87.74905	65.72851	56.54026	54.92894	52.98238	54.90505	49.04349	48.63595	47.13978	41.77935
399082	74.73831	64.92376	55.41628	51.66458	53.5003	54.22182	49.16556	47.78863	46.52414	40.94355
317050.8	69.97108	65.70974	55.16651	55.91637	53.91701	53.71903	48.25828	48.07698	45.23181	41.00086
251894.5	74.93898	63.75985	54.4746	55.84558	52.58604	53.88814	47.67096	47.40757	46.14932	41.17499
200097.7	74.18986	63.98871	53.34038	53.19772	50.72789	53.14119	47.45393	47.71641	44.92635	40.52386
158964.8	78.91549	62.2402	54.79112	51.32416	50.85348	53.62627	47.91909	49.32624	44.999	39.78332
126269.5	71.09588	66.55329	54.26426	52.23757	54.09287	51.80282	45.84891	46.54291	44.38047	40.20519
100253.9	72.45883	62.19437	53.77349	50.59846	50.58778	52.07651	46.20631	45.74768	44.21624	39.72146
79628.91	75.14244	63.57776	55.83847	52.49601	51.70708	53.54469	46.93797	46.83816	45.31603	40.78671
63339.84	71.90172	60.85138	53.66484	50.47451	49.49424	51.4808	45.01044	44.93336	43.3769	39.24221
50332.03	69.10175	58.49849	51.70125	48.14621	47.59444	49.37355	43.1825	43.51182	41.71164	37.47143
40019.53	67.49788	57.60976	51.19743	47.71696	46.87281	48.60038	42.4604	42.58505	41.20886	37.23541
31699.22	68.02099	57.55919	50.71046	47.51297	46.51224	48.23577	42.04697	42.24685	40.73415	36.93486

Table B2 (Continued)

Modulus

	10P	**20P**	**30P**	**40P**	**50P**	**60P**	**70P**	**80P**	**90P**	**100P**
Freq	**Zmod**	**Zmod**	**Zmod**	**Zmod**	**Zmod**	**Zmod**	**Zmod**	**Zmod**	**Zmod**	**Zmod**
Hz	**ohm**	**ohm**	**ohm**	**ohm**	**ohm**	**ohm**	**ohm**	**ohm**	**ohm**	**ohm**
25253.91	66.60196	56.82711	50.45414	46.80915	46.81547	48.32566	41.67298	41.98653	40.91294	37.00217
10011.57	69.15686	57.77954	52.86802	47.61323	47.33488	49.31948	42.08048	42.42638	41.10598	37.09742
7928.241	68.78466	58.27905	52.91393	48.84665	47.79393	48.97402	42.0249	42.96121	41.32391	37.80019
6307.871	70.50193	57.3619	53.62375	49.48862	48.27267	49.84726	42.21125	42.8199	41.20645	37.74739
5034.722	70.47301	59.32803	54.25182	49.73259	48.49334	50.54805	42.97561	43.99246	42.03632	38.43985
3993.056	71.36278	60.08563	55.18473	50.52846	49.18475	51.29991	43.47484	44.60786	42.53613	38.95586
3182.87	72.32761	60.93933	56.18633	51.40501	49.95949	52.17753	44.0558	45.31091	43.12765	39.56034
2519.531	73.62817	61.94133	57.34167	52.58145	50.89068	53.16636	44.74854	46.15412	43.80653	40.30863
2000.762	74.97399	63.10151	58.70063	53.85534	51.92551	54.40627	45.59155	47.12969	44.61579	41.1564
1580.669	76.62526	64.51871	60.26269	55.38835	53.17525	55.83244	46.56588	48.27578	45.56474	42.18139
1268.382	78.31155	66.06784	61.90436	57.10226	54.5159	57.43672	47.64993	49.52588	46.61244	43.31211
1000.702	80.57209	67.93462	63.92776	59.30328	56.20421	59.43849	49.03632	51.11501	47.9234	44.70994
799.0057	82.99426	70.10211	66.26594	61.79093	58.0464	61.78538	50.61608	52.87901	49.40758	46.24049
628.811	86.14619	72.83342	69.1764	64.92662	60.35964	64.74465	52.60265	55.08252	51.28494	48.1813
502.2321	89.59011	75.99103	72.25923	68.60072	62.95731	68.12595	54.86046	57.5235	53.36001	50.33819

Table B2 (Continued)

Modulus

	10P	**20P**	**30P**	**40P**	**50P**	**60P**	**70P**	**80P**	**90P**	**100P**
Freq	**Zmod**	**Zmod**	**Zmod**	**Zmod**	**Zmod**	**Zmod**	**Zmod**	**Zmod**	**Zmod**	**Zmod**
Hz	**ohm**	**ohm**	**ohm**	**ohm**	**ohm**	**ohm**	**ohm**	**ohm**	**ohm**	**ohm**
400.1524	93.67765	79.70619	75.96851	73.04867	66.04154	72.35788	57.5845	60.46946	55.85197	52.95514
315.5048	98.83261	84.43948	80.55117	79.20922	69.93372	77.74969	61.01612	64.02478	58.94366	56.24122
252.0161	104.6015	89.81594	85.70709	85.7818	74.31234	83.90019	64.96508	67.97505	62.44454	60.0442
200.3205	111.6777	96.44992	92.03732	93.83694	79.72334	91.52861	69.71362	72.95513	66.70037	64.66673
158.0056	120.3556	104.7133	99.90231	103.7747	86.47568	101.2207	75.54671	79.07876	71.90276	70.43179
126.6892	130.3086	113.8142	108.5888	114.9948	93.97334	112.2115	82.03535	85.73599	77.73647	77.18758
100.4464	142.4251	125.612	119.3435	128.5906	103.4095	125.9348	90.17565	94.45817	84.90985	85.45316
79.44915	157.2907	139.7402	132.4239	145.3619	114.9121	142.7986	102.2248	105.0081	93.59998	95.658

Table B3

Phase

	0P	10P	20P	30P	40P	50P	60P	70P	80P	90P	100P
Freq	**Zphz**	**Zphz**	**Zphz**	**Zphz**	**Zphz**	**Zphz**	**Zphz**	**Zphz**	**Zphz**	**Zphz**	**Zphz**
Hz	°	°	°	°	°	°	°	°	°	°	°
2000098	48.33999	1.801019	3.024118	3.085296	2.025307	-3.10123	5.154817	2.458045	-0.45603	5.346932	-0.64212
1588770	39.99859	13.42733	14.91566	22.62522	15.1856	6.994091	12.35578	14.33485	12.69701	15.45309	12.6561
1261934	43.62213	16.16364	16.58214	16.29963	15.90204	10.46728	15.10621	14.59457	12.8692	18.13018	14.0344
1002480	37.92769	12.01697	14.26671	14.72054	14.31562	10.75867	12.0504	13.28776	12.26834	15.17183	13.72442
796230.4	31.93247	11.85758	10.38715	13.46547	11.03598	6.425121	11.33949	10.56478	10.89144	13.3386	10.47653
632519.5	27.31095	8.22131	9.42884	9.100524	9.023889	5.742428	9.541104	8.409324	6.3282	10.32589	9.0915
502441.4	20.27935	8.178789	9.176237	6.760224	7.706786	10.03099	5.111573	6.989118	5.680199	7.978081	7.48514
399082	17.04328	6.575161	6.840508	7.184272	6.11561	3.425152	6.339279	7.459965	4.20759	5.273164	6.762844
317050.8	16.4543	3.724359	5.531718	6.189143	6.035224	3.479102	6.051471	4.689713	5.051728	5.58398	5.523948
251894.5	14.4346	5.195243	5.463813	5.681863	3.877362	4.813765	4.55236	4.762616	4.060939	4.658083	4.7586
200097.7	12.98489	3.789821	5.441176	4.365766	5.175641	3.92555	5.383514	2.746857	2.433405	6.503776	3.597388
158964.8	7.794143	3.320928	4.709295	5.404016	2.952816	6.935687	2.199188	5.291182	5.868123	4.018455	3.448823
126269.5	6.577337	4.053344	4.145122	4.526873	5.925832	2.37849	4.222717	2.518416	2.951754	5.080818	4.42918
100253.9	5.515238	3.221873	3.216329	3.012219	3.157211	2.111319	2.76629	2.942132	2.64812	3.555047	3.367284
79628.91	4.543299	0.255017	0.203772	0.12393	0.048185	-0.20188	0.041676	-0.13306	-0.18697	0.694551	0.372014
63339.84	2.525352	9.243431	9.07442	8.661285	9.013988	8.26845	8.796125	9.02892	8.890432	9.228914	8.987677
50332.03	2.010018	6.050561	6.088767	5.23539	5.448016	4.951724	5.233094	5.438272	5.424957	5.797166	5.819966
40019.53	1.505117	4.325699	3.906929	3.671321	3.643554	3.566636	3.533464	3.733705	4.01315	4.177418	4.501913

Table B3

Phase (Continued)

	0P	10P	20P	30P	40P	50P	60P	70P	80P	90P	100P
Freq	**Zphz**	**Zphz**	**Zphz**	**Zphz**	**Zphz**	**Zphz**	**Zphz**	**Zphz**	**Zphz**	**Zphz**	**Zphz**
Hz	°	°	°	°	°	°	°	°	°	°	°
31699.22	0.933283	2.811773	3.121725	2.431442	2.519112	2.617972	2.428941	2.502294	2.343339	2.741695	2.621087
25253.91	0.424979	2.137148	1.804477	1.233044	1.345466	1.118854	1.668772	0.927078	1.542563	1.221477	0.833157
20097.66	0.086164	0.933797	0.663148	-0.64009	0.007664	1.700814	0.607828	0.635614	0.09158	0.67359	0.054035
10011.57	-0.96725	-2.37062	-1.60721	-2.35864	-2.62973	-2.52421	-2.90755	-3.11738	-2.52027	-2.186	-2.63681
7928.241	-1.34691	-2.69098	-2.73691	-4.10725	-3.85399	-4.30393	-3.50293	-3.39538	-3.31312	-3.73446	-3.80709
6307.871	-1.68351	-4.10847	-4.57169	-5.3808	-4.04696	-4.93792	-4.45138	-4.99992	-3.63056	-4.22904	-4.50332
5034.722	-2.10591	-4.90989	-4.78877	-6.21995	-5.53992	-4.63735	-5.01504	-5.47787	-5.35541	-5.33884	-5.62805
3993.056	-2.58997	-5.88402	-5.71976	-7.3363	-6.53474	-5.53435	-5.93894	-6.45649	-6.32985	-6.35564	-6.73642
3182.87	-3.05965	-6.89618	-6.69804	-8.55301	-7.56943	-6.42041	-6.92965	-7.46977	-7.34811	-7.40611	-7.92424
2519.531	-3.60569	-8.00693	-7.77591	-9.91494	-8.68989	-7.44395	-8.01361	-8.56872	-8.43859	-8.59596	-9.25649
2000.762	-4.20203	-9.21032	-8.93899	-11.3585	-9.92145	-8.49063	-9.19561	-9.741	-9.63889	-9.8641	-10.7002
1580.669	-4.88501	-10.5562	-10.2537	-12.9746	-11.2746	-9.71496	-10.4938	-11.0774	-10.9415	-11.3013	-12.3422

Table B3

Phase (Continued)

	0P	**10P**	**20P**	**30P**	**40P**	**50P**	**60P**	**70P**	**80P**	**90P**	**100P**
Freq	**Zphz**	**Zphz**	**Zphz**	**Zphz**	**Zphz**	**Zphz**	**Zphz**	**Zphz**	**Zphz**	**Zphz**	**Zphz**
Hz	°	°	°	°	°	°	°	°	°	°	°
1268.382	-5.61134	-11.9496	-11.564	-14.6661	-12.6419	-10.9666	-11.8455	-12.3996	-12.2343	-12.7586	-14.0556
1000.702	-6.45062	-13.5839	-13.1272	-16.628	-14.2798	-12.4305	-13.4209	-14.0034	-13.8436	-14.491	-16.0608
799.0057	-7.3407	-15.2659	-14.7463	-18.6235	-15.9465	-13.9326	-15.1066	-15.6731	-15.4394	-16.2808	-18.1733
628.811	-8.36947	-17.2283	-16.6255	-20.9381	-17.8693	-15.7692	-17.0674	-17.5815	-17.3323	-18.3751	-20.6021
315.5048	-11.5297	-23.6655	-22.747	-28.5183	-24.1373	-21.8089	-23.6369	-24.0761	-23.5583	-25.4026	-28.7269
252.0161	-12.5584	-25.979	-24.9461	-31.0823	-26.3043	-24.0231	-26.0489	-26.4467	-25.8315	-27.9793	-31.5882
200.3205	-13.539	-28.3992	-27.266	-33.7124	-28.7244	-26.3821	-28.5773	-28.9725	-28.2409	-30.7061	-34.5383
158.0056	-14.5241	-30.9462	-29.6933	-36.353	-31.2618	-28.9024	-31.2462	-31.6436	-30.7516	-33.5741	-37.5195
126.6892	-15.3611	-33.3804	-31.9909	-38.6427	-33.6219	-31.1973	-33.7054	-34.0673	-33.155	-36.3758	-40.2222
100.4464	-16.1471	-35.8488	-34.3782	-41.0453	-36.1263	-33.6387	-36.3302	-36.6675	-35.6301	-39.1599	-42.9348
79.44915	-25.2717	-37.5258	-36.7557	-43.3208	-38.6634	-36.1295	-38.8531	-39.1915	-38.1206	-41.9169	-45.5227

Table B4

Conductivity of AF Tissue after Exposures to Single 100 µsPEF Voltage

	0	**500**	**600**	**700**	**800**	**900**	**1000**
Freq	**σ**	**σ**	**σ**	**σ**	**σ**	**σ**	**σ**
Hz	**S/m**	**S/m**	**S/m**	**S/m**	**S/m**	**S/m**	**S/m**
2000098	0.724356	0.394006	0.338022	0.337183	0.292502	0.16014	0.177089
1588770	0.781908	0.387775	0.33911	0.335295	0.289189	0.157434	0.172558
1261934	0.934549	0.402927	0.347208	0.348593	0.301761	0.167077	0.177165
1002480	1.082113	0.413618	0.351718	0.35639	0.30959	0.173247	0.185002
796230.4	1.387651	0.423079	0.357001	0.358064	0.315979	0.177197	0.190167
632519.5	1.82335	0.424947	0.361324	0.363986	0.316062	0.180775	0.191508
502441.4	2.085008	0.429182	0.363735	0.361348	0.316953	0.180641	0.19398
399082	1.966916	0.431365	0.363423	0.366808	0.321386	0.183773	0.198942
317050.8	1.871217	0.428221	0.361321	0.366514	0.322091	0.184198	0.192977
251894.5	2.460448	0.42909	0.363298	0.365739	0.321025	0.18474	0.196009
200097.7	3.686825	0.433713	0.363574	0.371056	0.317338	0.186055	0.197559
158964.8	1.238626	0.435138	0.3625	0.369861	0.321991	0.186369	0.196902
126269.5	1.870451	0.435817	0.366116	0.373317	0.32443	0.188284	0.196466
100253.9	2.406988	0.438808	0.365941	0.372248	0.325966	0.189053	0.199969
79628.91	2.392266	0.435587	0.362443	0.369396	0.322887	0.187227	0.19824
63339.84	0.764869	0.439382	0.364957	0.37292	0.325927	0.1894	0.200141
50332.03	1.667547	0.447585	0.370553	0.378726	0.332102	0.193914	0.205869
40019.53	2.030268	0.449915	0.371927	0.380645	0.333562	0.195737	0.207574
31699.22	1.787941	0.451225	0.372173	0.381433	0.335555	0.196585	0.209079
25253.91	1.538456	0.452654	0.373569	0.382765	0.335059	0.197712	0.20906

Table B4 (**Continued**)

Conductivity of AF Tissue after Exposures to Single 100 µsPEF Voltage

	0	**500**	**600**	**700**	**800**	**900**	**1000**
Freq	**σ**	**σ**	**σ**	**σ**	**σ**	**σ**	**σ**
Hz	**S/m**	**S/m**	**S/m**	**S/m**	**S/m**	**S/m**	**S/m**
20097.66	1.321109	0.453355	0.374246	0.383688	0.334992	0.198269	0.208904
15798.61	2.574972	0.452284	0.372027	0.381634	0.335915	0.197521	0.208985
12557.87	2.756294	0.45309	0.373271	0.380756	0.334573	0.197306	0.208072
10011.57	3.243312	0.452888	0.370992	0.381422	0.334374	0.197401	0.209694
7928.241	3.476253	0.451747	0.368955	0.379808	0.332354	0.196828	0.207691
6307.871	4.13623	0.450801	0.369028	0.37948	0.331811	0.195855	0.207689
5034.722	3.82947	0.449044	0.367982	0.377296	0.330237	0.1944	0.206047
3993.056	2.931927	0.447378	0.366514	0.375585	0.328694	0.193209	0.204773
3182.87	3.106463	0.445439	0.364877	0.373693	0.326906	0.19182	0.20334
2519.531	3.318807	0.44319	0.362991	0.371508	0.324828	0.190205	0.201715
2000.762	3.467439	0.440613	0.360921	0.3691	0.322561	0.188413	0.199802
1580.669	3.887493	0.437672	0.358612	0.366388	0.320004	0.186314	0.197662
1268.382	3.779081	0.43455	0.356245	0.363582	0.317385	0.18412	0.195395
1000.702	5.16782	0.430733	0.353463	0.360228	0.314204	0.181505	0.192659
799.0057	4.574222	0.426717	0.350563	0.356773	0.31095	0.17869	0.189754
628.811	3.365674	0.421972	0.347193	0.35273	0.307135	0.175463	0.186331

Table B5

Conductivity of AF Tissue after Exposures to 100 µsPEF at 500 V

	0	**10**	**20**	**50**	**80**	**100**
Freq	**σ**	**σ**	**σ**	**σ**	**σ**	**σ**
Hz	**S/m**	**S/m**	**S/m**	**S/m**	**S/m**	**S/m**
2000098	0.145266	0.240411	0.260591	0.225393	0.22409	0.245452
1588770	0.146331	0.247216	0.273662	0.211522	0.226558	0.283871
1261934	0.144085	0.247261	0.268627	0.214796	0.223909	0.225319
1002480	0.142221	0.244232	0.26669	0.228442	0.226042	0.27214
796230.4	0.140666	0.242218	0.264695	0.233012	0.225093	0.286549
632519.5	0.139202	0.240303	0.263055	0.225415	0.233969	0.297833
502441.4	0.139703	0.246457	0.264256	0.226652	0.242672	0.304468
399082	0.137277	0.237653	0.260846	0.222664	0.248082	0.31244
317050.8	0.136642	0.237303	0.259941	0.216256	0.247096	0.313845
251894.5	0.135359	0.235786	0.258763	0.229	0.254415	0.311008
200097.7	0.134513	0.234678	0.258297	0.247985	0.257139	0.324086
158964.8	0.133523	0.233678	0.257447	0.248392	0.242474	0.330659
126269.5	0.132636	0.232918	0.256815	0.217534	0.264726	0.32926
100253.9	0.131781	0.231947	0.256117	0.245927	0.27076	0.335554
79628.91	0.130953	0.230673	0.255221	0.234876	0.255389	0.314339
63339.84	0.130348	0.229851	0.254657	0.266338	0.287923	0.352416
50332.03	0.12951	0.228515	0.253512	0.288038	0.307913	0.387161
40019.53	0.128639	0.227005	0.252185	0.296885	0.321319	0.392527
31699.22	0.12771	0.225326	0.250507	0.303014	0.327727	0.399988
25253.91	0.1267	0.223589	0.24886	0.298085	0.329735	0.398689
20097.66	0.125621	0.221693	0.247019	0.303733	0.327191	0.396162
15798.61	0.124314	0.219497	0.244877	0.299556	0.333694	0.404998
12557.87	0.122897	0.217085	0.242463	0.310468	0.324044	0.396711
10011.57	0.121251	0.214396	0.239715	0.289274	0.325629	0.392811
7928.241	0.119394	0.211328	0.236554	0.285379	0.316174	0.379831
6307.871	0.117537	0.207962	0.232964	0.276369	0.320871	0.37804
5034.722	0.115523	0.204339	0.228898	0.27517	0.304115	0.366178
3993.056	0.113244	0.200201	0.224184	0.267049	0.296324	0.356305
3182.87	0.11077	0.195674	0.21897	0.258563	0.287945	0.345489
2519.531	0.107971	0.190441	0.213042	0.249287	0.278619	0.333404
2000.762	0.104942	0.184782	0.206438	0.24004	0.268997	0.32089
1580.669	0.101599	0.178495	0.199087	0.230059	0.258455	0.307365
1268.382	0.098182	0.172125	0.191638	0.220506	0.248229	0.293936
1000.702	0.094347	0.164828	0.183002	0.209983	0.236633	0.279422
799.0057	0.090494	0.157502	0.174245	0.200043	0.225325	0.265492
628.811	0.086286	0.149396	0.164534	0.189213	0.212971	0.25041

Table B5 (**Continued**)

Conductivity of AF Tissue after Exposures to 100 µsPEF at 500 V

	0	**10**	**20**	**50**	**80**	**100**
Freq	**σ**	**σ**	**σ**	**σ**	**σ**	**σ**
Hz	**S/m**	**S/m**	**S/m**	**S/m**	**S/m**	**S/m**
502.2321	0.082257	0.1415	0.155075	0.178787	0.201114	0.235998
400.1524	0.078121	0.133324	0.145382	0.168282	0.18888	0.221204
315.5048	0.07372	0.124634	0.135092	0.157138	0.176233	0.205834
252.0161	0.069587	0.116414	0.125564	0.146667	0.16435	0.191092
200.3205	0.065443	0.108181	0.116031	0.135894	0.1521	0.176421
158.0056	0.061262	0.099739	0.106608	0.124896	0.139681	0.161602
126.6892	0.057552	0.092188	0.098464	0.114782	0.113818	0.147599
100.4464	0.053812	0.084568	0.089975	0.104575	0.104429	0.133933
79.44915	0.049533	0.075802	0.079888	0.094536	0.095252	0.120674

Appendix C

Pulse Waveforms for Chapter 6

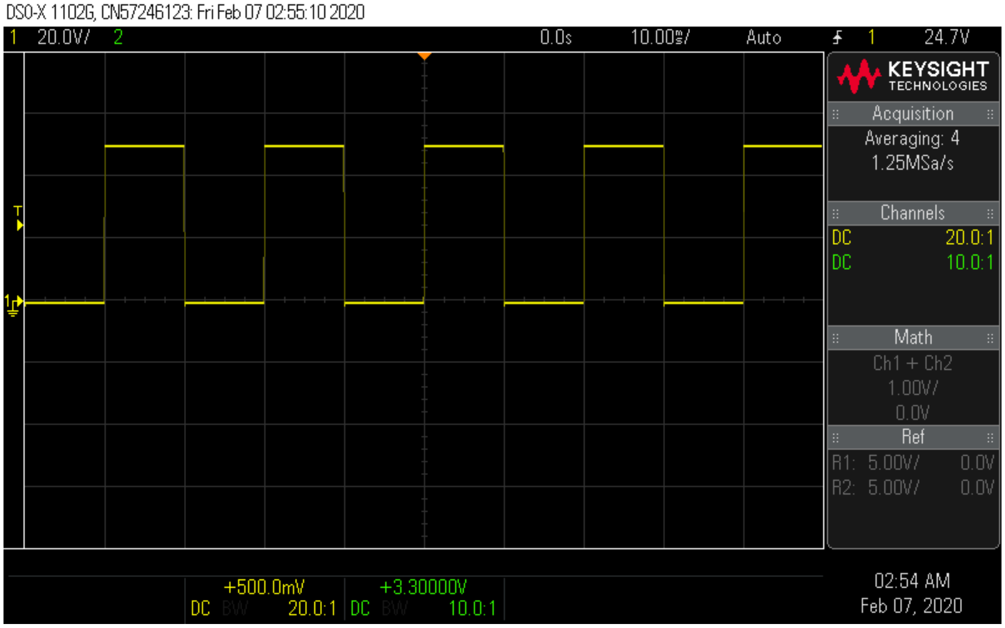

*Figure C1***.** Square shaped PEF waveform

Appendix D

COMSOL Simulation for Chapter 6

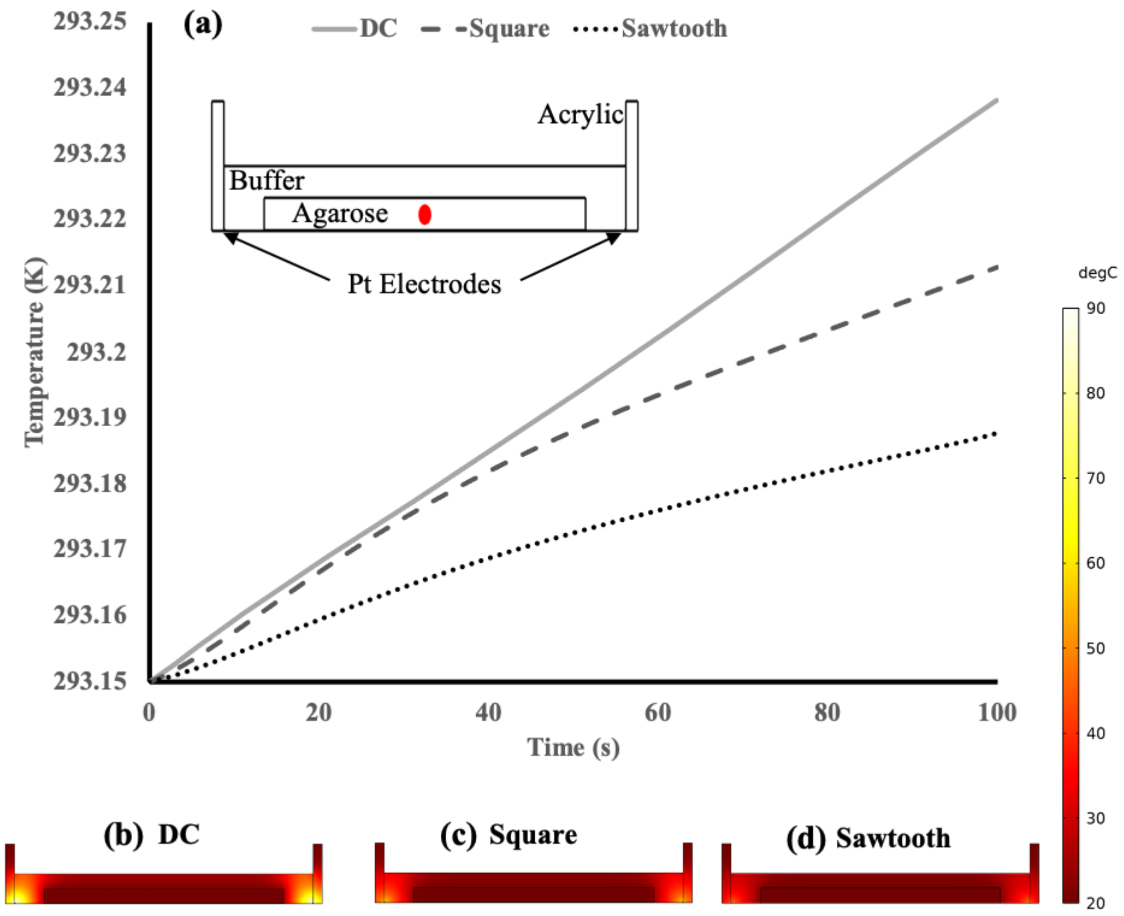

Figure D1. COMSOL model prediction of temperature during electrophoresis using different waveforms.

The inset shows the 2D geometry with labels denoting materials used. Temperature of the middle of the gel over 100 s (a) rises most quickly for the DC field, followed by the square-wave pulsed field and then the sawtooth pulsed field. Temperature distributions at the final time point within the models are shown for (b) DC, (c) square, and (d) sawtooth fields.

Appendix E

Figures for Chapter 7

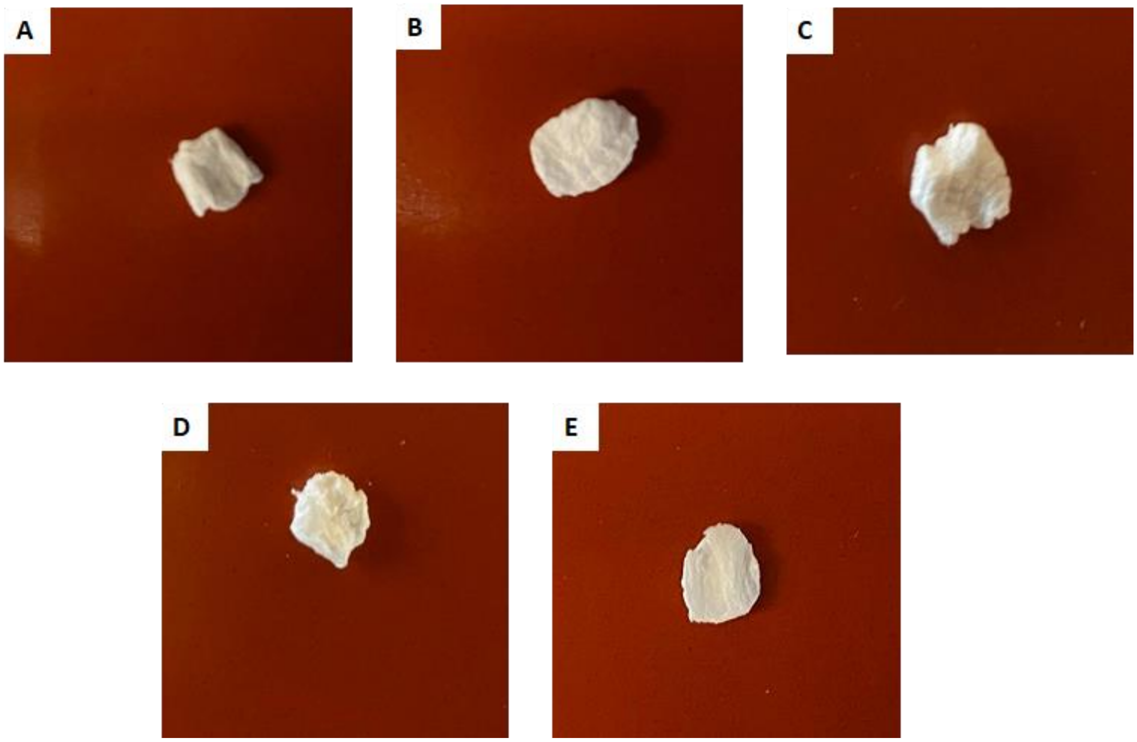

Figure E1. Cellular and acellular AF Tissue scaffolds. (a) Control, (b) PEF, (c) 0.5% SDS, (d) 1% SDS, (e) 3% Triton X-100.

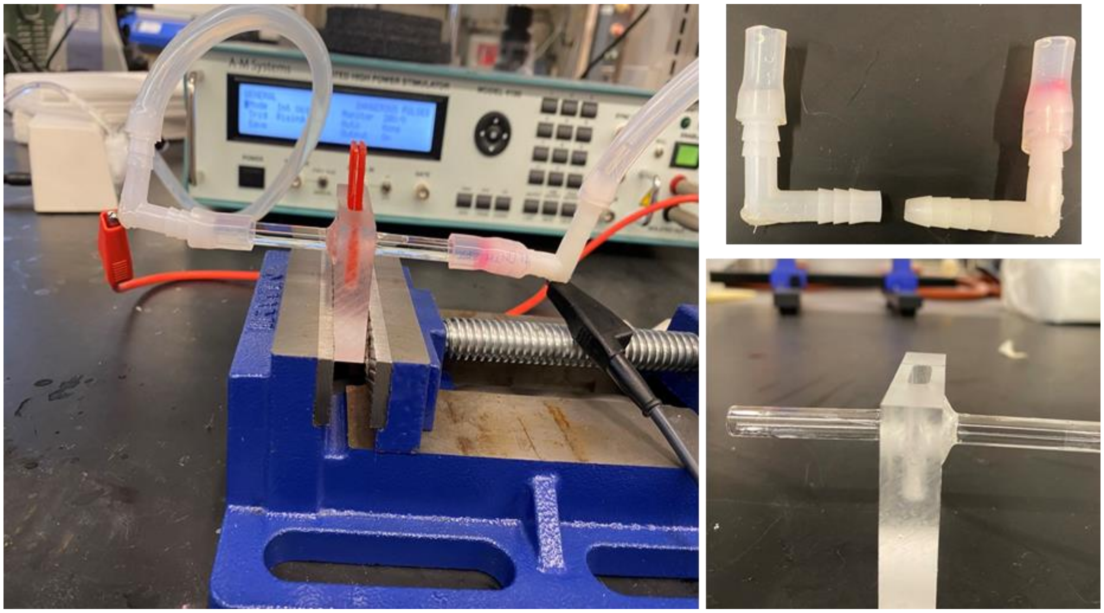

*Figure E2***.** Setup of chamber and components for electro kinetic extraction with pulsed electric fields.